Chapter 9

Seismic Arrays

(Version December 2011; DOI: 10.2312/GFZ.NMSOP-2_ch9)

Johannes Schweitzer, Jan Fyen, Svein Mykkeltveit,
Steven J. Gibbons, Myrto Pirli, Daniela Kühn, and Tormod Kværna[1)]

[1)] All: NORSAR, Gunnar Randers vei 15, P.O. Box 53, N-2027 Kjeller, Norway; contact via:
Phone: +47-63805900, E-mail: johannes.schweitzer@norsar.no

9.1 Outline

When the Manual of Seismological Observatory Practice (Willmore, 1979) was published, only a small number of seismic arrays with open data access were in operation. At the time, array seismology was limited to a very small number of specialists and, as a result, the chapter on array seismology in that issue of the Manual comprised just two pages, including one figure. Over the last three decades, many new seismic arrays have been deployed globally and, due to improvements in digital data acquisition systems and digital signal processing, it has become much easier to handle the large amount of data generated by seismic arrays. Array data have also become more easily accessible, and some array data are now even available in near real-time via SEEDlink servers. Consequently, array observations have now become more common in the seismological community. This chapter on array seismology explains the principles of seismic arrays and how array data can be used to analyze different types of seismic signals.

In the following sections, we define the term “seismic array” and show examples of seismic arrays installed around the world. We then describe the theoretical basics of the processing of seismic data observed with an array, continue with the explanation of tools for the analysis of transient signals and ambient noise observed with seismic arrays and describe some considerations in the optimization of seismic array configurations, in order to provide guidance for new array installations. We explain how seismic, in particular local and regional, events are located at the NORSAR Data Processing Center using only single array observations and, finally, discuss the application of seismic arrays to earthquake early warning systems.

9.2 Introduction

"The Conference of Experts to study the methods of detecting violations of a possible agreement on the suspension of nuclear tests" held in 1958 in Geneva under the auspices of the United Nations, was followed by several initiatives for improving the quality of seismic stations worldwide. At the same time, the idea of installing arrays of sensors to improve the Signal-to-Noise Ratio (SNR) of seismic onsets was adopted from radio astronomy, radar, acoustics, and sonar. In the 1960s, it was demonstrated that seismic arrays could facilitate detection and characterization of seismic signals that was superior to that possible using single three-component stations. Today, many of the seismic stations of the International Monitoring System (IMS) for the Comprehensive Nuclear-Test-Ban Treaty Organization (CTBTO) (see e.g., Dahlman et al., 2009) are arrays.

Seismic arrays were used to investigate the nature and source regions of microseisms (e.g., Capon, 1969b; Lacoss et al., 1969; Cessaro, 1994; Friedrich et al., 1998; Essen et al., 2003; Schulte-Pelkum et al., 2003). Since the 1980 (see e.g., Furumoto et al., 1990; Chouet, 1996; Almendros, 1997), seismic arrays have also become a tool for locating and tracking volcanic tremor and for analyzing complex seismic wave-field properties in volcanic areas (see also Section 13.4.4 in Chapter 13). Not only usual seismometers but also strong motion instruments (often sensitive to ground accelerations) have been installed in array configurations to study near field effects of earthquakes (see e.g., Spudich and Cranswick (1984); Abrahamson et al., (1987); Goldstein and Archuleta (1991b); Chiu et al., (1994); Huang (2001); or more recently Halldorson et al., 2009). For borehole installations of strong-motion sensors in array configurations see Section 7.4.6 of Chapter 7. Another possible application of seismic arrays was shown by Frankel et al. (1991), who used a temporary, very small aperture array to track aftershock activities after the 1989 Loma Prieta earthquake.

A seismic array is a set of seismometers deployed so that characteristics of the seismic wavefield at a specified reference point, within or close to the array, can be inferred by analyzing the waveforms recorded at the different sites. A seismic array differs from a local network of seismic stations mainly by the techniques used for data analysis. Thus, in principle, a network of seismic stations can be used as an array, and data from an array can be analyzed as data from a network. The size of an array is defined by its aperture, which is the largest horizontal distance between two sensors of the array. In practice, the geometry and the number of seismometer sites of an array are determined by the intended scientific purpose and economic limits. Details about array configurations can be found e.g., in Barber (1958; 1959), Haubrich (1968), Harjes and Henger (1973), or in Mykkeltveit et al. (1983; 1988).

Most array processing techniques require high signal coherency across the array, and this imposes signal frequency dependent constraints on the array geometry (spatial extent) and instrumentation. A homogeneous geology below all sites of the array is preferable since geological heterogeneity will diminish waveform semblance. Furthermore, proper analysis of array data depends on a stable, high precision relative timing of all array elements. This is required because most of the parametric information calculated using the array involves the measurement of (usually very small) time differences (phase shifts) between the seismic arrivals on the different sensors.

The superior signal detection capabilities of seismic arrays result from the use of so-called "beamforming" techniques whereby the signals at different sensors are delayed and stacked. The SNR is enhanced since the signals interfere constructively whereas the (random)

background noise is suppressed. Arrays can also provide estimates of the station-to-event azimuth (backazimuth, BAZ) and the apparent velocity of the seismic signals. These estimates are important both for event location purposes and for signal identification and classification, e.g., as P, S, local, regional, or teleseismic phases.

In principle, the slowness resolution of an array – i.e., how accurately the direction and apparent velocity of an incoming wavefront can be measured – improves with increasing the array aperture. However, the signal coherency diminishes with increasing sensor separation and so the spatial extent of an array is usually specified to provide an optimal trade-off between coherency and theoretical slowness resolution.

In this chapter we describe procedures for estimating the apparent wavefront velocity (inverse of the slowness or ray parameter), the angles of approach (backazimuth and incidence angle; cf. Figs. 9.8 and 9.9 in this Chapter) of a seismic signal as well as basic processing algorithms for signal detection, one-array regional phase association, and the preparation of an automatic event bulletin. Throughout the text, we use data processing examples from the large NORSAR array (NOA) in southern Norway and from the "regional" arrays NORES in southern Norway, ARCES in northern Norway and GERES in southeast Germany.

There have, historically, been few publications that provide tutorial details about basic array processing. There are numerous papers detailing advanced techniques and presenting results from observations, but the basics of beamforming and STA/LTA detection processing are mostly assumed to be known. The processing algorithms used are similar to many types of signal-processing applications and time-series analysis in fields such as radar technology (e.g., Barber, 1958; 1959) and in seismic prospecting. In seismic prospecting, "beamforming" is called "stacking".

The basic processing techniques developed in the 1960s have survived, and are still in use. The *Seismic Array Design Handbook* (IBM, 1972) describes the processing algorithms for the arrays LASA and NORSAR (today NOA). References therein are mostly to reports prepared by J. Capon and R. T. Lacoss of Lincoln Laboratories. A description of many array methods and early array installations can be found in a proceedings volume (Beauchamp, 1975) of a NATO Advanced Study Institute conference in 1974 in Sandefjord, Norway. In 1990, a special issue of the *Bulletin of the Seismological Society of America* was published (Volume **80**, Number 6B) with contributions from a symposium titled "Regional Seismic Arrays and Nuclear Test Ban Verification". This issue contains many papers on theoretical and applied array seismology. More recent reviews on array applications in seismology can be found in e.g., Douglas (2002), Gibbons et al. (2009) or Rost and Thomas (2002; 2009). Since the 1970s, NORSAR has published Semiannual Scientific Reports, and several issues of this series cover array data processing techniques and their applications. A special issue on "Array seismology in Europe: recent developments and applications" was published in 2011 in the *Journal of Seismology* (for an overview see Schweitzer and Krüger, 2011).

At the NORSAR Data Processing Center (NDPC) at Kjeller, Norway, data have been acquired for many years from different types of arrays: e.g., the large aperture NORSAR array (today NOA), the small aperture arrays NORES and ARCES and the very small aperture array on Spitsbergen (SPITS). We describe the general array-processing techniques for training purposes and for use as a reference for analysts new to the field of seismic array processing. Some algorithms are described in detail, whereas others have references to available

literature. It is assumed that the reader has a basic knowledge of time-series analysis such as bandpass filtering and Fourier transforms (e.g., Buttkus, 2000; Scherbaum, 2001).

Communication technologies for data transmission (in near real time) between the arrays sites and data processing centers are now available and cost effective. The volume of data generated by an array of seismometers and the associated digital signal processing no longer represent insurmountable technical difficulties. However, low-threshold detection processing leads to large numbers of triggers, all of which require analysis. It is therefore of great importance to use techniques that are robust and easy to operate in an automatic, uninterrupted mode. Three main stages of automatic data processing are employed at the NDPC:

- Detection Processing (DP), which uses beamforming, filtering and STA/LTA detectors to define signal triggers;
- Signal Attribute Processing (SAP), which uses techniques such as frequency-wavenumber (f-k) analysis to estimate the slowness vector, and other techniques to estimate parameters such as the onset time, period, amplitude and polarization attributes for every trigger; and
- Event Processing (EP), which analyzes the attributes and sequence of triggers to associate seismic phase arrivals to define events.

A documentation of these processing steps can be found in Mykkeltveit and Bungum (1984) with results from a first version of a program (called RONAPP) for detecting and associating seismic signals from regional events using data from the small aperture, regional array NORES. Later, the NORSAR processing was re-coded to adapt to any array, several data formats and machine architectures. These algorithms are packaged into the programs DP for continuous detection processing, and EP for automatic signal attribute processing, event processing, and interactive special processing (Fyen, 1989; 2001a and b). These programs have been used for almost all examples herein. Section 9.13 shows and explains the output of this automatic data processing for some signals observed with the ARCES array as an example of routine array data analysis.

9.3 Examples of seismic arrays

To the best of our knowledge, the first experimental seismic array with more than four elements and openly available data was established in February 1961 by the United Kingdom Atomic Energy Agency (UKAEA) on Salisbury Plain (UK), followed in December 1961 by Pole Mountain (PMA, Wyoming, USA), in June 1962 by Eskdalemuir (EKA, Scotland, UK), and in December 1963 by Yellowknife (YKA, Canada). These types of arrays (the so-called UK-arrays) are orthogonal linear or L-shaped. Later, arrays of the same type were built in Australia (Warramunga), Brazil (Brasilia), and India (Gauribidanur). A detailed description of this type of arrays can be found in Keen et al. (1965), Birtill and Whiteway (1965), and Whiteway (1965; 1966). Fig. 9.1 shows the configuration of the Yellowknife array (Somers and Manchee, 1966; Manchee and Weichert, 1968; Weichert, 1975) as one example of this kind of medium-sized array, which is still in operation. The apertures of the UKAEA arrays vary between 10 and 25 km.

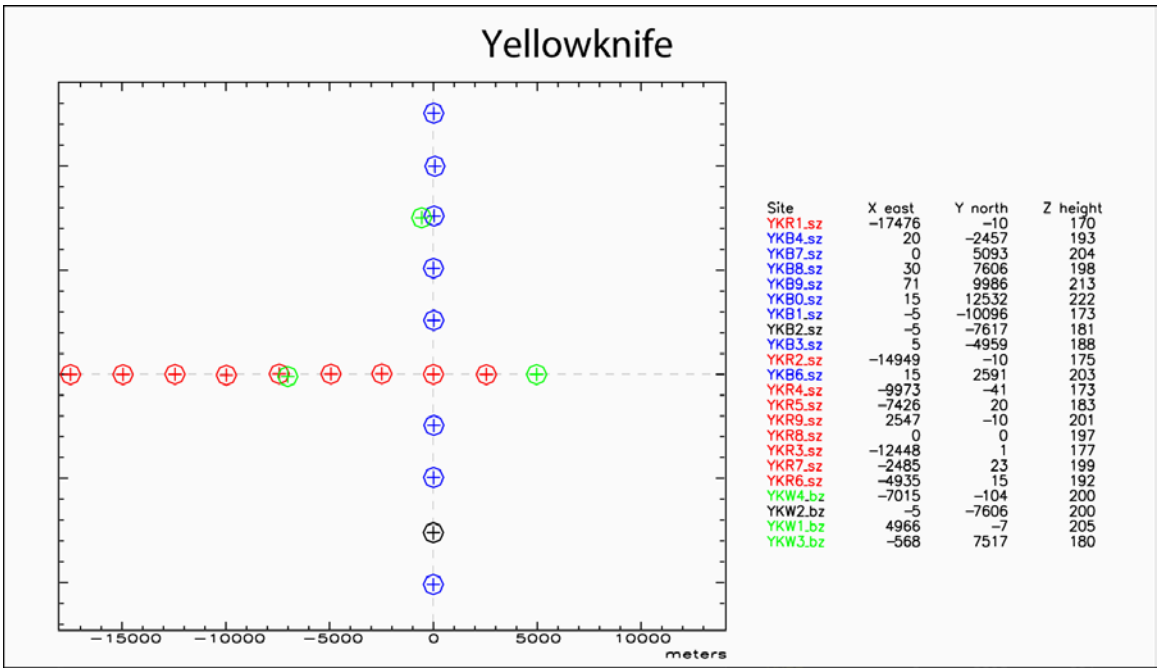

Fig. 9.1 Configuration of the UKAEA - type Yellowknife array (YKA) in Northern Canada**.** The blue and the red sites have vertical short-period instruments, while three-component, broadband seismometers are installed at the green sites. The center seismometer of YKA has the geographic coordinates 62.4932°N, 114.6053°W.

Since the 1950s, classified arrays deployed to monitor nuclear test activities at teleseismic distances had been built worldwide. Many of these arrays became known in the 1990s and are today part of the IMS as primary or auxiliary stations, e.g., AKASG (Malin, Ukraine), ASAR (Alice Springs, Australia), BRTR (Keskin, Turkey), CMAR (Chiang Mai, Thailand), ESDC (Sonseca, Spain), ILAR (Eielson, Alaska), and KURK (Kurchatov, Kazakhstan). Many of these arrays have quite diverse geometries and in some cases comprise different installations for short and long period signals (e.g., the Belbaşi and the Keskin array: Kuleli et al., 2001; Semin et al., 2011).

In the 1960s, arrays with very different apertures and geometries were tested, from small circular ones with apertures of a few kilometers to huge arrays with apertures of up to 200 km. The largest arrays were the Large Aperture Seismic Array (LASA: Frosch and Green, 1966) in Montana (USA), opened in 1965 and in operation until 1978 with 525 seismometer sites, and the original Norwegian Seismic Array (NORSAR: Bungum et al., 1971) in southern Norway, consisting of 132 sites over an aperture of approximately 100 km with altogether 198 seismometers, which became fully operational in spring 1971. The original NORSAR array was reduced in 1976 to seven subarrays (see Fig. 9.2) and was assigned the new code name NOA.

Figs. 9.2 and 9.3 show the configurations of the present day NORSAR (NOA) and NORES arrays and the layout of the seismometer sites for the ARCES array. The NORES and ARCES-type array design with sites located on concentric rings (each with an odd number of sites) spaced at log-periodic intervals is now used for most of the modern small aperture arrays; only the number of rings and the aperture (diameter of the outermost ring of sites) differ from installation to installation. For example, the SPITS array has only nine sites and

corresponds to the center site plus the A- and the B-ring of a NORES-type array; the FINES array in southern Finland consists of three rings with 16 sites altogether. The geometry of these regional, relatively small arrays was developed in the 1980s and 1990s. Today, the configuration of a SPITS-type 9-element array constitutes the standard for new arrays in the IMS, but in general with a larger aperture than SPITS.

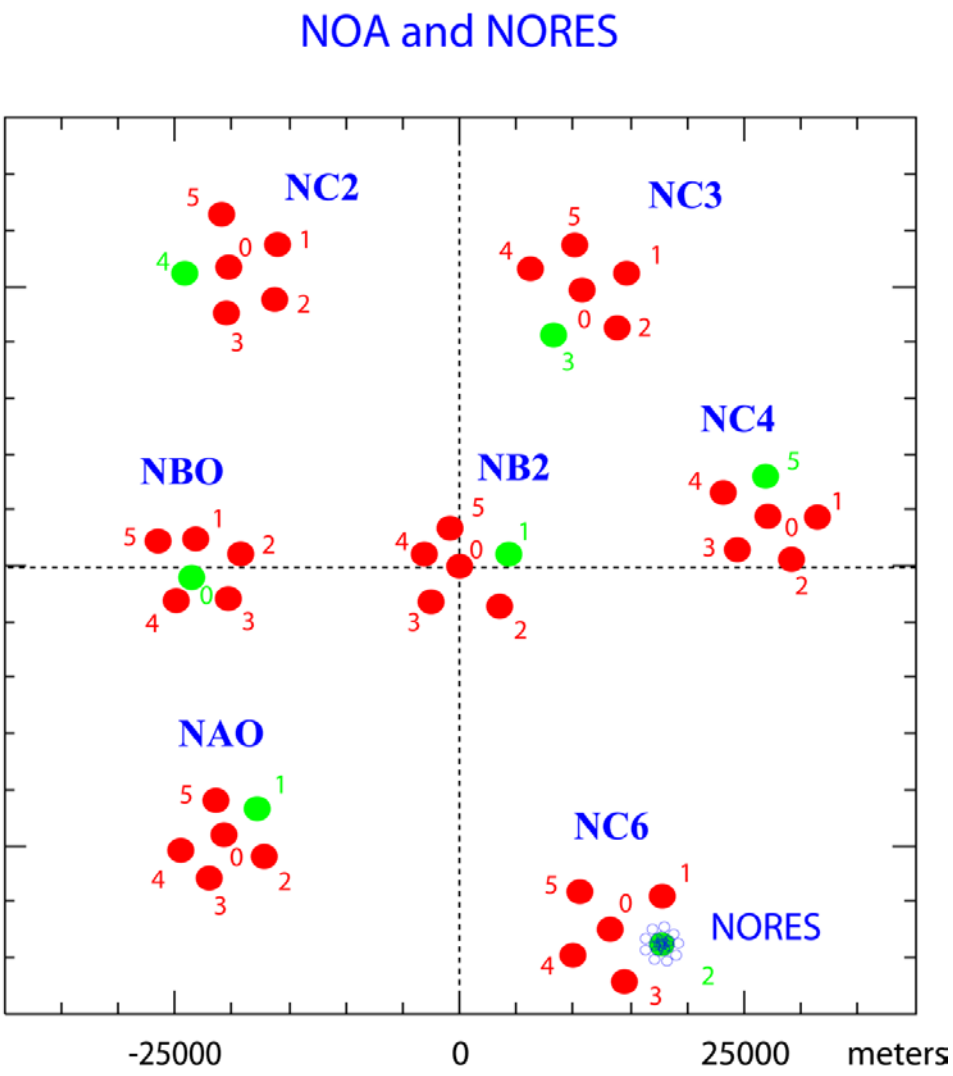

Fig. 9.2 Configuration of the present day large aperture NORSAR array (NOA) and the small aperture array NORES. The NORES array is co-located with the NORSAR subarray NC6. The aperture of NOA has, since 1976, been about 60 km and the aperture of NORES is about 3 km (see the small blue symbols). Each seismometer site is marked with a circle. The present NOA configuration has 42 sites, whereas the NORES array has 25 sites. NOA has seven subarrays, each with six vertical seismometers installed in shallow boreholes. In addition, one site in each subarray (marked in green) has one three-component broadband seismometer. The geometry of NORES is identical to the geometry of ARCES shown in Fig. 9.3. The center seismometer of NOA in subarray NB2 has the geographic coordinates 61.03972°N, 11.21475°E. The center seismometer of NORES has the geographic coordinates 60.73527°N, 11.54143°E.

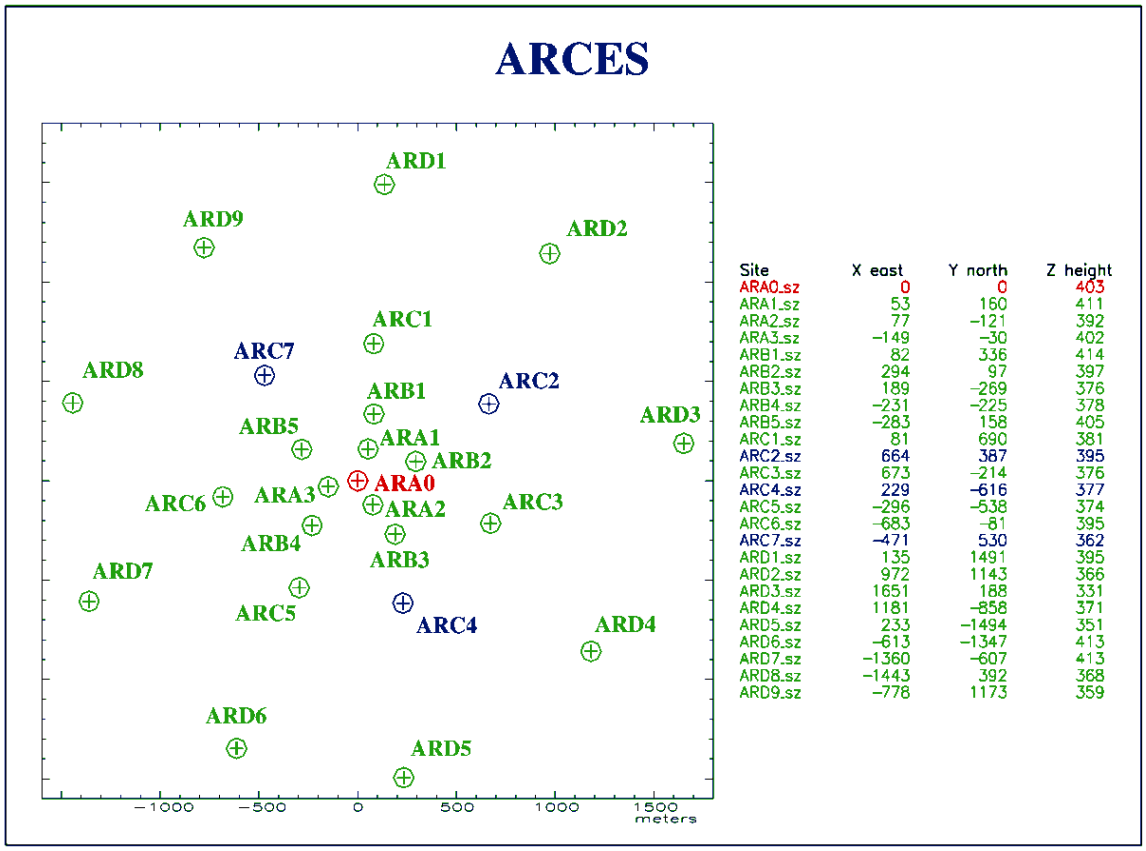

Fig. 9.3 Configuration of the regional array ARCES, which is identical to the NORES array. Each vertical short-period seismometer site is marked with a circle and a cross. The ARCES array has 25 sites with vertical short-period seismometers. Four of these sites have in addition short-period horizontal seismometers. These short-period three-component sites are marked in blue or red. A broadband three-component seismometer is co-located with the short-period three-component seismometer at the center site (red). ARCES has one center instrument – ARA0 – and four rings: the A-ring with three sites and a radius of about 150 m, the B-ring with five sites and a radius of about 325 m, the C-ring with seven sites and a radius of about 700 m, and finally, the D-ring with nine sites and a radius of about 1500 m. The center seismometer of ARCES has the geographic coordinates 69.53486°N, 25.50578°E. The table on the right of the figure gives the relative coordinates between the single sites and the center site ARA0, and the elevation of all sites above sea level in meters.

The large LASA and NORSAR arrays and the UKAEA arrays had narrow-band short-period seismometers at all sites and additional long-period seismometers at selected sites in their original configurations, whereas the Gräfenberg Array (GRF) in Germany was planned and installed in the early 1970s as an array of broadband sensors. It has an aperture of about 100 km (Harjes and Seidl, 1978; Buttkus, 1986) and an irregular shape (Fig. 9.4) that follows the limestone plateau of the Franconian Jura.

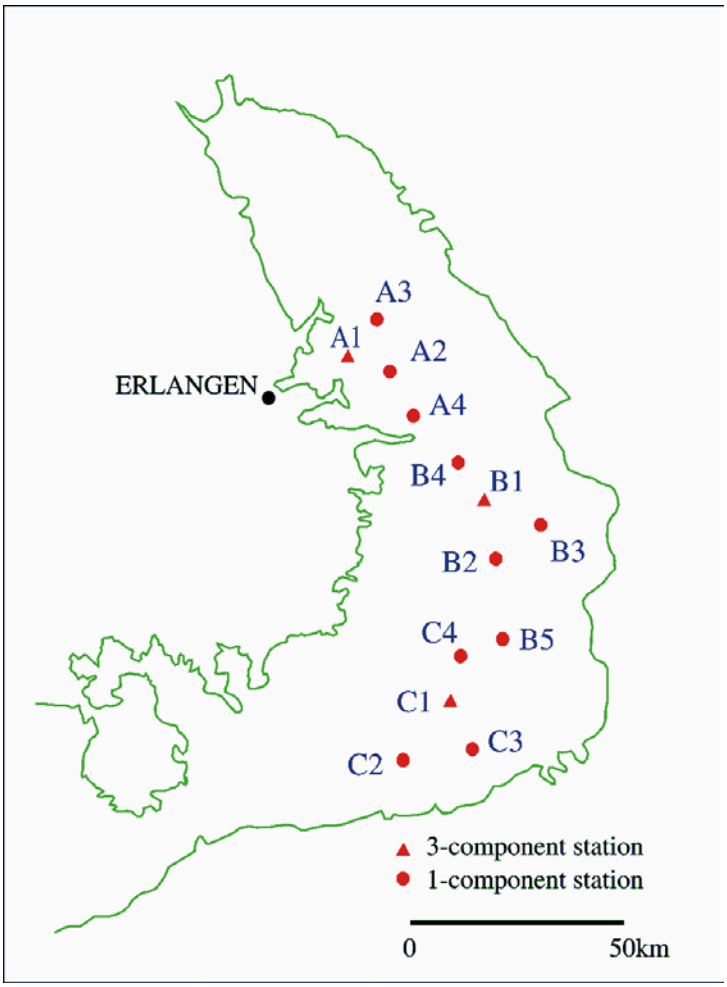

Fig. 9.4 Configuration of the irregularly shaped Gräfenberg array (GRF). Since several years, all sites are equipped with three-component, broadband STS-2 seismometers. The green line follows the geological unit Franconian Jura, on which the array is located. The reference station GRA1 (at position A1 on the map) has the geographical coordinates 49.69197°N and 11.22200°E.

Another approach to arrays was developed in the 1990s. In parts of Japan and in the USA the networks of seismometer stations are so dense that data from all stations can be combined and used as array data. Examples of these are the so-called J-array, the Californian array and the ongoing USArray project with semi-temporary stations (Levander et al., 1999). All known array techniques can be applied to analyze data from these networks (see e.g., J-array Group, 1993 or Benz et al., 1994).

9.4 Beamforming

With an array we can improve the signal-to-noise ratio (SNR) of a seismic signal by summing the coherent part of seismic signals as observed at the different single array sites. Figs. 9.5 and 9.6 show P onsets of a regional event observed at the ARCES sites and, in addition, the summation trace (on top) of all single observations divided by the number of traces. In Fig 9.5 the data were summed without taking into account any signal delay times between the

different stations due to finite apparent velocity of wave propagation. Consequently, the P onset is suppressed by destructive interference. In Fig. 9.6 all traces were time-adjusted to provide alignment of the first P pulse before summation. Note the clear and short P pulse on the beam trace and the suppression of incoherent energy in the P coda and preceding noise. In the following, all calculations of summation traces always includes as a last processing step the division of the summation trace by the number of traces summed up. This is done to conserve the amplitude of seismic signals for any later signal analysis.

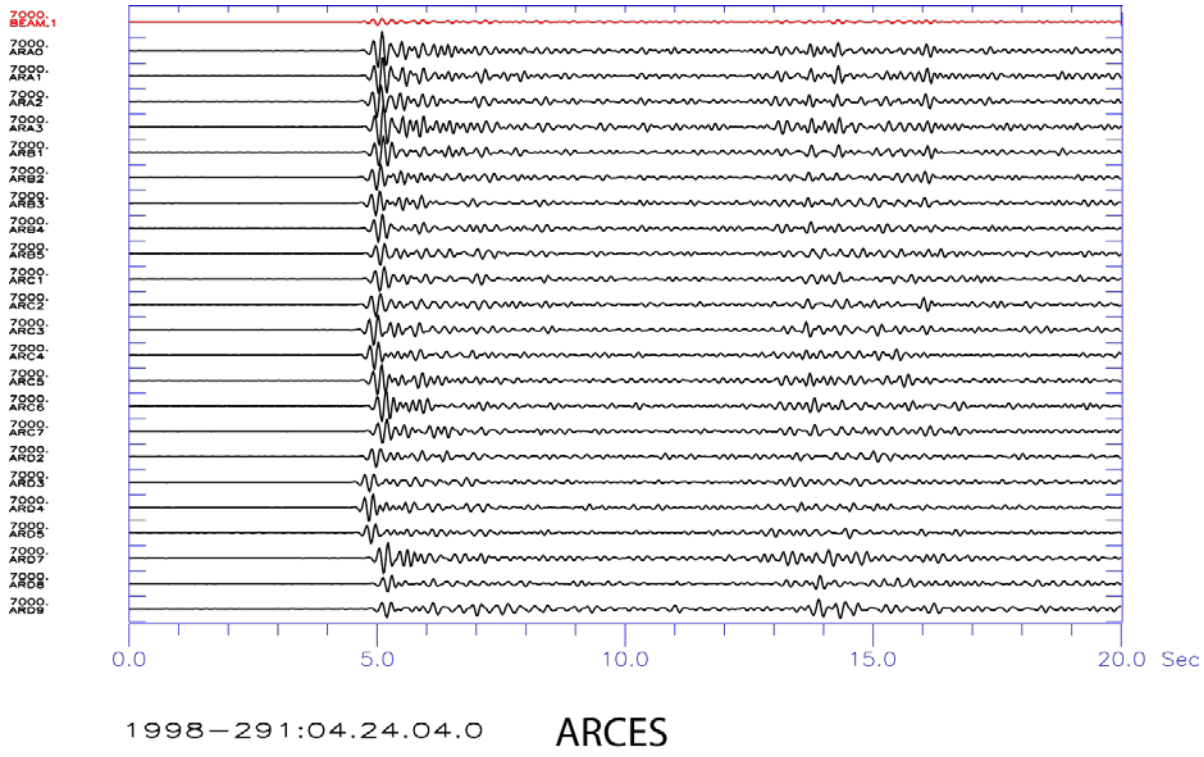

Fig. 9.5 The figure shows P-phase onsets of a regional event observed with the vertical short-period seismometers of ARCES. The top trace is an array beam, and the remaining traces are single vertical short-period seismograms. All data were filtered with a Butterworth band pass filter between 4 and 8 Hz and are shown with a common amplification. All traces were summed to create the beam, which was then divided by the number (23) of traces, without any delay-time application.

This demonstrates that the most significant consideration in the summation (or beamforming) process is to find the best delay times, with which the single traces must be shifted before summation ("delay and sum") in order to get the largest amplitudes due to coherent interference of the signals. The simplest way is just to pick the onset times of the signal on each trace and shift the traces with respect to the onset time at the reference site of the array. However, most onsets from weaker events have a much smaller SNR than in the example shown, and therefore onset times are often difficult to pick. With hundreds of onsets each day, this is not practical during routine operation. Therefore for routine processing of array data the best approach is to predefine many different beams and to calculate them automatically. A detector can then search for onsets on these beams.

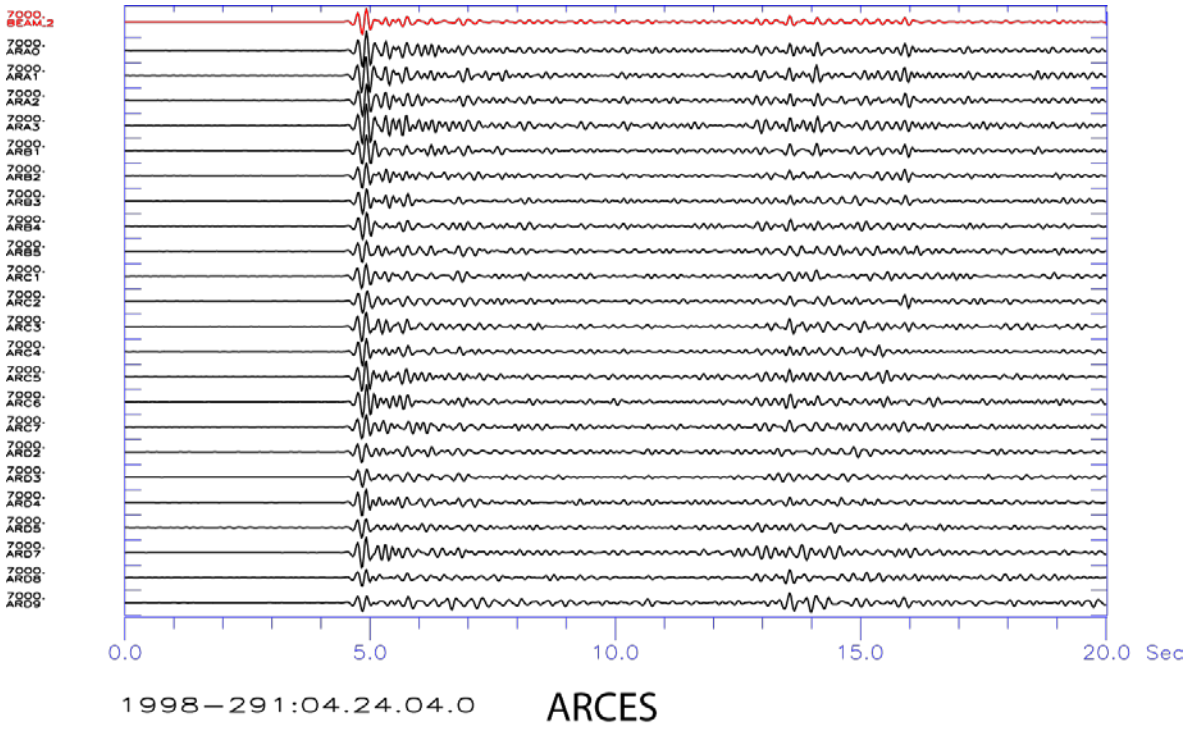

Fig. 9.6 This figure shows P-phase onsets of a regional event observed with the vertical short-period seismometers of ARCES as in Fig. 9.5 but the single traces were first aligned, summed up and then divided by the number of traces (23). Note for this case the clear and relatively short pulse form of the first P onset on the beam and the suppression of incoherent energy in the P coda.

In the following sections, we explain how such delay times can be theoretically calculated for known seismic signals, using some basic equations and parameter definitions, and we give the formulas for a seismic beam.

9.4.1 Geometrical parameters

As aforementioned, an array is defined as a set of seismometers with one seismometer site or any other location within or close to the array being assigned the role of a reference point. The relative distances from this reference point to all other array sites are used later in all array specific analysis algorithms (Fig. 9.7).

$\boldsymbol{r}_j$ Position vector of instrument j with a distance (absolute value) r_j from the defined reference point. We use bold characters for vectors and normal characters for scalars. The position is normally given relative to a (central) instrument at site O, $\boldsymbol{r}_j = f(x, y, z)$, where (x, y, z) are the Cartesian coordinates measured in [km] with positive axes towards East (x), towards North (y), and in the vertical up above sea level (z).

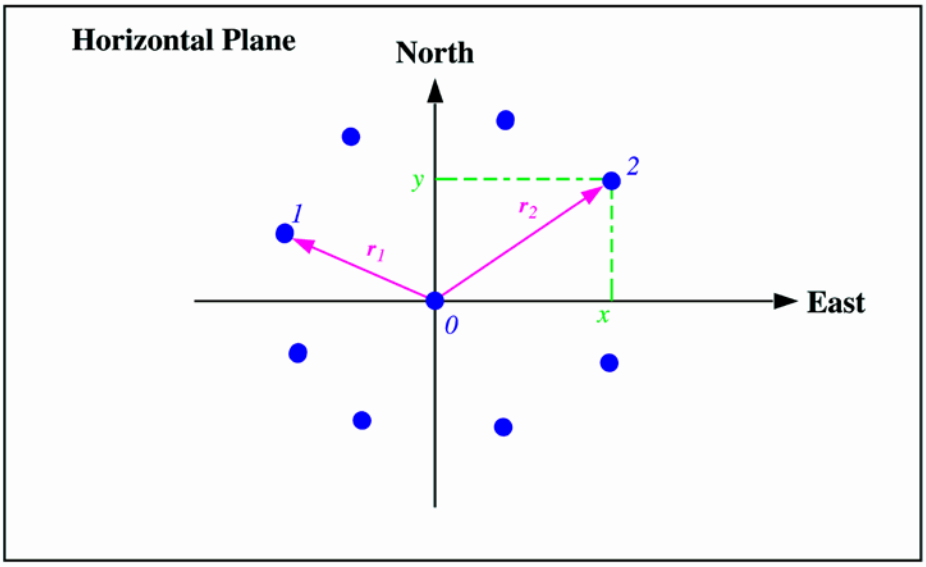

Fig. 9.7 Illustration (horizontal plane) of an array of instruments (filled circles). The center instrument *0* is used as reference and origin for the relative coordinates *x*, *y* (see also Fig. 9.3 for an example of such a circular array).

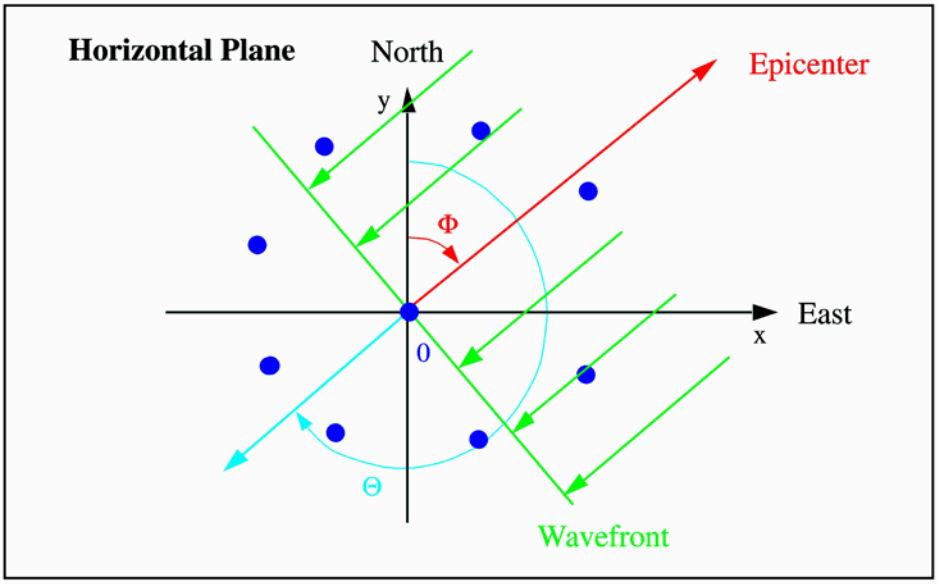

Fig. 9.8 Definition of the angles Θ (direction of wavefront propagation) and Φ (direction to the epicenter = backazimuth); here, e.g., for a wavefront coming from north-east and crossing the array in a south-westerly direction.

For distances from the source much larger than about 10 wavelengths, a seismic wave approaches an array as a **wavefront** that is close to **planar**. The case when the (simplified) plane-wave approach is no longer applicable and a circular wavefront has to be assumed is discussed in Almendros et al. (1999). The directions of approach and propagation of the wavefront projected on to the horizontal plane are defined by the angles Φ and Θ (Fig. 9.8).

Φ Backazimuth (often abbreviated as BAZ) = angle of wavefront approach, i.e., direction angle from a station to an epicenter, measured clockwise from the North to the direction towards the epicenter in [°]. In many cases this angle is for short called azimuth, but the recommendation is to use in all cases backazimuth to distinguish it from other azimuth measures.

Θ Direction in which the wavefront propagates, also measured in [°] from the North, with $\Theta = \Phi \pm 180°$.

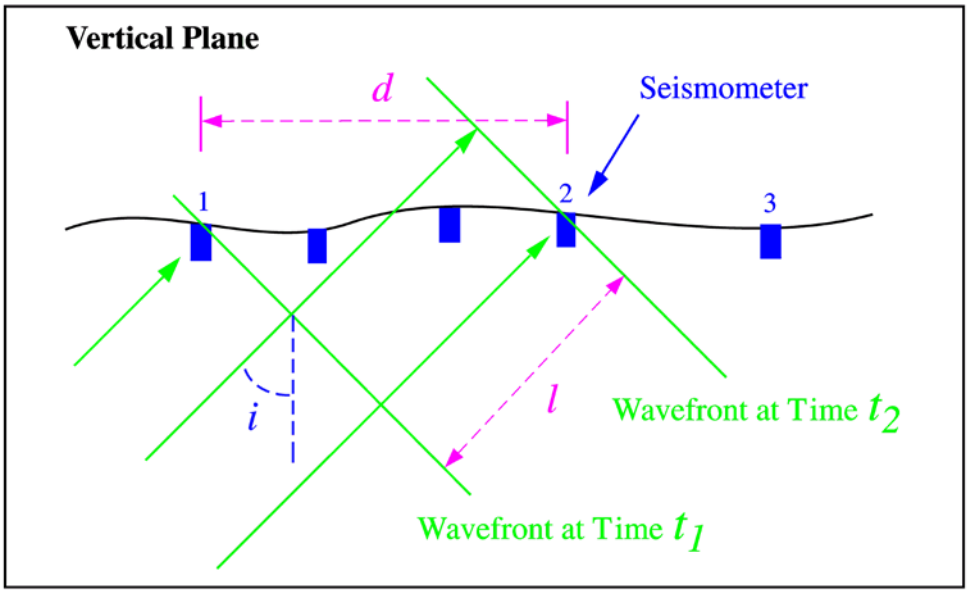

Fig. 9.9 Illustration (vertical plane) of a seismic plane wave crossing an array at an angle of incidence *i*.

In the vertical plane, the angle measured between the direction to the source and the vertical is called the angle of incidence *i* with $i \leq 90°$ (see Fig. 9.9). The seismic velocity below the array in the uppermost crust and the angle of incidence define the apparent propagation speed of the wavefront crossing the array. Be aware that the seismic velocity below the array is an effective mean velocity of the uppermost crustal layers depending on the dominant wavelength (frequency) of the seismic signal.

9.4.2 Apparent velocity and slowness

The upper crustal velocity together with the angle of incidence defines the apparent propagation speed of the wavefront at the observing instruments. This is **not** the physical propagation speed of the wavefront and is therefore called **apparent** velocity (see also Section 2.5.2 of Chapter 2). We start our consideration by defining the following quantities (for definition see Fig. 9.9):

d horizontal distances between different array sites in [km];
v_c effective, mean crustal velocity (for P or S waves, depending on the seismic phase) immediately below the array in [km/s];
i angle of incidence;

$\boldsymbol{v}_{app}$ apparent velocity vector with the absolute value $v_{app} = 1/s$. $\boldsymbol{v}_{app} = (v_{app,x}, v_{app,y}, v_{app,z})$, where $(v_{app,x}, v_{app,y}, v_{app,z})$ are the single apparent velocity components in [km/s] of the wavefront crossing an array;

v_{app} absolute value of the apparent velocity vector in [km/s] of a plane wave crossing an array (see Fig. 9.10);

$v_{app,h}$ absolute value of the horizontal component of the apparent velocity $v_{app,h} = \sqrt{v_{app,x}^2 + v_{app,y}^2}$.

The inverse of the apparent velocity v_{app} is called slowness *s*, which is a constant for a specific ray. For local or regional applications the unit of slowness is [s/km]. For global applications it is more appropriate to use the unit [s/°] and slowness is then called ray parameter. The ray parameter of major seismic phases is usually tabulated for standard Earth models together with the travel times as a function of distance from the source. The following symbols are used:

$\boldsymbol{s}$ slowness vector with absolute value $s = 1/v_{app}$. $\boldsymbol{s} = (s_x, s_y, s_z)$, where (s_x, s_y, s_z) are the single, inverse apparent velocity (= slowness) components in [s/km]. Note, because the vector $\boldsymbol{s}$ is oriented in the propagation direction (in direction of Θ = 225°, see Fig. 9.8), a plane wave with backazimuth Φ = 45° would have negative values for both horizontal components with North and East directions being positive;

s absolute value of the slowness vector in [s/km] of a plane wave crossing an array;

p ray parameter $p = s \cdot g$, measured in [s/°], for a spherical Earth model with a radius of 6371 km, where $g = \frac{\pi \cdot 6371\text{km}}{180°} \cong 111.19\ [\text{km}/°]$.

The relation between the parameters of a plane wave and the actual seismic signal is given by the wavenumber vector $\boldsymbol{k}$:

$\boldsymbol{k}$ wavenumber vector defined as $\boldsymbol{k} = \omega \cdot \boldsymbol{s}$ with the angular frequency $\omega = 2 \cdot \pi \cdot f = 2 \cdot \pi / T$ measured in [1/s]. *T* is the period and *f* the frequency of the seismic signal;

k absolute value of the wavenumber vector $\boldsymbol{k}$ defined as $k = \omega \cdot s = 2 \cdot \pi \cdot f \cdot s = 2 \cdot \pi / \lambda$, measured in [1/km]. λ is the wavelength of the signal and because of the analogy between ω and *k*, *k* is also called spatial frequency.

The time delay τ_j is defined as the arrival-time difference of the wavefront between the seismometer at site *j* and the seismometer at the reference site. The unit of measurement is seconds with a positive delay meaning a later arrival with respect to the reference site.

Assume a wavefront is propagating the distance *l* between time t_1 and time t_2 (Fig. 9.9). Then, if *d* is used for the horizontal distance between instrument 1 and 2 in [km], and if both instruments are assumed to be at the same elevation, we have:

$\tau_2 = (t_2 - t_1) = \frac{l}{v_c}$, and the horizontal component of the apparent velocity $v_{app,h}$ is then defined as a function of the incidence angle *i* (Fig. 9.10):

$$v_{app,h} = \frac{d}{(t_2 - t_1)} = \frac{v_c}{\sin i} \qquad v_{app,z} = \frac{v_c}{\cos i} \tag{9.1}$$

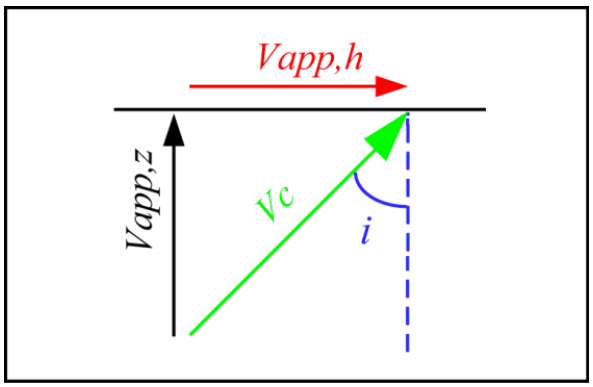

Fig. 9.10 A plane wave propagating in the direction of the green arrow with the velocity v_c reaches the Earth's surface. The decomposition of this velocity into a vertical ($v_{app,z}$) and a horizontal component ($v_{app,h}$) of the apparent velocity depends on the incidence angle i. The horizontal velocity component is only equal to the propagation velocity v_c for waves propagating parallel to the surface; in all other cases v_{app} is higher than v_c.

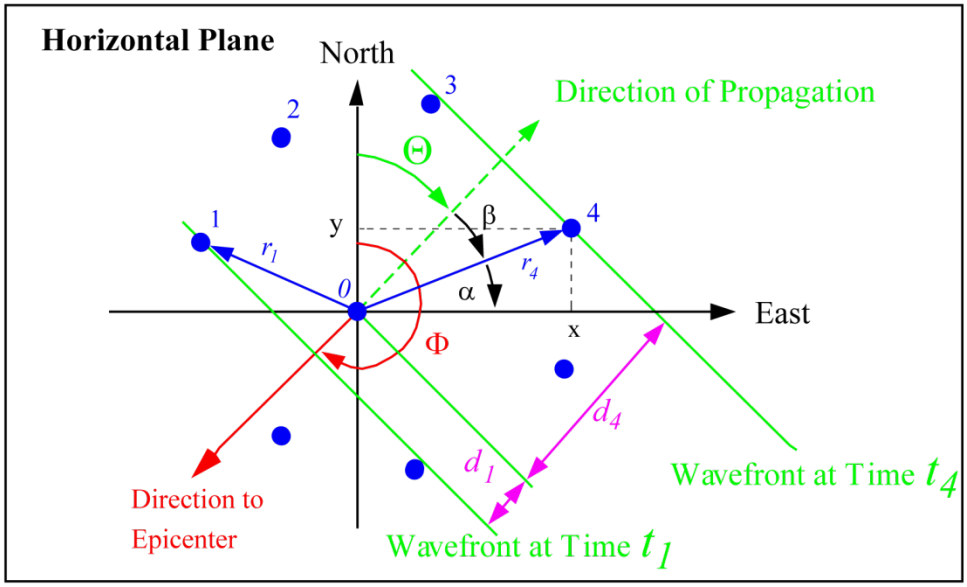

Fig. 9.11 Illustration (horizontal plane) of a plane wave, coming from the Southwest (backazimuth Φ), crossing an array and propagating in a north-easterly direction Θ.

9.4.3 Plane-wave time delays for sites in the same horizontal plane

In most cases, the elevation differences between single array sites are so small that travel-time differences due to elevation differences are negligible (Fig. 9.9). We can assume, therefore, that all sites are in the same horizontal plane. In this case, we cannot measure the vertical component of the wavefront propagation. The vertical apparent velocity component can then

be defined as $v_{app,z} = \infty$, and the corresponding slowness component becomes $s_z = 0$. From Fig. 9.11 we see that the time delay τ_4 [s] between the center site *0* and site *4* with the relative coordinates (x_4, y_4) is

$$\tau_4 = \frac{d_4}{v_{app,h}} = \frac{r_4 \cdot \cos\beta}{v_{app,h}}, \text{ with } r_4 = |\boldsymbol{r}_4|.$$

Now let us omit the subscript *4*, and evaluate further:

$$\alpha + \beta + \Theta = 90°, \quad r \cdot \cos\beta = d, \quad r \cdot \cos\alpha = x, \quad d = \frac{x \cdot \cos\beta}{\cos\alpha}$$

$$d = \frac{x \cdot \cos(90° - \alpha - \Theta)}{\cos\alpha} = \frac{x \cdot (\sin\alpha \cdot \cos\Theta + \cos\alpha \cdot \sin\Theta)}{\cos\alpha} = x \cdot \frac{\sin\alpha}{\cos\alpha} \cdot \cos\Theta + x \cdot \sin\Theta$$

$$d = x \cdot \frac{y}{x} \cdot \cos\Theta + x \cdot \sin\Theta = y \cdot \cos\Theta + x \cdot \sin\Theta$$

With $\Theta = \Phi \pm 180°$ (Fig. 9.8), we get for the horizontal distance traveled by the plane wave $d = -x \cdot \sin\Phi - y \cdot \cos\Phi$.

Then, for any site *j* with the horizontal coordinates (x, y), but without an elevation difference relative to the reference (center) site, we get the time delay τ_j:

$$\tau_j = \frac{d_j}{v_{app,h}} = \frac{-x_j \cdot \sin\Phi - y_j \cdot \cos\Phi}{v_{app,h}} \tag{9.2}$$

These delay times can also be written in vector syntax with the position vector $\boldsymbol{r}_j$ and the slowness vector $\boldsymbol{s}$ as parameters. In this notation the delay times are defined as projection of the position vector onto the slowness vector:

$$\tau_j = \boldsymbol{r}_j \cdot \boldsymbol{s} \tag{9.3}$$

9.4.4 Plane-wave time delays when including site elevations

In some cases, not all array sites are located on one horizontal plane. Then the calculation of the time delays becomes slightly more complicated. Site *2* (Fig. 9.12) has the relative coordinates (x_2, y_2, z_2) and we see that $i + \gamma + \varphi = 90°$, $z_2 = r_2 \cdot \sin\varphi$, $d_2 = r_2 \cdot \cos\varphi$, $l = r_2 \cdot \cos\gamma$, and $\tau_2 = \frac{l}{v_c}$.

$$l = \frac{z_2}{\sin\varphi} \cdot \cos\gamma = \frac{z_2}{\sin\varphi} \cdot \cos(90° - i - \varphi) = \frac{z_2 \cdot (\sin i \cdot \cos\varphi + \cos i \cdot \sin\varphi)}{\sin\varphi}$$

Omitting again the site number, we get:

$$l = z \cdot \frac{\cos\varphi}{\sin\varphi} \cdot \sin i + z \cdot \cos i = d \cdot \sin i + z \cdot \cos i$$

Using Eqs. (9.1) and (9.2), we get for the total time delay at site *j*

$$\tau_j = \frac{-x_j \cdot \sin i \cdot \sin\Phi - y_j \cdot \sin i \cdot \cos\Phi + z_j \cdot \cos i}{v_c} = \frac{-x_j \cdot \sin\Phi - y_j \cdot \cos\Phi}{v_{app}} + \frac{z_j \cdot \cos i}{v_c} \qquad (9.4)$$

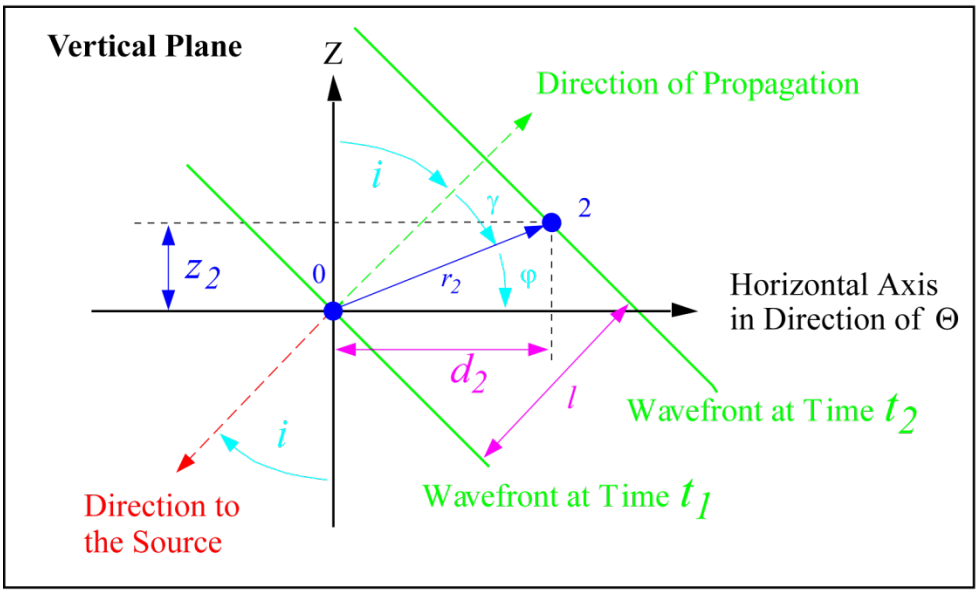

Fig. 9.12 Illustration (vertical plane) of a plane wave crossing an array at the angle of incidence *i*.

Now, the time delays τ_j also depend on the local crustal velocities (v_c) below the given site *j* and not just on the parameters of the wavefront (Φ, v_{app}). This is a clear disadvantage of arrays where single sites are not located on one horizontal plane, and if possible elevation variations should be avoided when planning a new array installation. Writing these time delays in vector notation will again result in Eq. (9.3), but note, the vectors are now three-dimensional.

$$\tau_j = \boldsymbol{r}_j \cdot \boldsymbol{s}$$

As rule of thumb one can use: elevation corrections should be applied whenever elevation related time delays between different array sites become equal or larger than about ¼ of the dominant signal period.

9.4.5 Beamforming formulae

After deriving the delay times τ_j for each station by solving Eq. (9.2) or Eq. (9.4) for a specific backazimuth and apparent velocity combination, we can define a "delay and sum" process to calculate the array beam. In the following we will use the shorter vector syntax of Eq. (9.3) to calculate time delays. The calculated delay times can be negative or positive. This depends on the relative position of the single sites with respect to the array's reference point and to the backazimuth of the seismic signal. Negative delay times correspond to a delay and positive delay times correspond to a signal arriving earlier than at the reference site.

Let $w_j(\boldsymbol{r_j}, t)$ be the digital sample of the seismogram from site *j* at time *t*, then the beam of the whole array is defined as

$$b(t) = \frac{1}{M}\sum_{j=1}^{M} w_j(t + \mathbf{r}_j \cdot \mathbf{s}) = \frac{1}{M}\sum_{j=1}^{M} w_j(t + \tau_j)\,. \tag{9.5}$$

This operation of summing the recordings of the *M* instruments by applying the time delays $\boldsymbol{r} \cdot \boldsymbol{s}$ and then dividing by the number of traces *M* is called beamforming.

Because we are using digital data, sampled with a defined sampling rate, we will always need an integer number of samples in programming Eq. (9.5), that is, the term $t + \boldsymbol{r_j} \cdot \boldsymbol{s} = t + \tau_j$ needs to be converted to an integer sample number. However, to avoid aliasing effects by following the rules of digital signal processing, it is in most cases sufficient for beamforming to use the nearest integer sample, as long as the dominant frequency is lower than ~25% of the sampling rate. If better resolution is needed one has to oversample the data. An example of the positive effects of oversampling is the beampacking algorithm (see section 9.8.2).

If seismic waves were harmonic waves *S(t)* without noise, with identical site responses, and without attenuation, then a "delay and sum" with Eq. (9.5) would reproduce the signal *S(t)* accurately. The attenuation of seismic waves within an array is usually negligible, but large amplitude differences can sometimes be observed between data from different array sites due to differences in the crust directly below the sites (see Fig. 4.34 in Chapter 4). In such cases, it can be helpful to normalize the amplitudes or to weight the traces before beamforming.

Real data *w(t)* are, of course, the sum of background noise *n(t)* plus the signal of interest *S(t)*, i.e., $w(t) = S(t) + n(t)$.

The actual noise conditions and signal amplitude differences will influence the quality of a beam. However, the noise is usually more incoherent than the signal, i.e., signal and noise will be influenced differently by beamforming. The improvement of the signal-to-noise ratio (SNR) due to the beamforming process can be estimated as follows:

Calculating the sum of M observations and including noise we get:

$$B(t) = \sum_{j=1}^{M} w_j(t + \boldsymbol{r}_j \cdot \boldsymbol{s}) = \sum_{j=1}^{M} (S_j(t + \boldsymbol{r}_j \cdot \boldsymbol{s}) + n_j(t + \boldsymbol{r}_j \cdot \boldsymbol{s}))\,.$$

Assuming that the signal is coherent and not attenuated, this sum can be split and we get:

$$B(t) = M \cdot S(t) + \sum_{j=1}^{M} n_j (t + \boldsymbol{r}_j \cdot \boldsymbol{s}) \,. \tag{9.6}$$

Now we assume that the noise $n_j(\boldsymbol{r}_j, t)$ has a normal amplitude distribution, a zero mean value, and the same variance σ^2 at all M sites. Then, for the variance of the noise after summation, we get $\sigma_s{}^2 = M \cdot \sigma^2$ and the standard deviation of the noise in the beam trace will become $\sqrt{M} \cdot \sigma$. That means that the standard deviation of the noise will be multiplied only with a factor of $\sqrt{M}$, but the coherent signal with the factor M (Eq. (9.6)). So, the theoretical improvement of the signal-to-noise ratio (SNR) by the "delay and sum" process will be $\sqrt{M}$ for an array containing M sites. The SNR improvement, also called array gain G, of an M-sensor array can then be written as

$$G^2 = M \quad \text{or} \quad G = \sqrt{M} \,. \tag{9.7}$$

9.4.6 Examples of beamforming

In the following, two examples of beamforming are shown with data from the small aperture, short-period arrays NORES and GERES. With sampling rates of 40 Hz, these arrays are optimized to observe seismic phases at regional distances. A further advantage of these arrays is the relatively large number of 25 array elements, which can theoretically give an array gain (SNR improvement) of up to G = 5.

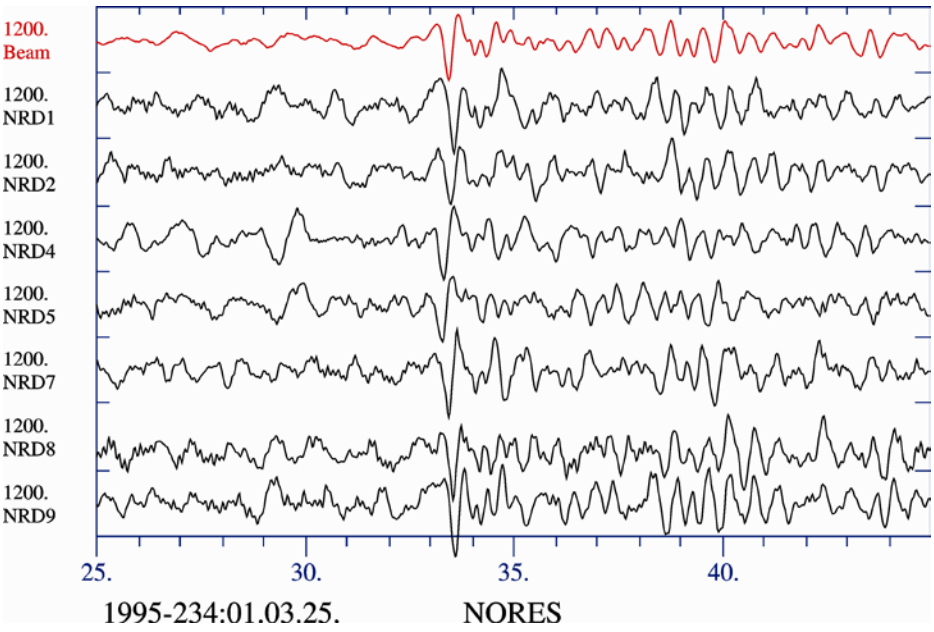

Fig. 9.13 Selected unfiltered NORES channels recording an event in Greece, with the beam displayed in red at top. All traces have the same amplitude scale and the unit of the time scale is in [s].

In Fig. 9.13 (top trace), we display a beam calculated by using the known apparent velocity (v_{app} = 10.0 km/s) and backazimuth (BAZ = 158°) for the P-onset of an event in Greece

recorded at NORES at an epicentral distance of 21.5°. 21 vertical sensors of the array have been used, but only the data recorded with the NORES D-ring elements are displayed together with the beam. Note that the signal on the beam is very similar to the individual signals, but the noise changes both in frequency content and amplitude level. The beam is made by calculating time delays for the given slowness and applying Eq. (9.2), and the individual traces have been shifted with these delays. There is an obvious SNR improvement (e.g., between the trace NRD8 and the beam of 2.98) but clearly less than the theoretical optimum of 4.58 times. This can have several reasons, such as:

- Non-optimum calculation of the time delay due to deviation from the assumed planar wave due to velocity anomalies below the array and along the ray path;
- The influence of lateral heterogeneities on the pulse shape of the signal at the different array sites due to multipathing, scattering or signal damping;
- Destructive interference of the noise may not work as theoretically assumed because the mean noise level at the different sites is very different;
- The noise at the different sites is not statistically independent but may have coherent components (Braun and Schweitzer, 2008).

Some approaches to further increase the SNR during beamforming of real data are described under Section 9.5.

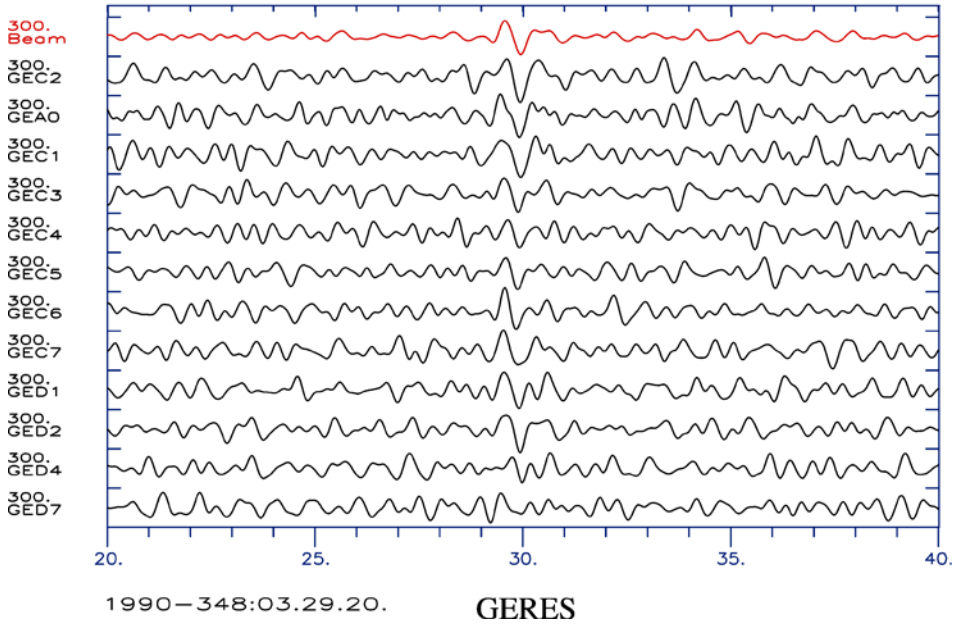

Fig. 9.14 GERES beam (top trace) in red for a PcP onset observed at an epicentral distance of 9.6° from a deep focus event in the Tyrrhenian Sea. All traces are 1 – 3 Hz bandpass filtered and have the same amplitude scale and the unit of the time scale is in [s].

The next example in Fig. 9.14 demonstrates the ability of arrays to detect small signals that are difficult to detect with single stations. It shows the tiny onset of the core reflection PcP recorded at the GERES array from a deep focus event in the Tyrrhenian Sea (h = 275 km) at an epicentral distance of 9.6°. For the "delay and sum" process, data from 20 sites of GERES were used (with only a subset of the single traces shown). Note that although the signal coherency is low, because of the large superimposing noise amplitudes, the noise suppression on the beam is clearly visible. In this case, the SNR improvement is also less than

theoretically expected (e.g., 3.9 between GEC3 and the beam trace instead of the theoretical value of 4.5) but the onset can now be analyzed.

9.5 Data analysis with beamforming

9.5.1 The n-th root process

A non-linear method to enhance the SNR during beamforming is the so-called n-th root process (Muirhead, 1968; Kanasewich et al., 1973; Muirhead and Ram Datt, 1976). Before summing up the single seismic traces, the n-th root is calculated for each trace retaining the sign information; Eq. (9.5) then becomes:

$$B_N(t) = \frac{1}{M}\sum_{j=1}^{M}\left|w_j(t+\tau_j)\right|^{1/N} \cdot signum\{w_j(t)\}, \tag{9.8}$$

where the value of the function $signum\{w_j(t)\}$ is defined as -1 or +1, depending on the sign of the actual sample $w_j(t)$. After this summation, the beam has to be raised to the power of *N*, again retaining the sign information:

$$b_N(t) = \left|B_N(t)\right|^N \cdot signum\{B_N(t)\} \tag{9.9}$$

N is an integer (*N* = 2, 3, 4, ...) that has to be chosen by the analyst. The n-th root process weights the coherency of a signal higher than the amplitudes, which results in a distortion of the waveforms: the larger *N*, the less the original waveform of the signal is preserved. However, the suppression of uncorrelated noise is better than with linear beamforming.

9.5.2 Weighted stack methods

Schimmel and Paulssen (1997) introduced another non-linear stacking technique to enhance signals through reduction of incoherent noise, which shows a smaller waveform distortion than the n-th root process. In their method, the linear beam is weighted with the mean value of the so-called instantaneous phase of the actual signal. The phase term itself follows a power law, which can be defined by the analyst. With this phase-weighted stack all phase-incoherent signals will be suppressed and small coherent signals will be relatively enhanced.

Instead of the instantaneous phase, Kennett (2000) proposed the use of the semblance of the signal as a weighting function. He applied this approach not only on one (vertical) component of the observed wave field but also jointly on all three components taking into account the cross-semblance between the three components of ground movement. He achieved a resolution similar to what is achieved with the method of Schimmel and Paulssen (1997).

An easily implementable weighted stack method would be to weight the amplitudes of the single sites of an array with the SNR of the signal at this site before beamforming, but this does not directly exploit the coherency of the signals across the array. All described stacking methods can increase the slowness resolution of vespagrams (see Section 9.8.4).

9.5.3 The double beam technique

Spudich and Bostwick (1987) applied the principal of reciprocity and used a cluster of earthquakes as a source array to analyze coherent signals in the seismic coda. This idea was consequently expanded by Krüger et al. (1993) who analyzed seismic array data from well-known source locations (i.e., mostly explosion sources) with the so-called “double beam method”. Here the principle of reciprocity is used for source and receiver arrays to further increase the resolution and the SNR for small amplitude signals by combining both arrays in a single analysis.

9.5.4 Time delay corrections

Calculating time delays using $\tau_i = \boldsymbol{r}_i \cdot \boldsymbol{s}$ is a simplification, often ignoring both elevation differences between the instruments and the fact that seismic waves are not perfect plane waves when crossing an array. To compensate for this, we have to introduce a correction $\Delta\tau_i$. Calculating time delays as done in Section 9.4.4 will compensate for deviations due to elevation differences (see Fig. 9.15). However, deviations from a plane wave may also be due to lateral heterogeneities below the array and if known, time corrections may improve the conformance between observed and theoretically predicted time delays.

For the large NORSAR array (NOA) e.g., elevation corrections are not used for beamforming. Instead, a database with empirical time delay corrections $\Delta\tau_{i,l}$ was established that corrects for both elevation differences and inhomogeneities, and this database is still in use (Berteussen, 1974). So, for all beamforming, including each point in the beampacking process (see Section 9.8.2), the delays $\Delta\tau_i$ of Eq. (9.3) are corrected according to Eq. (9.10). Note that the corrections depend on the slowness $\boldsymbol{s}_l$ of the signal.

$$\tau_i = \mathbf{r}_i \cdot \mathbf{s}_l + \Delta\tau_{i,l} . \tag{9.10}$$

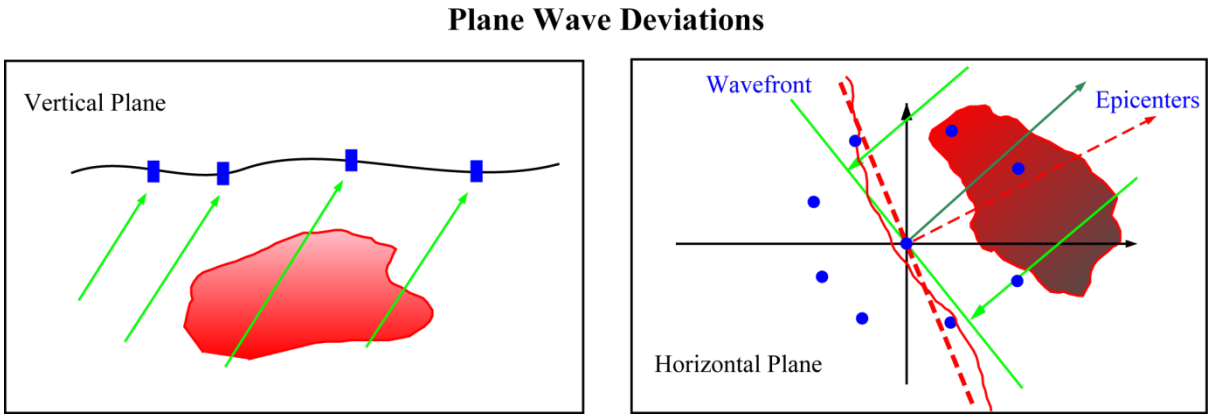

Fig. 9.15 This figure illustrates how lateral heterogeneities below an array (reddish areas) can disturb the propagation of seismic waves. Instead of a plane wave (green line on the right figure) a curved wavefront (red line) is passing the array and then (wrongly) interpreted as a plane wave (broken red line). The theoretically expected plane wave would be the green line.

A method to determine velocity heterogeneities by inverting such deviations of observed onset times from the theoretical plane wave was developed at NORSAR, the so-called ACH method (Aki, Christoffersson, and Husebye, 1977; Christoffersson and Husebye, 2011).

9.6 Beamforming and detection processing

A major task in processing seismic data is that of detecting possible signals in the data samples collected at the seismometers. A "signal" is defined to be distinct from the background noise due to its amplitude, different shape, and/or frequency content; in other words, the variance of the time series is increased when a signal is present. Statistically, we can form two hypotheses: the observation is noise or the observation is a signal plus noise. As aforementioned, the seismic signal observed at different sites of an array should be more coherent than random noise. If we assume that the time series recorded are independent measurements of a zero-mean Gaussian random variable, then it can be shown that the hypothesis of the recording being noise can be tested by measuring the power within a time window. If this power exceeds a preset threshold, then the hypothesis is false, i.e., the recording is signal plus noise. In practice, the threshold cannot be calculated precisely and may vary with time as is true for the background noise. An approximation to such a detector in seismology is to estimate the signal power over a long time interval (LTA = Long Term Average), and also over a short time interval (STA = Short Term (power) Average). The ratio STA/LTA, which is usually called signal-to-noise ratio (SNR), is compared with a preset threshold. If the SNR is larger than this threshold, the status of detection is set to "true" and we are speaking about a detected seismic signal.

This kind of an STA/LTA detector, proposed by Freiberger (1963), was installed and tested to our knowledge for the first time at LASA (van der Kulk et al., 1965), and later at Yellowknife (Weichert et al., 1967) and at NORSAR (Bungum et al., 1971). For complementary details on the STA/LTA trigger algorithm and its parameter settings in general, see IS 8.1. To calculate the STA, we can use a sum of the absolute values rather than the squared values (power) for computational efficiency; the difference in performance is minimal and the results are slightly more robust. The definition of the short-term average (STA) of a seismic trace $w(t)$ is:

$$STA(t) = \frac{1}{L} \cdot \sum_{j=0}^{L-1} \left| w(t-j) \right| \qquad L = sampling\ rate \cdot STA\ window\ length\,, \tag{9.11}$$

the recursive definition of the long-term average (LTA) is:

$$LTA(t) = 2^{-\varsigma} \cdot STA(t-\varepsilon) + (1-2^{-\varsigma}) \cdot LTA(t-1)\,, \tag{9.12}$$

where ε is a time delay, typically a few seconds, and ζ is a steering parameter for the LTA update rate. The parameter ε is needed to prevent a too early influence of the often-emergent signals on the LTA. In the case of a larger signal, the LTA may stay too long at a relatively high level and we will therefore have problems detecting smaller phases shortly after this large signal. Therefore, the LTA update is forced to lower the LTA values again by the exponent ζ.

Then the signal-to-noise ratio (SNR) is defined as:

$$SNR(t) = STA(t)/LTA(t)\,. \tag{9.13}$$

The STA/LTA operator may be used on any type of seismic signals or computed traces. That means, the input time series $w(t)$ may be raw data, a beam, filtered data or a filtered beam. L is the number of points of the time series $w(t)$ to be integrated. The recursive formulation for calculating the LTA means that the linear power estimate of the noise is based mainly on the last minute's noise situation, which is a very stable estimate. The influence of older noise conditions on the actual LTA value and a weighting of the newest STA value can be defined by the parameter ζ, for which, e.g., at NORSAR, a value of about 6.0 is used for STA update rates of about 0.2 seconds. It is also advisable to implement a delay of $\varepsilon = 3 - 5$ seconds for updating the LTA as compared to the STA. A simpler implementation is to estimate the LTA according to Eq. (9.11), but using an integration length that is 100 or 200 times longer for the LTA than for the STA. However, when detecting signals with frequencies above 1 Hz, it is also recommended that the LTA should not be updated while the SNR is above the detection threshold. This feature is easier to implement by using Eq. (9.12). Further details about the SNR and its improvement can be found in Section 4.4 of Chapter 4.

Figs. 9.16 and 9.17 demonstrate how the STA/LTA detector works for a single seismogram. The direct P onset of this regional event is sharp and detected clearly (Fig. 9.16). However, the P coda increases the background noise for later phases and the SNR of these phases becomes very small (Fig. 9.17). In this case, the advantages of using an array to detect seismic signals can be demonstrated easily. The apparent velocities of the P onsets and the S onsets are so different that calculating the corresponding S beam will decrease the P-phase energy and amplify the S-phase energy (Fig. 9.18).

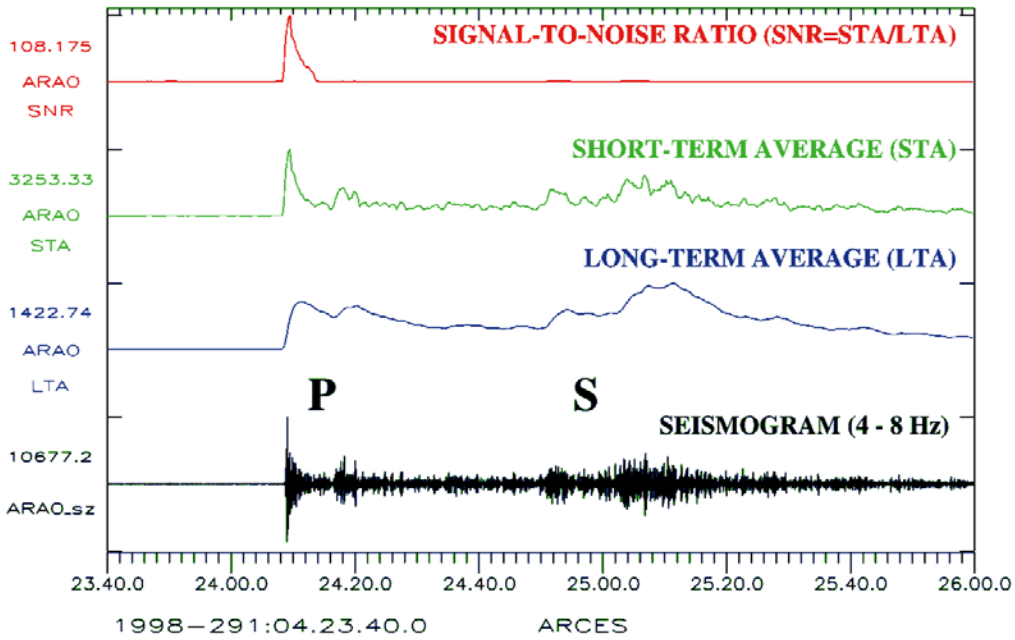

Fig. 9.16 LTA, STA and STA/LTA (= SNR) traces for a seismogram of a regional event observed at the ARCES reference site ARA0 (bottom). The seismogram was bandpass filtered between 4 and 8 Hz. Note the sharp onset for the P phase with an SNR of 108.175.

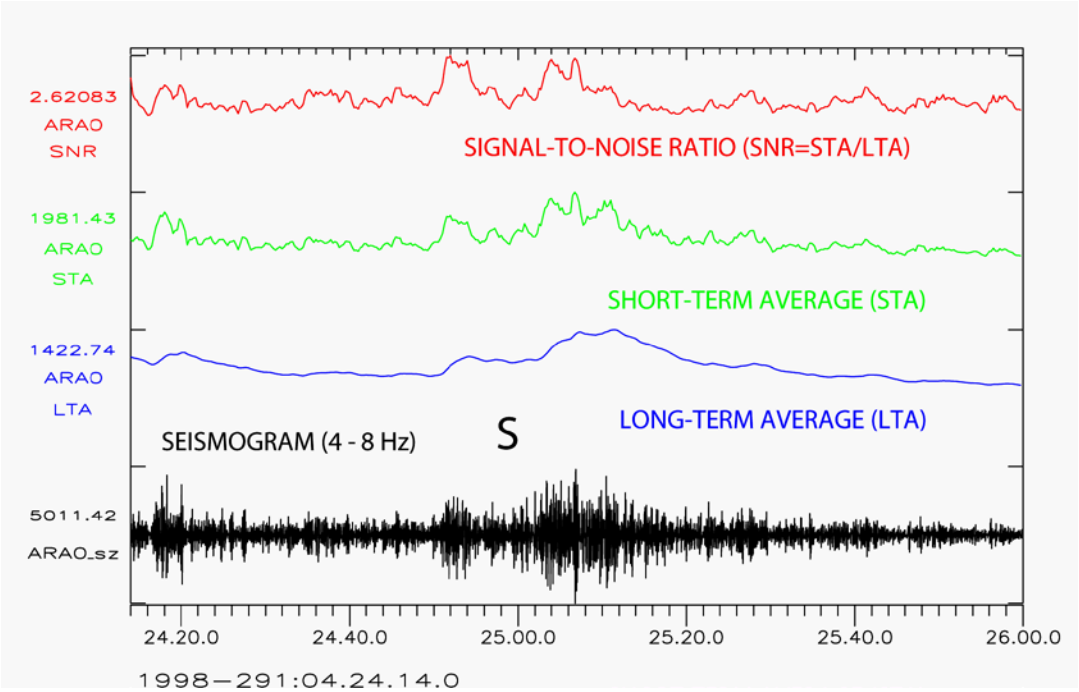

Fig. 9.17 As Fig. 9.16, but only for the time window after the P onset. Note that due to the P coda the noise and consequently the LTA is increased. Therefore the SNR of the S-phase onsets becomes relatively small on this single vertical trace.

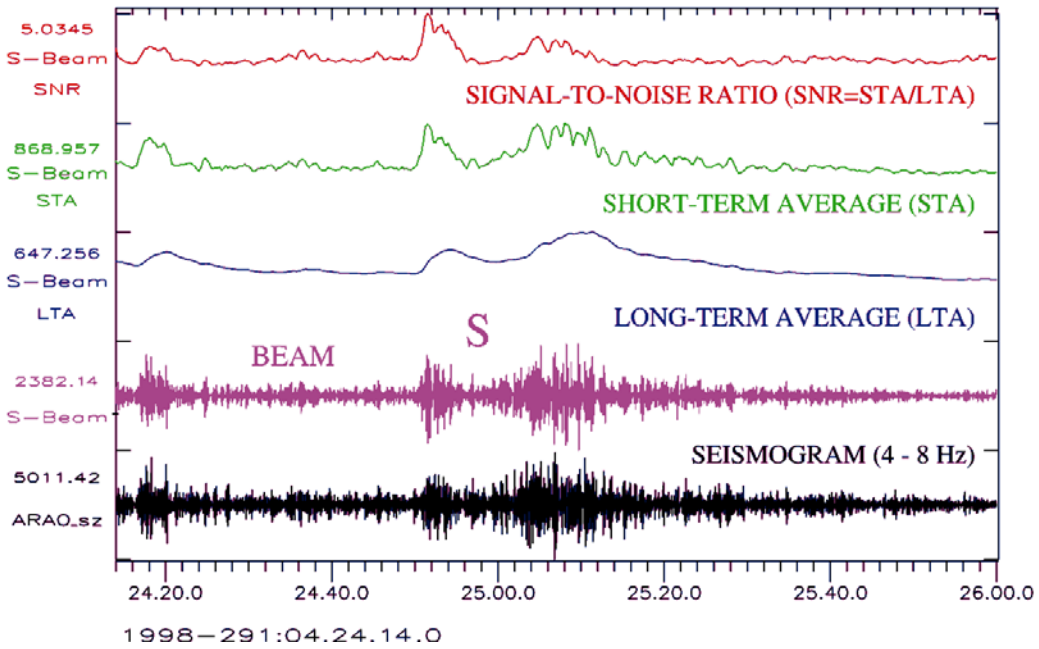

Fig. 9.18 As Fig. 9.17, but with LTA, STA and SNR calculated for a beam optimized for the first S onset. The array beam is shown as the second trace from the bottom. Compare the relative amplitudes of the P-coda on the array beam and on the single station seismogram at ARA0, which is shown at the bottom (note the different scaling factors to the left of the traces).

In Fig. 9.19 we display again the Greek event from Fig. 9.13 with the "best" beam (v_{app} = 10.0 km/s, backazimuth 158°) on top, together with beams using the same apparent velocity of 10.0 km/s but different backazimuths (0.0°, 90.0°, 180.0° and 270.0°). Note the difference in amplitudes of the beams for signal and noise. Because the "best" backazimuth of 158° is relatively close to 180.0°, the top trace and the second trace from the bottom differ only slightly. Thus, Fig. 9.19 demonstrates **resolution limits** for small aperture arrays like NORES. To find the "best" beam is, in principle, a matter of forming beams with different slowness vectors and comparing the amplitudes or the power of the beams, and then finding which v_{app}-backazimuth combination gives the highest signal energy on the beam.

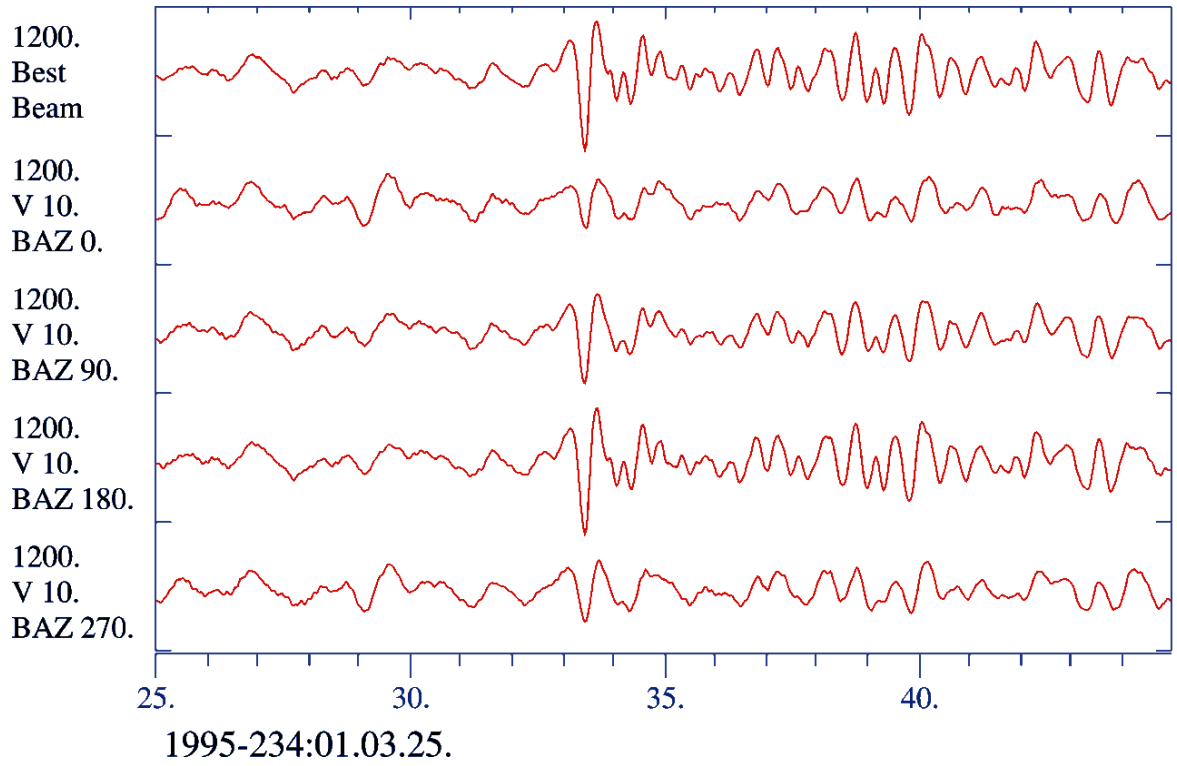

Fig. 9.19 NORES beams for the same event as in Fig. 9.13 with different slownesses. At top we plot again the best beam of Fig. 9.13. The other four traces are NORES beams of the same data now calculated by applying a constant apparent velocity of 10 km/s and different backazimuths (BAZ). The traces are unfiltered and are plotted with an equal amplitude scale.

In Fig. 9.20, the same beams as in Fig. 9.19 are shown, but now filtered using a Butterworth 3rd order bandpass filter between 2 and 4 Hz. When beamforming using Eq. (9.5), we can either filter all the individual traces first and then beamform, or we can beamform first, and then filter the beam, which is faster by a factor of the number of sites minus one. Both procedures should theoretically give the same result because both beamforming and filtering are linear processes. However, locally increased noise levels at single sites can make it useful to filter the single traces first to avoid leakage of low frequency energy when using tools containing Fourier analysis applications.

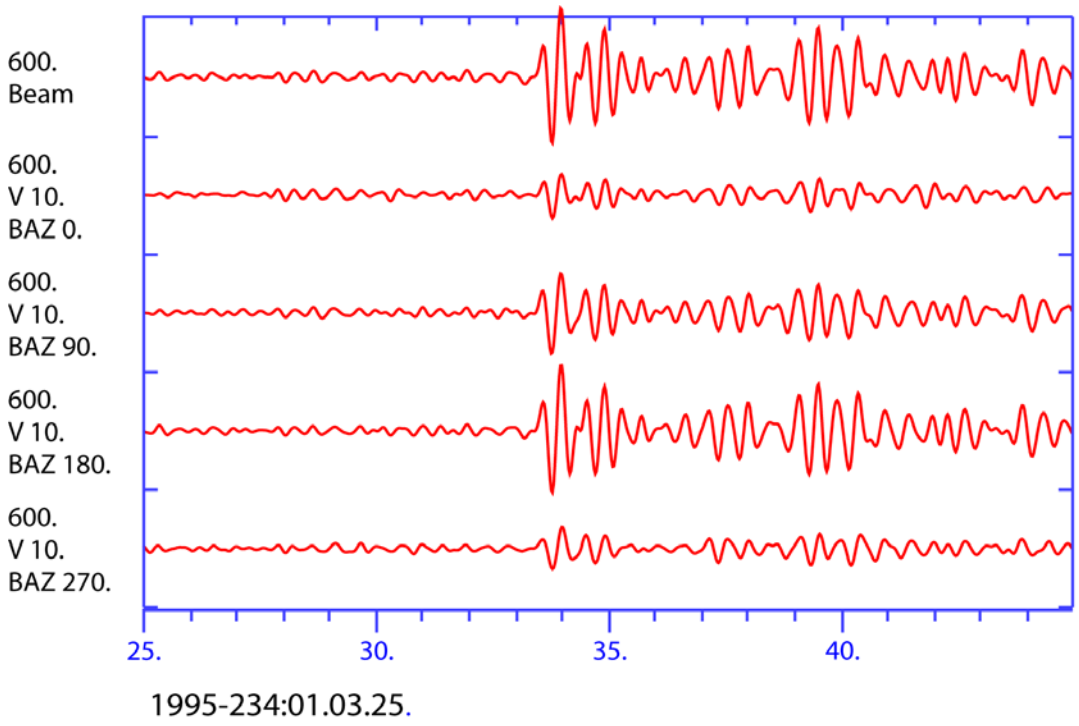

Fig. 9.20 This figure shows the same beams as in Fig. 9.19 but filtered with a Butterworth bandpass filter between 2 and 4 Hz. All traces have an equal amplitude scale.

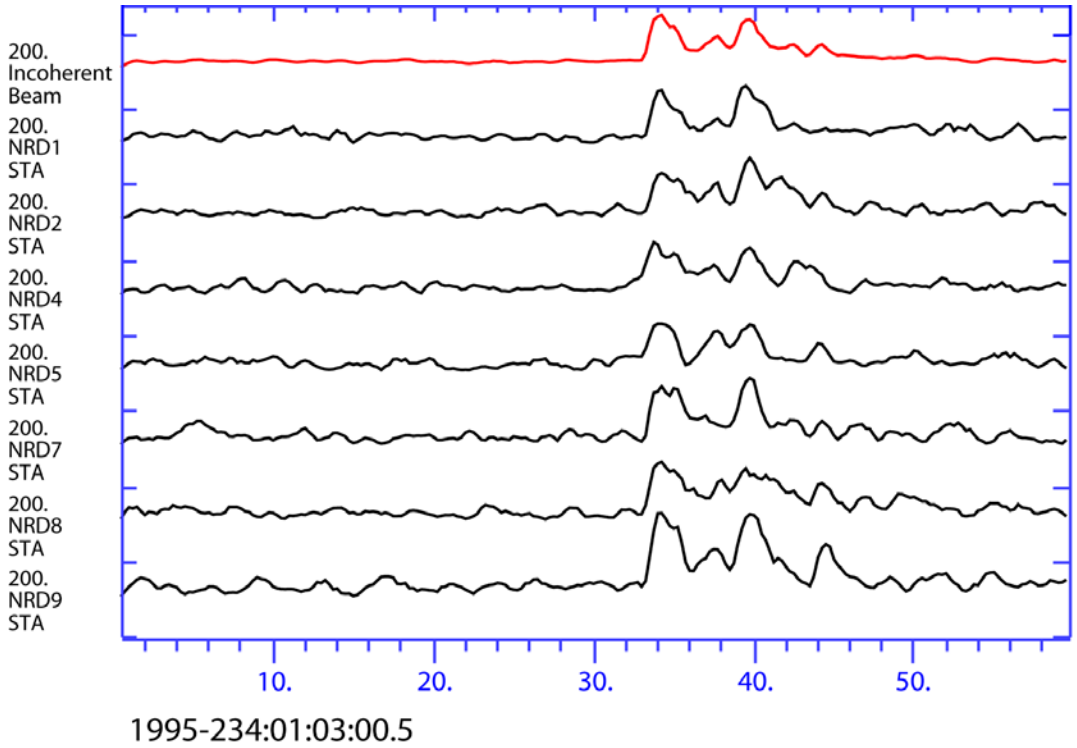

Fig. 9.21 Illustration of an incoherent beam (see text) which is shown on top in red. The other traces are STA time series. The selected NORES channels have been pre-filtered with a Butterworth bandpass filter between 2 and 4 Hz. All traces have an equal amplitude scale.

Fig. 9.21 (top trace) shows an incoherent beam, made by first filtering the raw data, then computing STA time series of each trace and afterwards, summing up the STA traces. The STA traces can be time shifted using time delays for a given slowness vector, but for detection purposes, when using a small aperture array, this is not necessary since the time shifts will be very small compared to the envelope of the signal. An incoherent beam will reduce the noise variance and can be used to detect signals that are incoherent across an array. Such incoherent signals are typically of higher frequency. When calculating incoherent beams, filtering must (!) be the first step.

9.7 Array transfer function

The array transfer function describes sensitivity and resolution of an array for seismic signals with different frequency contents and slownesses. When digitizing the output from a seismometer, we are sampling a seismic signal in the time domain, and to avoid aliasing effects, we need to apply an anti-aliasing filter. Similarly, when observing the wavefront of a seismic signal using an array, we obtain a spatial sampling of the ground movement. With an array, or a dense network, we are able to observe the wavenumber $k = 2\pi/\lambda = 2\pi \cdot f \cdot s$ of this wave defined by its wavelength λ (or frequency *f*) and its slowness *s*. While analog-to-digital conversion may give aliasing effects in the time domain, the spatial sampling may give aliasing effects in the wavenumber domain. Therefore the wavelength range of seismic signals, which can be investigated, and the sensitivity at different wavelengths must be estimated for a given array.

A large volume of literature exists on the theory of array characteristics, e.g., Barber (1958; 1959), Somers and Manchee (1966), Haubrich (1968), Doornbos and Husebye (1972), Harjes and Henger (1973), Harjes and Seidl (1978), Mykkeltveit et al. (1983; 1988), Johnson and Dudgeon (1993; 2002), Harjes (1990), and Wang (2002), but array theory can also be found in seismological textbooks (e.g., Capon, 1973; Aki and Richards, 1980; Bullen and Bolt, 1985; Buttkus, 2000; Kennett, 2002). We will describe in the following how the array transfer function can be estimated.

Assuming a noise and attenuation free plane-wave signal, the difference between a signal *w* at the reference site A and the signal w_n at any other sensor A_n is only the travel time between the arrivals at the sensors. As we know from Section 9.4, a plane wave is defined by its propagation direction and its apparent velocity, or in short by its slowness vector $\boldsymbol{s}_o$. Thus we can write:

$$w_n(t) = w(t - \mathbf{r}_n \cdot \mathbf{s}_0) .$$

Following Eq. (9.5) the best beam of an array with *M* sensors for a seismic signal for the slowness $\boldsymbol{s}_o$ is defined as

$$b(t) = \frac{1}{M} \sum_{j=1}^{M} w_j(t + \boldsymbol{r}_j \cdot \boldsymbol{s}_o) = w(t) . \qquad (9.14)$$

The seismic signal at sensor A_n of a plane wave for any other slowness $\boldsymbol{s}$ can be written as $w_n(t) = w(t - \boldsymbol{r}_n \cdot \boldsymbol{s})$ and the beam is given by

$$b(t) = \frac{1}{M}\sum_{j=1}^{M} w_j(t + \boldsymbol{r}_j \cdot \boldsymbol{s}). \tag{9.15}$$

If we calculate all time shifts for a signal with the (correct) slowness $\boldsymbol{s}_o$ (Eq. (9.14)) with respect to any other slowness $\boldsymbol{s}$ (Eq. (9.15)), we get the difference for the signal at site A_n $w(t + \boldsymbol{r}_n \cdot \boldsymbol{s}_o - \boldsymbol{r}_n \cdot \boldsymbol{s}) = w(t + \boldsymbol{r}_n \cdot (\boldsymbol{s}_o - \boldsymbol{s}))$. The calculated beam can be written as

$$b(t) = \frac{1}{M}\sum_{j=1}^{M} w_j(t + \boldsymbol{r}_j \cdot (\boldsymbol{s}_o - \boldsymbol{s})). \tag{9.16}$$

This beam is now a function of the difference between the two slowness values $(\boldsymbol{s}_o - \boldsymbol{s})$ and the geometry of the array $\boldsymbol{r}_j$. If the correct slowness is used, the beam calculated with Eq. (9.16) will be identical to the original signal *w(t)*. The seismic energy of this beam can be calculated by integrating over the squared amplitudes:

$$E(t) = \int_{-\infty}^{\infty} b^2(t)\,dt = \int_{-\infty}^{\infty} \left[\frac{1}{M}\sum_{j=1}^{M} w_j(t + \boldsymbol{r}_j \cdot (\boldsymbol{s}_o - \boldsymbol{s}))\right]^2 dt. \tag{9.17}$$

This equation can be written in the frequency domain by applying Parseval's theorem and then the shifting theorem:

$$E(\omega, \boldsymbol{s}_o - \boldsymbol{s}) = \frac{1}{2\pi}\int_{-\infty}^{\infty} \left|\overline{w}(\omega)\right|^2 \cdot \left|\frac{1}{M}\sum_{j=1}^{M} e^{i\omega \cdot \boldsymbol{r}_j \cdot (\boldsymbol{s}_O - \boldsymbol{s})}\right|^2 d\omega \tag{9.18}$$

with $\overline{w}(\omega)$ being the Fourier transform of the seismogram *w(t)*. Using the definition of the wavenumber vector $\boldsymbol{k} = \omega \cdot \boldsymbol{s}$, we can also write $\boldsymbol{k}_o = \omega \cdot \boldsymbol{s}_o$:

$$E(\omega, \boldsymbol{k}_o - \boldsymbol{k}) = \frac{1}{2\pi}\int_{-\infty}^{\infty} \left|\overline{w}(\omega)\right|^2 \cdot \left|C(\boldsymbol{k}_o - \boldsymbol{k})\right|^2 d\omega, \text{ where} \tag{9.19}$$

$$\left|C(\boldsymbol{k}_o - \boldsymbol{k})\right|^2 = \left|\frac{1}{M}\sum_{j=1}^{M} e^{i\omega \cdot \boldsymbol{r}_n \cdot (\boldsymbol{k}_O - \boldsymbol{k})}\right|^2. \tag{9.20}$$

Eq. (9.18) or Eq. (9.19) defines the energy of an array beam for a plane wave with the slowness $\boldsymbol{s}_o$ (or $\boldsymbol{k}_o$), but calculating the applied time shifts for a slowness $\boldsymbol{s}$ (or $\boldsymbol{k}$). If the difference between $\boldsymbol{s}_o$ and $\boldsymbol{s}$ (or $\boldsymbol{k}_o$ and $\boldsymbol{k}$) changes, the resulting beam has a different energy. However, this dependency is not a function of the actual signals observed at the single sites, but only a function of the array geometry weighted with the slowness difference $\boldsymbol{r}_n \cdot (\boldsymbol{k}_o - \boldsymbol{k})$ (Eq. (9.19)). If the slowness difference is zero, the factor $\left|C(\boldsymbol{k}_o - \boldsymbol{k})\right|^2$ becomes 1.0 and the array is optimally tuned for this slowness. All other energy propagating with a different slowness will be (partly) suppressed. Therefore, Eq. (9.20) is called the transfer function of an array. This function is not only dependent on the slowness of the seismic phase observed with the array, but also on the frequency, i.e., a function of the wavenumber *k* of the observed signal, and of the array geometry.

There exists literature about general criteria used to evaluate array transfer functions for a given array geometry (see e.g., Harjes and Henger, 1973; Johnson and Dudgeon 1993; 2002). Some general rules about transfer characteristics of arrays can be formulated as follows:

1) The aperture of an array defines the resolution of the array for small wavenumbers. The larger the aperture *a*, the smaller are the wavenumbers that can be measured with the array. The upper limit for the longest wavelength λ that can be resolved by array techniques is approximately similar to the aperture *a* of the array. The array behaves like a single station for signals with $\lambda \gg a$.

2) The number of sites controls the quality of the array as a wavenumber filter, i.e., its ability to suppress seismic energy crossing simultaneously with a different slowness the array than the one on which the array is steered. (see point 4).

3) The distances between the seismometers define the position of the side lobes of the array transfer function and the largest resolvable wavenumber: the smaller the mean distance, the smaller the wavelength of a resolvable seismic phase will be (for a given seismic velocity).

4) The geometry of the array defines the azimuth dependence of the aforementioned points.

Some of these points are demonstrated by two examples of array transfer functions. Fig. 9.22 shows the array transfer function of the cross-shaped Yellowknife array (YKA, see Fig. 9.1) and Fig. 9.23 shows the array transfer function of the circular, small aperture array ARCES.

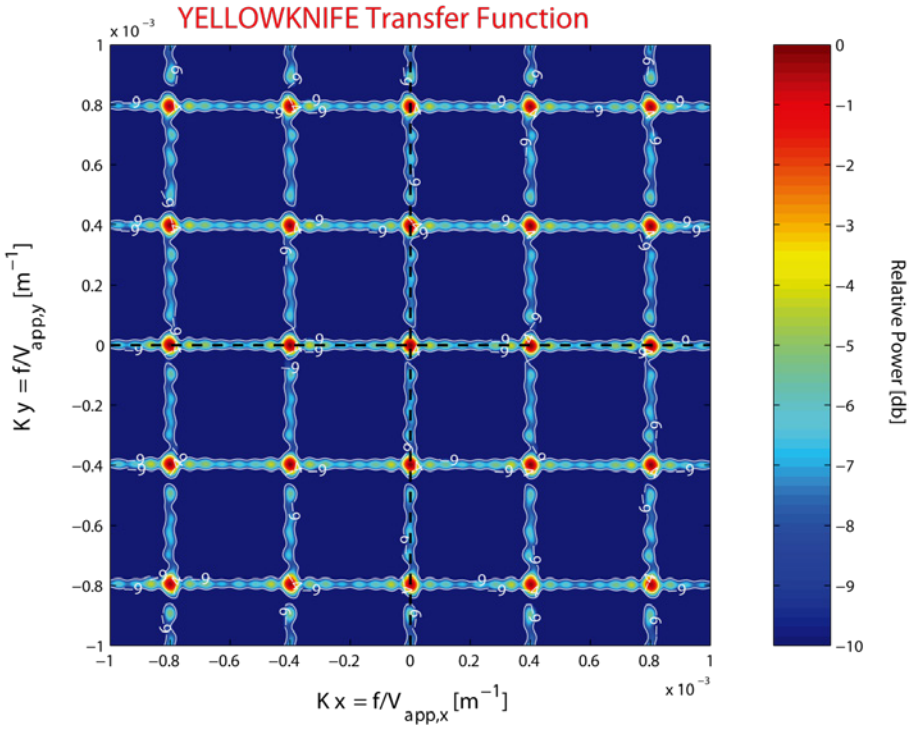

Fig. 9.22 This figure shows the array transfer function of the cross-shaped Yellowknife array (see Fig. 9.1) as relative power (color coded and with white isolines) of the array response normalized with its maximum.

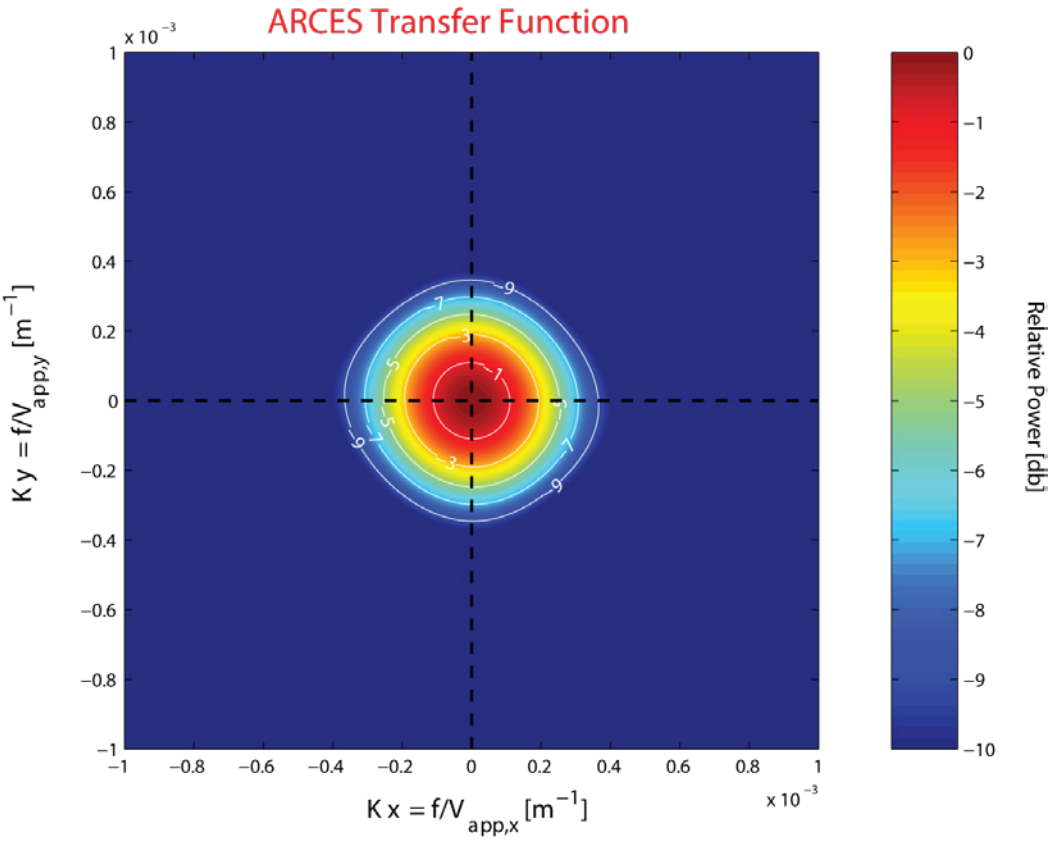

Fig. 9.23 This figure illustrates the array transfer function of the circular ARCES array (see Fig. 9.3). The figure shows relative power of the array response normalized with its maximum. White isolines were plotted at -1, -3, -5, -7, and -9 db below the maximum of the array response.

The ARCES geometry (see Fig. 9.3) gives a perfect azimuthal resolution, and the side lobes of the transfer function are far away from the main lobe. However, because of the small aperture, this array cannot distinguish between waves with small wavenumber differences, as can be seen in the relatively wide main lobe of the transfer function. In contrast, in the case of Yellowknife, the main lobe is very narrow because of the much larger aperture of the array. This results in a higher resolution in measuring apparent velocities. But the array shows resolution differences for different azimuths, which are caused by its geometry. The many side lobes of the transfer function are the effect of the larger distances between the single array sites.

Details on array design for the purpose of maximizing the gain achievable by beamforming can be found in Section 9.11.

9.8 Slowness estimation using seismic arrays

In the following sections we will introduce the “f-k analysis” and “beampacking” methods. Simply speaking, it is all a matter of forming beams with different slowness vectors and comparing the amplitudes or the power of the beams, and then finding out which v_{app} – backazimuth combination gives the highest energy on the beam, i.e., to find out which beam

is the "best" beam. In f-k analysis the process is done in the frequency domain rather than in the time domain. Both methods are nowadays the theoretical background for many different approaches not only in global and regional array seismology but also in local velocity structure and site effect investigations (see also Chapter 13, Section 13.4.4 and Chapter 14, Section 14.3.2.1).

9.8.1 Slowness estimation by f-k analysis

Frequency-wavenumber analysis – "f-k analysis" – is used as a reference tool in array processing for estimating slowness. A description of the method may be found, e.g., in Capon (1969a) or as a larger review in Capon (1973). This method has been further developed to include wide-band analysis, maximum-likelihood estimation techniques, and three-component data (Kværna and Doornbos, 1986; Kværna and Ringdal, 1986; Ødegaard et al., 1990). Theoretical aspects and information on the development of the methodology are also found in several textbooks on seismology and geophysics (Capon, 1973; Aki and Richards, 1980; Buttkus, 2000; Kennett, 2002), as well as in numerous original articles or review papers since the 1960s (e.g., Burg, 1964; Lacoss, 1965; Linville and Laster, 1966; Iyer, 1968; Liaw and McEvilly, 1979; Rost and Thomas, 2002).

The methodology exploits the deterministic, non-periodic character of seismic wave propagation to calculate the frequency-wavenumber spectrum of the signals by applying the multidimensional Fourier transform. Under these assumptions, a monochromatic, plane wave $w(x,t)$ will propagate along the x direction according to equation:

$$w(x,t) = Ae^{i2\pi(f_0 t - k_0 x)}, \tag{9.21}$$

where A is the amplitude, f_0 the frequency and k_0 the wavenumber in the x direction. Application of the two-dimensional Fourier transform provides:

$$W(k_x, f) = \int_{-\infty}^{\infty}\int_{-\infty}^{\infty} Ae^{-i2\pi[t(f-f_0)-x(k_x-k_0)]}dxdt . \tag{9.22}$$

Using the delta function properties, Eq. (9.22) can be rewritten as follows:

$$W(k_x, f) = A\delta(f - f_0)\delta(k_x - k_0) . \tag{9.23}$$

Eq. (9.23) suggests the possibility to map a plane, monochromatic wave in the frequency-wavenumber domain as a point, with coordinates $(f, k_x) = (f_0, k_0)$, which are nothing else than the frequency and wavenumber of the wave (e.g., Buttkus, 2000). Since the velocity of this wave is related to its wavenumber through the expression $v_0 = \frac{f_0}{k_0}$, it is easy to observe that the wave's velocity is the slope of the line connecting the point (f_0, k_0) in the frequency-wavenumber domain with the origin of the applied coordinate system f, k_x.

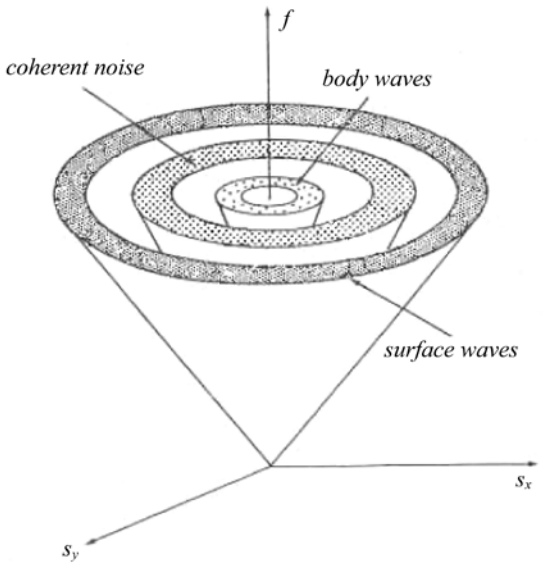

Fig. 9.24 Frequency-slowness distribution of different types of waves: surface waves, body waves and coherent noise (slight modification of Fig. 7.3 from Buttkus, 2000, p. 107).

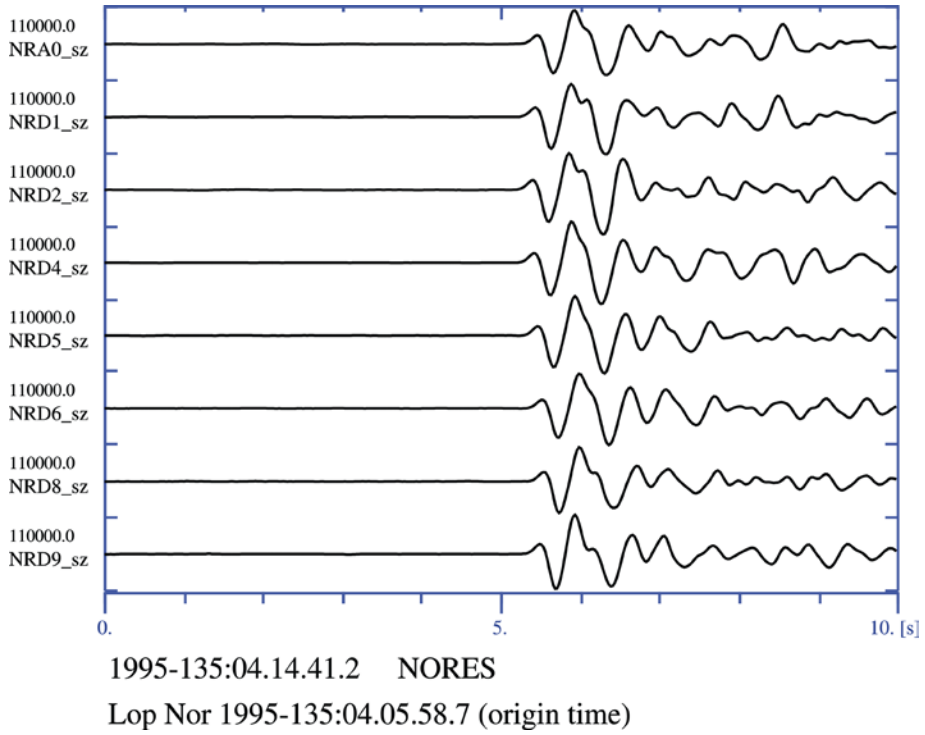

Fig. 9.25 NORES recordings (raw data) of the Lop Nor explosion on May 15, 1995. Traces from the center site A0 and the D-ring instruments are shown to the same scale. The time scale is in [s].

Transferring our observations onto the $k_x k_y$ plane, the angle between the k_y axis and the direction to the point (f_0, k_0) is the azimuth of the wave under discussion. Thus, measuring waves in two-dimensions, which we place on the Earth's surface, and assuming that k_x, k_y are

the wavenumber along the *x* and *y* direction respectively, provides us through f-k analysis with *f*, k_x, k_y and thereby the slowness distribution of the different types of signals. Adding frequency as a third dimension results in the formation of a 'cone', as in Fig. 9.24, where the different types of waves (i.e., body and surface waves, coherent noise) occupy specific concentric areas which in most cases do not overlap. In reality, the spectrum of seismic signals in its entirety exhibits a much larger complexity than the simplistic approach shown in Fig. 9.24. This is the result of a large number of factors affecting seismic signals, such as the geometry of near-surface crustal structure, the inhomogeneity of the crust, topography, etc., to mention only a few.

Practically, f-k analysis is performed in the frequency domain and represents in principle beamforming in the frequency domain for a number of different slowness values. A time shift in the time domain is equivalent to a phase shift in the frequency domain, since time is the analogue to angular frequency and space the analogue to wavenumber. Normally, at NORSAR we use slowness values between -0.4 and 0.4 s/km equally spaced over 51 by 51 points. For every one of these points the beam power is evaluated, giving an equally spaced grid of 2601 points with power information.

Such a power grid is displayed in Fig. 9.26 with the slowness ranging from -0.2 to 0.2 s/km; the unfiltered data are shown in Fig. 9.25. The power is displayed by isolines of dB down from the maximum power. The maximum power in the grid and the corresponding slowness vector define the slowness of the plane wave.

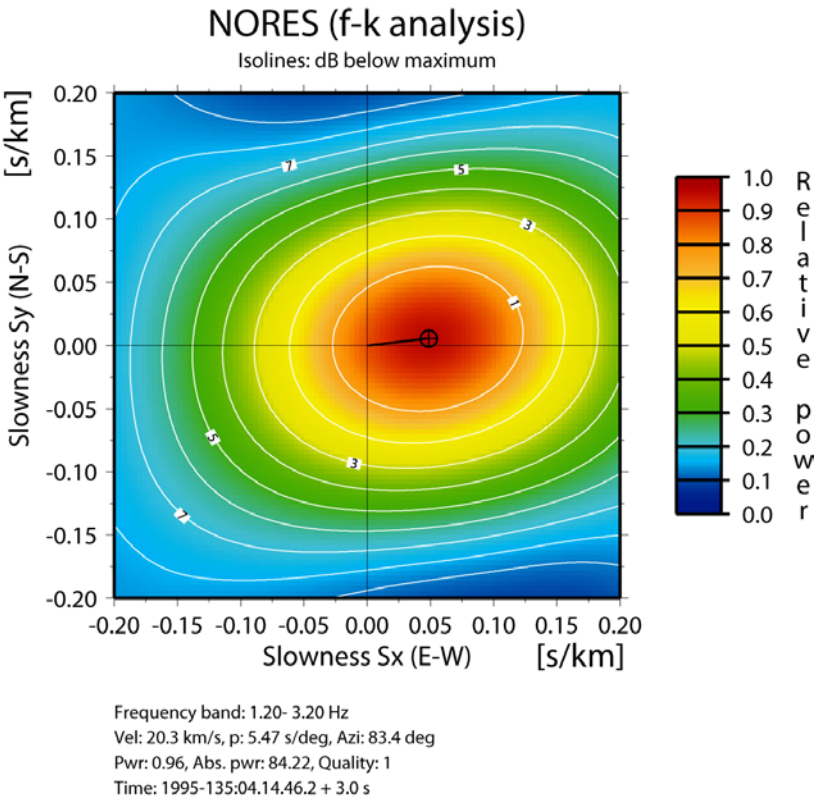

Fig. 9.26 Result from wide-band f-k analysis of NORES data from a 3 second window around the signal shown in Fig. 9.25. The isolines are in dB from the maximum peak and the color-coded relative power is a measure of signal coherency.

In the f-k plot in Fig. 9.26 color-coding is used to represent the relative power of the multichannel signal for 51 by 51 points in slowness space. Because the f-k analysis is a frequency-domain method, one has to define a frequency range of interest. In our case the data were analyzed in the frequency range between 1.2 and 3.2 Hz. The peak level is found at an apparent velocity of 20.3 km/s and a backazimuth of 83.4°. The normalized relative peak power is 0.96. This measure tells us how coherent the signal is between the different sites and that a beam formed with the corresponding slowness will give a signal power that is 0.96 times the average power of the individual sensors. This means that the estimated beam signal will have practically no signal loss for this slowness and in this filter band as compared to individual sensors. However, such beam loss can be taken into account when calculating station magnitudes by adding empirically derived corrections. The equivalent beam total power in Fig. 9.26 is 84.22 dB. The isolines tell us that using any different (i.e., wrong) slowness will give a signal loss of maximum 10 dB, which would correspond to an underestimation of magnitude by 0.5 magnitude units, if uncorrected.

The example in Fig. 9.26 is in a way a cross-section of the cone of Fig. 9.24 for the frequency interval 1.2 to 3.2 Hz, "focused" on the characteristics of the seismic phase selected for analysis. As already mentioned in Section 9.7, the shape of the horizontal slowness distribution is defined by the position of the elements of the recording array and the distances between them.

An uncertainty of the estimated apparent velocity and backazimuth can be derived from the size of the observed power maximum in the f-k plot at a given dB level below the maximum, the SNR of the signal, and the power difference between the maximum and any existing secondary maximum that may be present in the plot.

Fig. 9.27 displays the f-k analysis results for a 1.5 s long window of a signal arriving vertically at the array displayed at the bottom, for a narrow (left) and a wide (right) frequency range. The strong side-lobes appearing in the case when the technique is applied to a narrow frequency band (6.0 ± 0.1 Hz) are eliminated by the application over a wider range (1.9 – 10.0 Hz). Kværna and Doornbos (1986) reported on f-k analysis techniques using an integration over a wider frequency band (also called "wide-band" or "broadband" f-k analysis) rather than the single frequency-wavenumber analysis (e.g., Capon, 1969a; 1973) as applied by many authors. Fig. 9.27 demonstrates the increased stability of the wide-band f-k analysis (Kværna and Doornbos, 1986; Kværna and Ringdal, 1986) for data of adequately high SNR over the selected frequency range. The reason for this is that the positions of the side-lobes in the f-k space are frequency dependent. To the contrary, the main-lobe for different frequencies is always positioned at the same place. So, summing up f-k results for different frequencies increases the amplitude distance between the main and the side-lobes.

The result of an f-k analysis also depends on the method employed to determine the maximum power in the grid. There exists a variety of methods, such as the maximum likelihood method (Kelly and Levin, 1964; Levin, 1964; Capon et al., 1967), the maximum entropy method (Burg, 1967), the multiple signal classification (MUSIC) algorithm (Schmidt, 1986) and various adaptive algorithms for the estimation of spectral power density (e.g., Goldstein and Archuleta, 1991a; Goldstein and Chouet, 1994; Fujiwara, 1997).

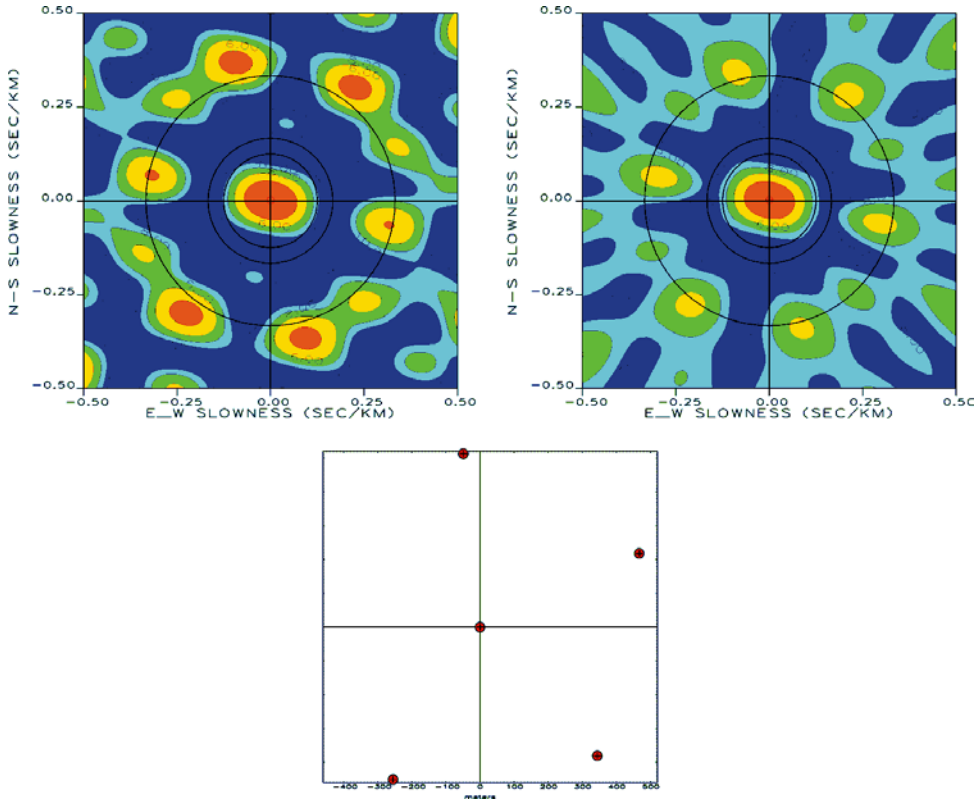

Fig. 9.27 Results from narrow- (upper left) and wide-band (upper right) f-k analysis of a 1.5 second window of a signal arriving vertically at the seismic array shown below. The narrow frequency band extends from 5.9 to 6.1 Hz, while wide-band f-k analysis was applied over the range 1.9 – 10.0 Hz. The isolines are in dB from the maximum peak and the color-coded relative power is a measure of signal coherency. The black circles represent apparent velocities of 8, 6 and 3 km/s, respectively.

9.8.2 Beampacking (time domain wavenumber analysis)

An alternative to the technique described above is the so-called beampacking scheme, which had been developed at NORSAR to apply f-k analysis of regional phases to data of the large NORSAR array (NOA). This algorithm performs in the time domain beamforming over a predefined grid of slowness points and measures the power of the beam.

As an example see Fig. 9.28, where we used the same NORES data as for the f-k analysis in Fig. 9.26. All data were prefiltered with a Butterworth 1.2 – 3.2 Hz bandpass filter to make the results comparable with the f-k result in Fig. 9.26. To obtain a similar resolution as for the f-k analysis, the time domain wavenumber analysis requires a relatively high sample rate of the data. Therefore, we oversampled the data in this example 5 times by interpolation, i.e., we changed the sample rate from 40 to 200 Hz.

One can see from the beampacking process that we get practically the same slowness estimate as for the f-k analysis in the frequency domain (Fig. 9.26). In the time domain case, the relative power is the signal power of the beam for the peak slowness divided by the average sensor power in the same time window. The total power of 91.45 dB in Fig. 9.28 is the maximum beam power.

Compared to the f-k process used, the resulting total power is now 6 dB higher, which is due to the measurement method, and not a real gain. However, the beampacking process results in a slightly (about 10%) narrower peak for the maximum power as compared with f-k analysis.

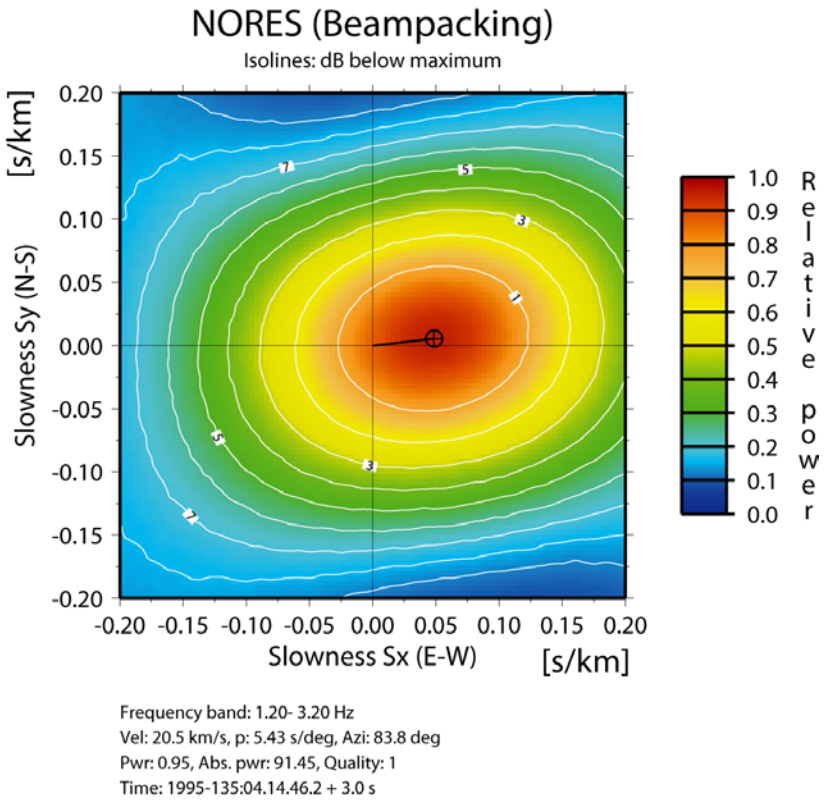

Fig. 9.28 Result from beampacking of the NORES data in Fig. 9.27 in an equispaced slowness grid. The data were prefiltered in the band 1.2 – 3.2 Hz and were resampled to 200 Hz. The isolines represent power of each beam within the 3-second window analyzed.

9.8.3 Plane wave fitting – slowness estimation by time picks

Yet another way of estimating slowness is to pick carefully times of the first onset or any other common distinguishable part of the same phase (same cycle) for all instruments in an array (see Fig. 9.29). Estimating the ray parameter and BAZ of a teleseismic P onset by fitting an assumed plane wave to a set of onset times was first applied by Abt (1907). Today, we may, e.g., use Eq. (9.24) to estimate the slowness vector $\boldsymbol{s}$ by a least squares fit to the observations.

Let t_i be the arrival time picked at site i, and t_{ref} be the arrival time at the reference site, then $\tau_i = t_i - t_{ref}$ is the observed time delay at site i. We observe the plane wave at M sites. With $M \geq 3$, we can estimate the horizontal components (s_x, s_y) of the slowness vector $\boldsymbol{s}$ by using e.g., a least squares fitting algorithm. If $M \geq 4$, the vertical component of the slowness vector (s_z) can also be resolved. The uncertainties of the estimated parameters can be calculated simultaneously by solving the equation system of Eq. (9.24).

$$\sum_{i=1}^{M} (\tau_i - \boldsymbol{r}_i \cdot \boldsymbol{s})^2 = min \quad . \tag{9.24}$$

This method requires interactive analyst work. However, to obtain automatic time picks and thereby provide a slowness estimate automatically, techniques like cross-correlation (matched filtering) or just picking of peak amplitude within a time window (for phases that have an impulsive onset and last two or three cycles) may be used (see e.g., Del Pezzo and Giudicepietro, 2002).

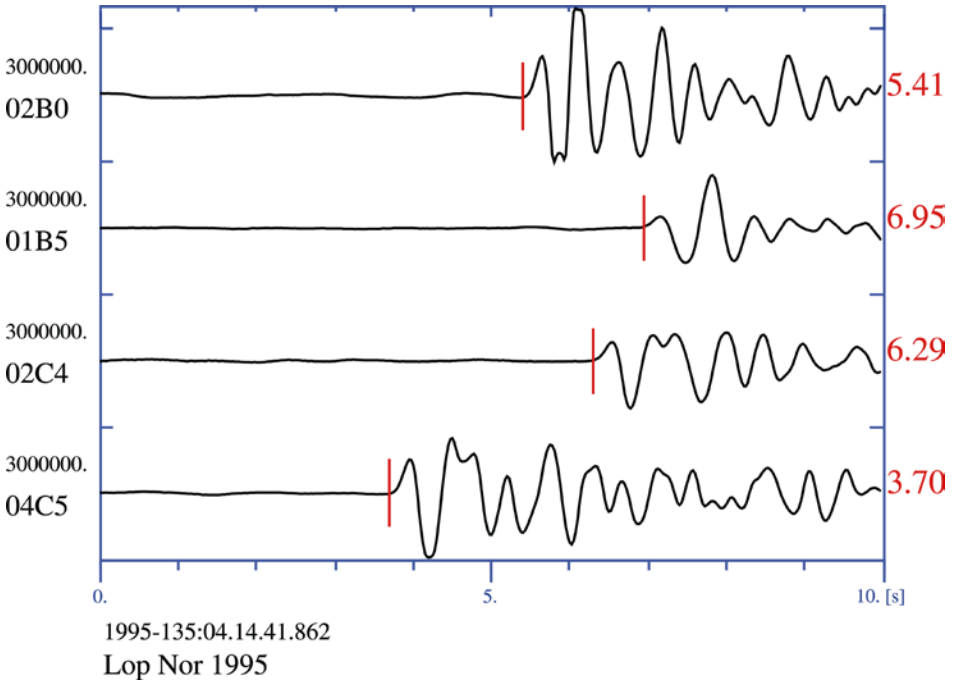

Fig. 9.29 NOA recording of the Lop Nor explosion of May 15, 1995. Vertical traces (sz) from the sites 02B0, 01B5, 02C4, and 04C5 of the NOA array (see also Fig. 9.2) are shown at the same amplitude scale. Note the large time delays as compared to the smaller NORES array in Fig. 9.27. The figure illustrates a simple time pick procedure of the individual onsets. A plane wave fit to these 4 onset-time measurements gives a backazimuth of 77.5° (theoretically expected 76.1°) and an apparent velocity of 16.3 km/s, which is close to the theoretical value of 14.5 km/s corresponding to an epicentral distance of 61°.

The so-called Progressive Multichannel Cross Correlation (P.M.C.C) program package can apply inter-sensor correlation functions between single array traces to estimate BAZ and slowness of seismic signals in a continuous mode (see Cansi et al., 1993; Cansi, 1995). However, because of the amount of required computations, this method is most effective for arrays with a smaller number of sites or for subarray configurations.

9.8.4 The VESPA algorithm

A method to separate signals propagating with different apparent velocities is the VElocity SPectrum Analysis (VESPA). The principal idea of this method is to estimate the seismic energy reaching an array with different slownesses and to plot the beam energy along the time

axis. The usual way to display a vespagram is to calculate the observed energy for specific beams and to construct an isoline plot of the observed energy for the different slowness values. The original VESPA process was defined for plotting the observed energy from a specific azimuth for different apparent velocities versus time (Davies et al., 1971).

Fig. 9.30 shows as an example of a vespagram for a mine blast in the Khibiny Massif (Kola Peninsula) observed with the ARCES array. The underground blasting of about 190 tons of explosives occurred on December 21, 1992 at 07:10 (latitude 67.67°, longitude 33.73°) at about 3.55° epicentral distance from ARCES. All beams were calculated with the theoretical backazimuth of 118°, and the seismograms were bandpass filtered between 2 and 8 Hz. Fig 9.30 (middle) shows two of the filtered seismograms used to calculate the vespagram.

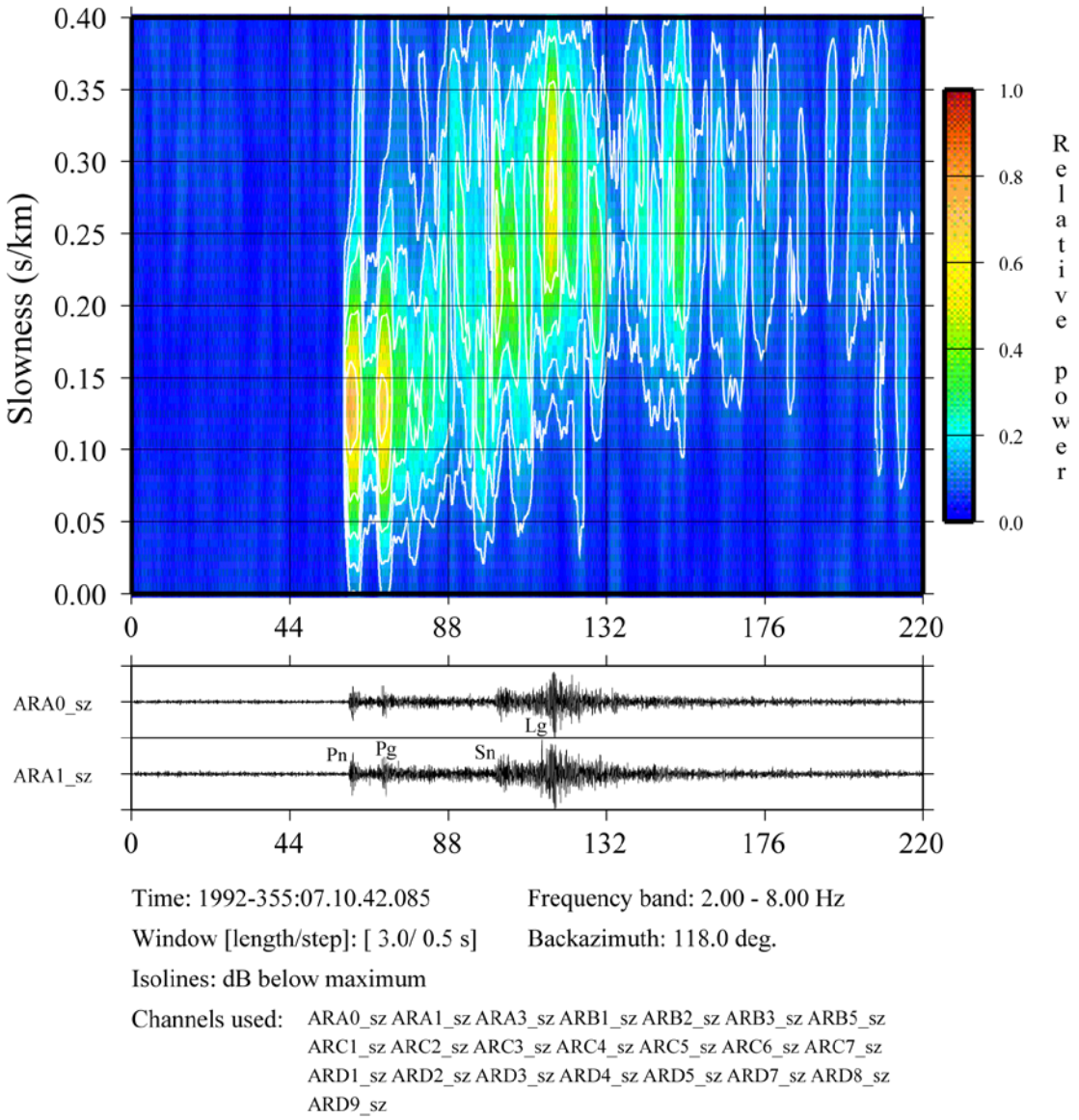

Fig. 9.30 Vespagram for a mining explosion (December 21, 1992; 07:10 h; latitude 67.67° N, longitude 33.73° E) in the Khibiny Massif observed at ARCES. Shown is the observed seismic energy for different apparent velocities (slownesses) and a constant backazimuth of 118°.

The energy for the different slowness values was calculated for 3 second-long sliding windows moved forward in 0.5 s long steps. The observed energy was normalized with the maximum value and the isolines were plotted as contour lines in [dB] below this maximum. Note that the first two P onsets both have a slowness of about 0.125 s/km equivalent to an apparent velocity of 8 km/s; these are the Pn phase and a superposition of onsets from several crustal phases. The S phases are clearly separated from the P phases in the slowness space; Sn with a slowness of about 0.225 s/km (corresponding to an apparent velocity of about 4.44 km/s) and the dominating Lg phase with a slowness of about 0.28 s/km or an apparent velocity of about 3.57 km/s.

Later, the vespagram concept was expanded by plotting the observed energy from different azimuths using a specific apparent velocity. Fig. 9.31 shows an example for such a plot for the same event in the Khibiny Massif as for Fig. 9.30.

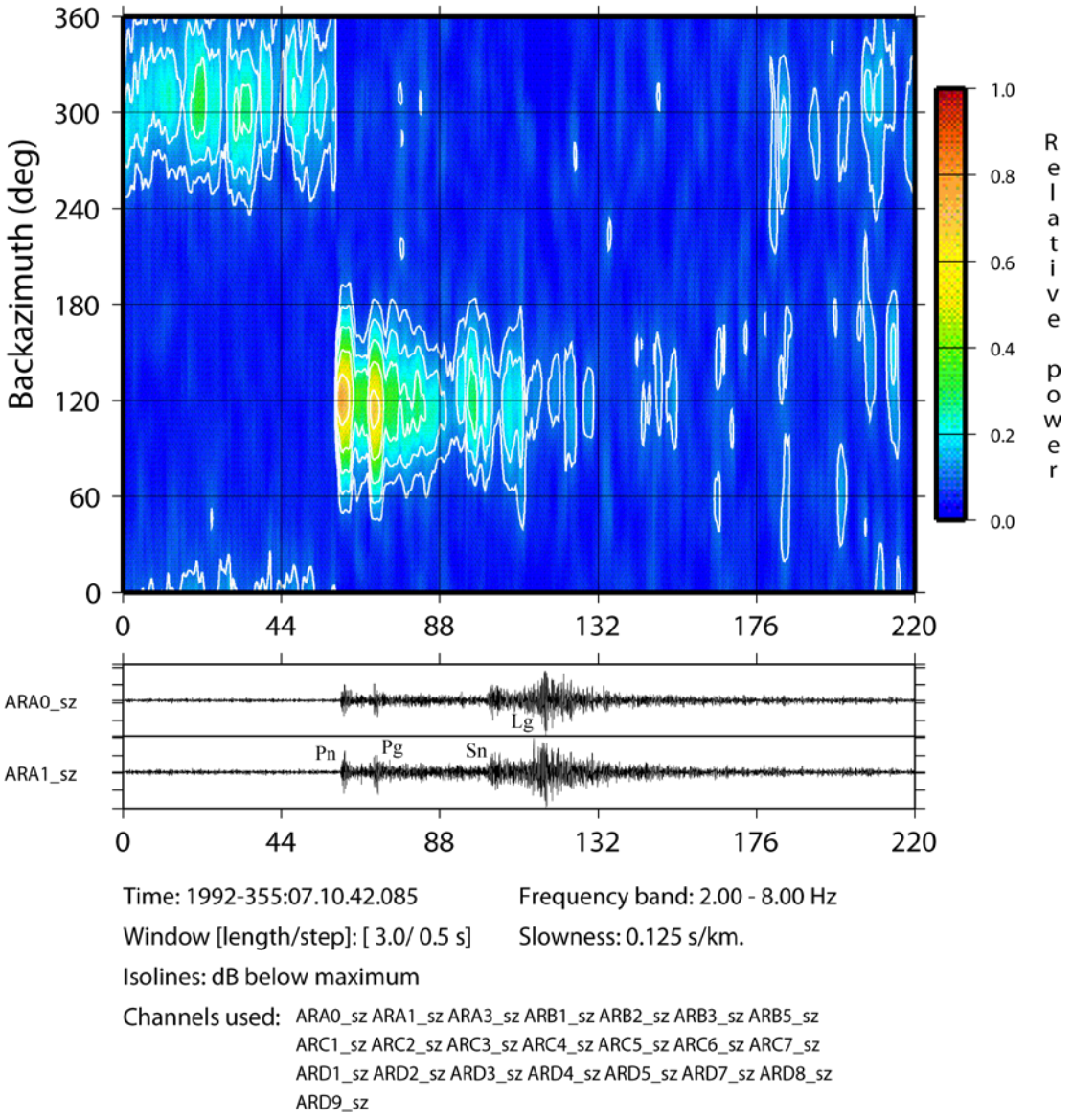

Fig. 9.31 As Fig. 9.30 but the energy is now calculated for a constant apparent velocity of 8 km/s (i.e., a slowness of 0.125 s/km) and different backazimuths.

Instead of a constant backazimuth, a constant apparent velocity of 8 km/s was used to calculate the beam energy from all azimuth directions. Note also that the noise preceding the first P onset contains energy with apparent velocities around 8 km/s, but this noise approaches the array from a different backazimuth (310°), and the crustal P phases show a slight shift in the backazimuth direction relative to the first mantle P phase (Pn).

9.8.5 The correlation method used at the UKAEA arrays

As discussed in Section 9.7, the array transfer function of the UKAEA array YKA shows strong side lobes along a rectangular grid (see Fig. 9.21). This effect can be observed at all orthogonal linear or L-shaped arrays (Birtill and Whiteway, 1965). To improve the lower resolution along these principal axes, a correlation method has been introduced. In a first step, theoretical beams are calculated separately for each of the two seismometer lines; the geometrical crossing point of the two linear subarrays is used as the common reference point for both beams. If the actual signal has the same slowness as the slowness used to calculate the two beams, the signal must be in phase on both beams. In a second step, the calculation of the cross-correlation between the two beams tests this condition. The correlator trace is calculated for a short, moving time window. This non-linear process is very sensitive to small phase differences and improves the resolution of such arrays especially along the principal axes of their transfer functions (for further details see Whiteway, 1965; Birtill and Whiteway, 1965; Weichert et al., 1967).

9.8.6 Tracking earthquake source propagation with seismic arrays

Usually earthquakes are modeled as point sources. The hypocenter of an earthquake is defined as the point where the initial rupture starts (see IS 11.1). However, for many studies the geometry of the rupture and its dynamics are of importance. Spudich and Cranswick (1984) published a study, in which they used data from a small linear accelerometer array to investigate the dynamics of the 1979 Imperial Valley, California earthquake. Similar studies were made by Goldstein and Archuleta (1991b) and Huang (2001), who used data from two very small aperture accelerometer arrays in Taiwan (SMART-1 (Abrahamson et al., 1987) and SMART-2 (Chiu et al., 1994)) to investigate rupture propagation of large Taiwan earthquakes. Common for these studies is that they all applied array analysis techniques to strong motion data from nearby strong earthquakes.

After the huge 2004 Sumatra earthquake, a slightly different approach was tested and implemented. The fault length of this event was more than 1000 km long and using data from the German network of broadband stations or the Japanese Hi-Net array, the rupture propagation of this earthquake could be monitored at teleseismic distances by applying array techniques (Krüger and Ohrnberger, 2005a and b; Ishii et al., 2005a and b). These authors measured BAZ and slowness in a moving window for times after the direct first P onset. Usually, one can observe the different seismic phases (see e.g., the VESPA algorithm in Section 9.8.4) arriving at the array. In the case of very large arrays, however, the seismograms during these time windows are dominated by the seismic energy radiated during the ongoing source process itself. The authors could show that the observed systematic change of BAZ and slowness can only be explained by the continuous seismic energy radiating rupture along the seismic fault. Later, several authors applied this technique to investigate rupture dynamics

of large earthquakes and today even an automated version for continuous monitoring of megathrust zones has been tested (Roessler et al., 2010).

9.8.7 Slowness corrections

When observing the backazimuth of an approaching wave, we find deviations from the expected backazimuth. In addition, the observed ray parameter will also be different from the theoretical one. This observation is valid for any seismic station. If the deviation is systematic and consistent for a given source location (or small region), we can correct for this deviation. If the predicted slowness is $\boldsymbol{s}_c$ and the observed slowness is $\boldsymbol{s}_o$ (Fig. 9.32), then the slowness deviation is

$$\Delta \boldsymbol{s} = \boldsymbol{s}_o - \boldsymbol{s}_c \,. \tag{9.25}$$

It is also common to use the ray parameter p [s/°] and the backazimuth BAZ [°] as slowness vector components and to express the residuals as:

$$\Delta p = p_o - p_c \;\text{ and }\; \Delta BAZ = BAZ_o - BAZ_c \,. \tag{9.26}$$

However, every array has to be calibrated with its own corrections. Numerous studies have been performed to obtain slowness corrections for different seismic arrays (see e.g., Berteussen, 1976; Krüger and Weber, 1992; Bondár et al., 1999; Kuleli et al., 2001; Schweitzer, 2001; and more recent examples of such studies are, e.g., Hao and Zheng, 2009; Tibuleac and Stroujkova, 2009; or Shen and Ritter, 2010). Usually, the derivation of slowness corrections for the whole slowness range observable with one array needs a large amount of corresponding reference data and therefore takes some time.

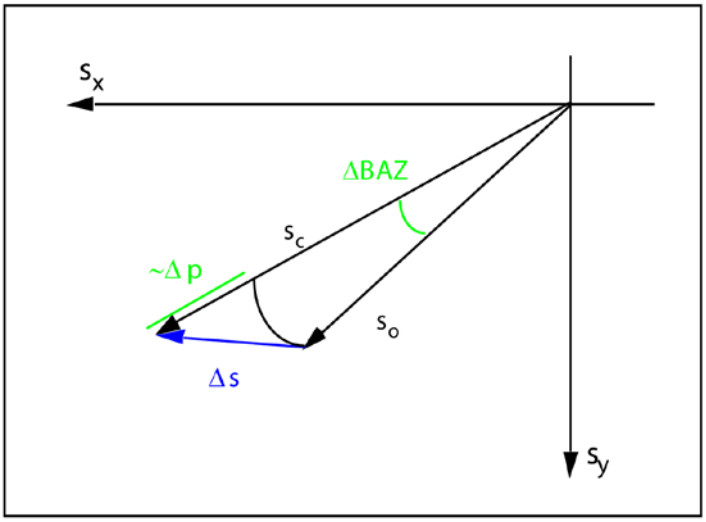

Fig. 9.32 Slowness vector deviation in the horizontal plane. The vector $\boldsymbol{s}_c$ denotes the theoretical slowness. The vector $\boldsymbol{s}_o$ denotes the observed slowness. The vector $\Delta \boldsymbol{s}$ denotes the slowness residual, also referred to as the mislocation vector. The length of the slowness vector measured in [s/°] is the ray parameter p, and the angle between North and the slowness vector, measured clockwise, is the backazimuth BAZ.

9.9 Detection of repeating seismic events using waveform cross-correlation

In the same way that signals generated by a seismic event will resemble each other on two sensors with a sufficiently small separation, signals generated by two different seismic events will show similarity on a given sensor provided that the spatial separation of the event source locations is sufficiently small and that the event mechanisms are similar (see e.g., Geller and Mueller, 1980). This is to say that the signal observed at any seismic station is like a fingerprint for events within a given limited geographical region, as long as the seismic wave radiation pattern does not change. The degree of similarity between two segments of waveform can be measured by calculating their cross-correlation coefficient (CC). Given a signal template from a previously observed event, subsequent occurrences of that signal can be detected by calculating a continuous cross-correlation trace on the incoming data stream at the same site.

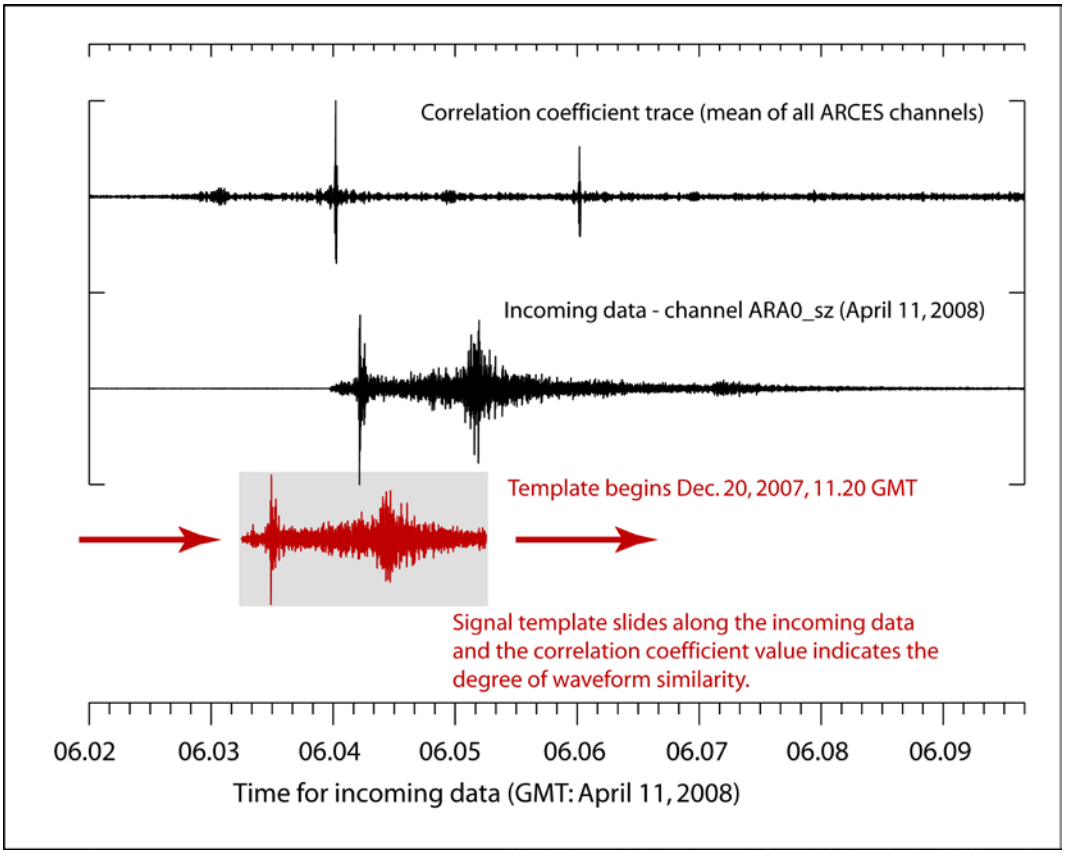

Fig. 9.33 Illustration of detection by waveform correlation on the ARCES array of an earthquake in April 2008 using a template from an event in 2007 as a master signal (from Bungum et al., 2010). All waveforms were bandpass filtered between 2 and 8 Hz prior to performing the cross-correlation.

The principle is illustrated in Fig. 9.33. A signal template is extracted on the ARCES array for a shallow earthquake in the Steigen region of northern Norway at an epicentral distance of approximately 460 km. This template is correlated with successive segments of data and the occurrences of new earthquakes close to the site of the master event are detected by identifying times, at which the correlation coefficient is sufficiently greater than the

background level. A second peak is observed in the correlation coefficient trace approximately two minutes after the first. This indicates the presence of an aftershock whose signal is buried in the coda of the first event. This processing is done for all available array traces. If a seismic signal is present, all correlation coefficient traces should have a maximum at the same time and one can stack the correlation coefficient traces without any time delay application. The SNR on the summed correlation coefficient trace will be increased and even tiny signals hidden in the noise or other signals can be detected.

Gibbons and Ringdal (2006) describe a number of applications of the method and point out that, especially on small-aperture arrays, false alarms can occur due to a coincidental waveform similarity over a short time window. Such false detections can frequently be identified by examining the alignment of the correlation coefficient traces on the single sensors. In the case of small-aperture arrays, Gibbons and Ringdal (2006) demonstrate that the correlation traces emulate a wavefront that propagates over the array with an apparent slowness vector which is approximately equal to the difference between the dominant slowness vectors of the master and detected events. If performing wide-band f-k analysis on the cross-correlation (CC) traces indicates a non-zero slowness vector then the detected signal cannot arrive from the same direction as the master event signal and the detection can be classified automatically as a false alarm and ignored. Fig. 9.34 displays the alignment of single channel CC-traces at ARCES for the Steigen event in Fig. 9.33 together with the slowness grid from the f-k analysis.

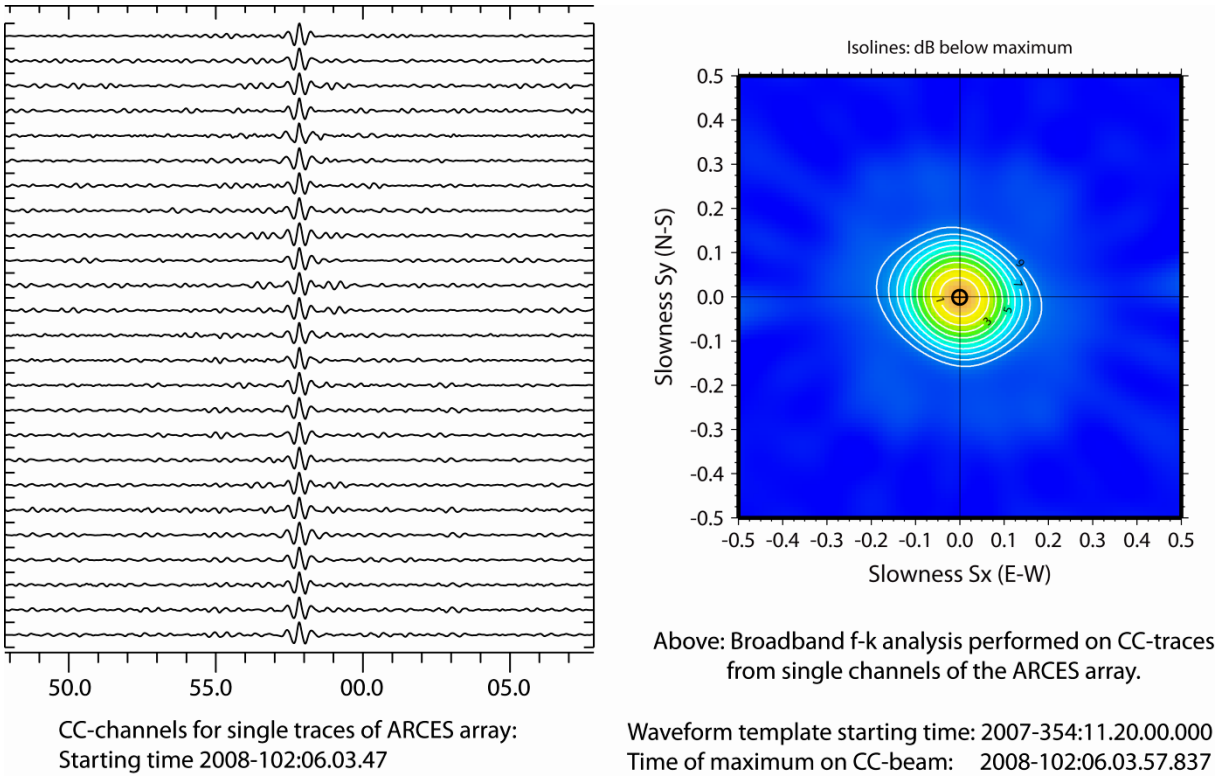

Fig. 9.34 Verification of the validity of a cross-correlation detection by performing f-k analysis on the individual correlation coefficient traces. A non-zero slowness vector would indicate that the signals from the master and detected events do not come from the same direction.

9.10 Ambient noise array analysis

9.10.1. Overview

During the last decades, ambient seismic vibration measurements have gained in importance, especially in regions covered with soft sediments (e.g., Aki, 1957; Horike, 1985; Tokimatsu, 1997; Okada, 2003; Foti et al., 2011). Advantages of the method are its low cost as well as the non-destructivity of measurements and thus its applicability even in densely populated areas. Whereas the presence of strong seismic noise is obstructive for active seismic investigations, it constitutes a continuous energy source for ambient seismic vibration measurements illuminating the subsurface.

One widespread application of ambient vibration measurements are microzonation studies (single station measurements analyzed with the H/V method, see e.g., Tokimatsu, 1997). Later on, the H/V method emerged as a geophysical tool to assess soil and sedimentary thickness, the analyzed depth ranging from tens of meters to more than 1000 m (e.g., Ibs von Seht and Wohlenberger, 1999; Delgado et al., 2000; Parolai et al., 2001). The H/V spectrum has even been employed to gain shear wave velocity profiles (Fäh et al., 2003; Parolai et al., 2002; Arai and Tokimatsu, 2004), but usually, ambient vibration array measurements are used to estimate the shear wave velocity structure (e.g., Asten and Henstridge, 1984; Horike, 1985; Tokimatsu, 1997; Scherbaum et al., 2003). However, the trade-off between accumulated travel times in the sediment structure and depth of the main impedance contrasts led to the development of combined inversion strategies from both techniques (Scherbaum et al., 2003; Parolai et al., 2005; Picozzi et al., 2005). A set of useful guidelines for single station and array measurements of ambient seismic vibrations was developed within the framework of the EU-project SESAME (Site Effects uSing AMbient Excitations, see e.g., SESAME group, 2004; Jongmans et al., 2005). For more details about the investigation of site response in urban areas by using earthquake data or seismic noise see Chapter 14.

A detailed review of sources of ambient vibrations can be found in Section 4.3 in Chapter 4. A discussion of noise which is specifically related to ambient vibration analysis is given in Bonnefoy-Claudet et al. (2004). At low frequencies (below 1 Hz), ambient vibrations seem to mainly consist of fundamental Rayleigh waves mostly caused by meteorological phenomena. However, at higher frequencies the noise sources are mostly caused by human activities and there is no agreement yet between authors on the ratio between body and surface waves as well as the ratio between Love and Rayleigh waves and fundamental and higher modes.

9.10.2 Single station/array measurements

Single station H/V analysis techniques (also known as Nakamura's technique, see Nogoshi and Igarashi, 1971; Nakamura, 1989; Bard, 1999) analyze ambient vibrations measured on horizontal and vertical seismometer components to estimate the fundamental resonance period of high impedance sediment layers overlaid by lower impedance materials (e.g., sediment over bedrock). The fundamental period is derived from the observation of a peak in the H/V spectral ratio, although the physical explanation of this peak is still under discussion, since both reverberating SH body waves as well as the ellipticity characteristics of Rayleigh surface waves may account for its existence. However, it has been demonstrated that both hypotheses explain the observations equally well in case of large impedance contrasts and simple stratigraphy (Malischewsky and Scherbaum, 2004).

Ambient vibration array techniques are logistically more demanding, but allow for the direct estimation of wave propagation characteristics, i.e., apparent wave velocity and direction of the seismic wave front. Frequency-wavenumber (f-k) and autocorrelation techniques are used to obtain the apparent phase velocity within narrow frequency bands. The resulting frequency-dependent phase velocity curves are interpreted as dispersion curve branches of surface waves and are inverted for the physical properties of 1-D Earth models parameterized as stack of horizontally homogeneous layers. Since the dispersion curve inversion constitutes a highly non-linear and non-unique problem, it is of utmost importance to obtain an accurate dispersion curve measurement and a well-founded interpretation of observations. Considering the resolution capabilities of array settings with a low number of sensors, adaptive measurement strategies have to be used to capture the full available wavelength range of the surface waves included in the ambient vibration wavefield (Bonnefoy-Claudet et al., 2005). Starting with small inter-station distance and small aperture provides a good estimate of the shallow shear wave velocity which can be used to optimize the array configuration for redeployment with larger apertures and inter-station distances. Thus, the array configuration is iteratively adapted to the next larger target wavelength. A proposed work flow can be found, e.g., in Jongmans et al. (2005). Further, a priori information (e.g., shallow shear wave velocities derived from hammer blow refraction seismic, borehole stratigraphies) may help to reduce the non-uniqueness of the inverse problem.

9.10.3 Array geometry for ambient vibration measurements

The optimal array geometry for ambient vibration measurements has been discussed by e.g., Asten and Henstridge (1984) and Kind (2002). Whereas small aperture arrays designed for monitoring natural or man-made seismic sources are optimized for (usually undispersed) broadband transient signal arrivals from relatively distant sources (see also Section 9.7), arrays used for ambient vibration measurements are supposed to record a mostly random wavefield caused by nearby superficial sources, which is analyzed within narrow frequency bands (Jongmans et al., 2005). The resolution of narrowband array responses is significantly reduced compared to wide-band array responses and aliasing peaks are fully developed due to the lack of superpositioning of beam patterns for different frequencies (Jongmans et al., 2005; see also Fig. 9.24). The resolution can be enhanced by using either a large number of sensors or choosing the array size according to the specific narrow wavelength range of interest, which means re-deployment of several array configurations for different frequency ranges as mentioned in Section 9.10.2. For ambient vibration measurements, Jongmans et al. (2005) recommend a circular array deployment with an odd number of stations (see also Section 9.12) since this configuration is known to have the best possible azimuthal suppression capability for a given number of sensors and allows for analysis using f-k as well as autocorrelation methods.

9.10.4 Estimation of phase velocity curves

The ability to extract phase velocity curves from ambient vibration measurements within specific frequency bands is inherently coupled with the propagation characteristics at the site and the nature of ambient vibration sources on the one hand, and with experimental conditions and data analysis procedures on the other hand (Jongmans et al., 2005). In principle, either Rayleigh or Love wave phase velocity curves can be produced, but often, only Rayleigh-wave

dispersion curves are analyzed (see, e.g., Okada, 2003, for a general discussion about three-component ambient vibration analysis).

Data processing methods can be classified in two basic types: f-k methods and autocorrelation methods. The first class of methods comprises the conventional semblance based frequency-wavenumber method (CVFK) after Kværna and Ringdal (1986; see also Section 9.8), which is implemented using sliding time windows and narrow frequency bands around a center frequency (see, e.g., Dietrich et al., 2001). Capon (1969a) formulated a high-resolution f-k approach, which optimizes the windowing function based on the evaluation of the cross spectral matrix (CSM matrix) such that the wavenumber response approaches a delta-function in the f-k domain. However, the gain in slowness resolution is traded against a lack of time resolution caused by the estimation of the cross spectral matrix ("block averaging") and its inversion. Since the construction of the windowing function involves the signal itself, the response cannot be independently studied from the signal. Only a lower limit of slowness resolution can be derived from the beam pattern (Kind, 2002). Another f-k analysis method is the MUSIC algorithm (Multiple Signal Classification, Schmidt, 1986; Schmidt and Franks, 1986) decomposing the CSM matrix into signal and noise subspaces.

For an overview on the extraction process of dispersion curves from ambient vibration data, see Fig. 9.35. In order to extract the most coherent plane wave arrival, a grid search is performed in the wavenumber plane. For every frequency band of interest and every time window, a slowness map is computed. For each slowness map, the maximum is extracted resulting in the propagation parameters (azimuth and slowness as a function of frequency). These propagation parameters along with the beampower value are analyzed as histograms for their distributional characteristics, and the mean curve and variance are estimated. Such a dispersion curve is computed for each sub-array. Dispersion curves are subsequently combined within the resolution limits of the respective arrays (for a more detailed description, see, e.g., Bonnefoy-Claudet et al., 2005).

Aki (1957) developed a spatial autocorrelation method (SPAC). The spatial autocorrelation function describes the similarity between seismograms recorded by station pairs with similar interstation distance. By filtering with a narrow passband before correlation, the frequency-dependence of the spatial autocorrelation function can be investigated. Assuming a stochastic wavefield that is stationary in time and space, the spatial autocorrelation function depends directly on the phase velocity (Aki, 1957). By azimuthal averaging of the spatial autocorrelation function (averaging for station pairs having equal inter-station distances, but different azimuths), the directionally independent autocorrelation coefficients can be expressed by using Bessel functions. In the same manner as for the f-k method, the analysis is performed with sliding time windows. For each time window, the spatially averaged autocorrelation curve is computed and subsequently, the mean curve and variance are calculated over all time windows. The autocorrelation curve can either be inverted directly for the shear-wave velocity profile or transformed into a dispersion curve first. Since several station pairs with equal inter-station distance are required for azimuthal averaging, the array configuration has to be circular (Aki, 1957) or at least regular (extended spatial autocorrelation (ESPAC), see Ohori et al., 2002). Bettig et al. (2001) modified the SPAC method (MSPAC) for application to less ideal array configurations by grouping the seismic co-array (Haubrich, 1968) into rings of finite thickness introducing a radial integration corresponding to an average over all autocorrelation coefficients within a particular ring in addition to the azimuthal integration.

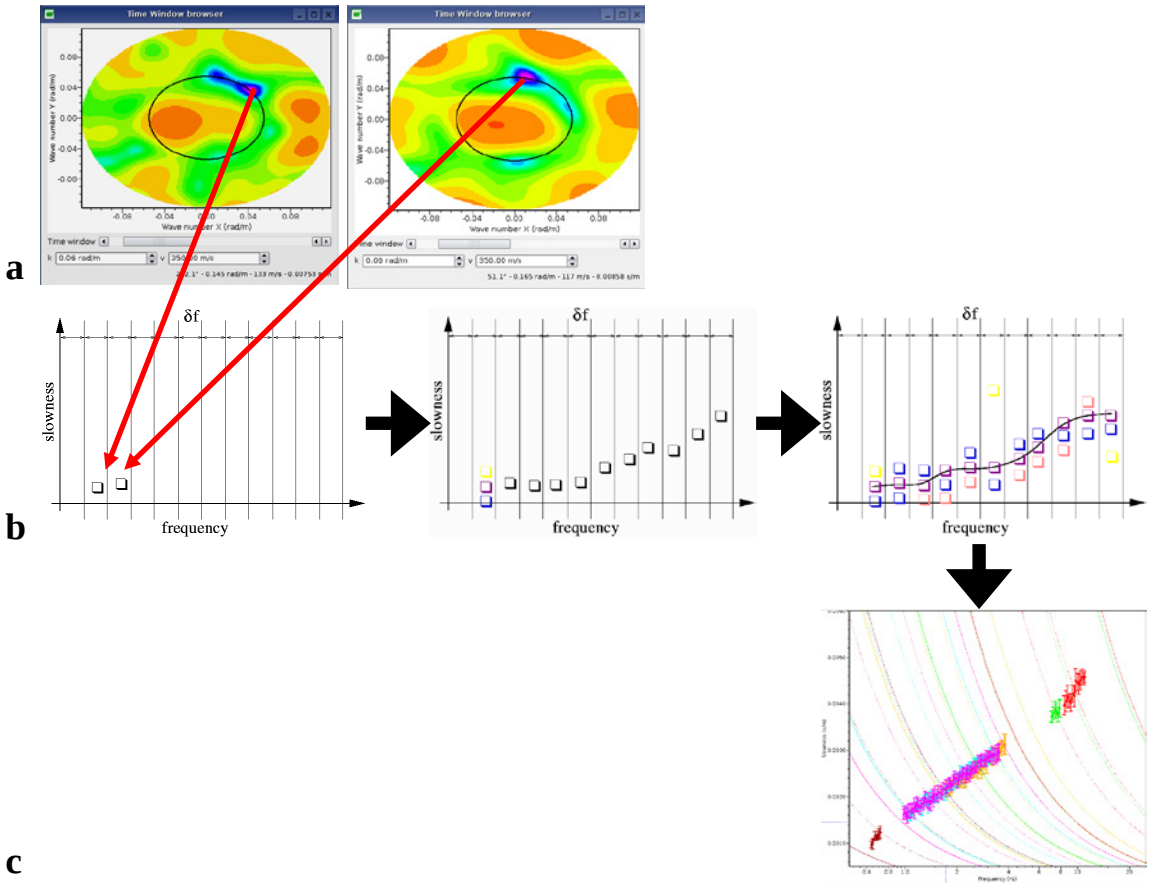

Fig. 9.35 How to extract dispersion curves using f-k methods: a) compute slowness map for every frequency band of interest and every time window, pick maximum; b) insert slowness values into frequency-slowness plot, one slowness value is extracted for every frequency band and every time window, and a mean curve including variance is computed; c) a dispersion curve is extracted for every sub-array, these are combined within their respective resolution limits (given by colored lines) to give the final dispersion curve (figures partly produced using geopsy/dinver software; Wathelet et al., 2004; Wathelet, 2008).

9.10.5 Inversion of dispersion curves to obtain shear wave velocity profiles

A software package readily available to deal with the determination of dispersion curves from ambient vibration array recordings and their inversion is the *geopsy/dinver* software (Wathelet et al., 2004; Wathelet, 2008; see Fig. 9.36 for an example). The *geopsy* software package implements f-k methods (CVFK and a so-called high resolution f-k algorithm (HRFK)) as well as autocorrelation methods (MSPAC) following the implementation in the CAP software developed within the framework of the SESAME project. Within the *dinver* software, the inversion of dispersion curves is performed using a neighbourhood algorithm (Sambridge 1999a and b) linked to a revised version of the forward computation by Herrmann (1987).

9.10.6 Difficulties

So far, only little work has been done on the reliability of the dispersion curve estimate and the dispersion curve inversion (for results of an international blind test see Cornou et al.,

2006). In general, dispersion curves derived from ambient vibration array analysis are reproducible and remain temporally stable although the sources exciting the wavefield may change. This stability is a consequence of the randomness of the source distribution and the attenuation properties of the medium (Bonnefoy-Claudet et al., 2005). However, the main assumptions on which the data inversion is based, namely that the subsurface is one-dimensional, i.e., horizontally stratified, and that ambient vibrations consist mainly of surface waves may not be a reasonable approximation under the given conditions (Jongmans et al., 2005).

One of the main difficulties in the analysis of ambient vibrations results from the lack of knowledge on the nature of the wavefield, e.g., spatio-temporal distribution of sources, source types, source depths, type and energy content of the radiated waves (Jongmans et al., 2005). The f-k techniques are best suited for the analysis of ambient vibrations resulting from a single source or an azimuthally constrained dominant source region, whereas for the MSPAC analysis, a random source distribution is most favorable. Thus, complementary information of both techniques can be used to enhance phase velocity estimates.

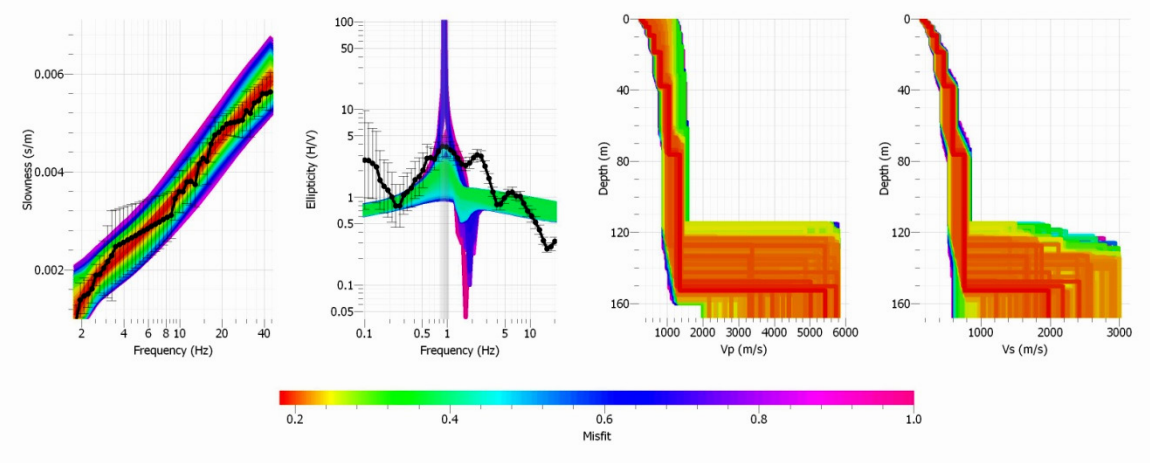

Fig. 9.36 Inversion of dispersion curves; the four frames from left to right: 1) black line: mean dispersion curve with error bars, colored lines: forward computation of dispersion curves for ensemble of final models colored according to misfit; 2) black line: H/V ratio at central array station, colored lines: forward computation of H/V ratios for ensemble of final models; 3) P-wave velocity profile for ensemble of final models; 4) S-wave velocity profile for ensemble of final models, note high uncertainty of both P- and S-wave velocities below strong impedance contrast (figures produced using the dinver software; Wathelet et al., 2004; Wathelet, 2008).

Uncertainties in the phase velocity estimates may arise due to data recording, data processing, and the nature of the ambient vibration wavefield (Jongmans et al., 2005; Bonnefoy-Claudet et al., 2005). The main source of uncertainties is a relative arrival time error between sensor pairs due to instrumentation, phase determination, and violation of the plane wave signal. Time shifts may be either systematic or random (Jongmans et al., 2005). Systematic time shifts are caused by, e.g., unlocked GPS time synchronization, internal clock drifts of digitizers, station positioning errors, differences between phase delays of individual sensors caused by variations of seismometer constants and can be prevented by using only well-calibrated sensors in a sufficient number (at least 5, see Jongmans et al., 2005) having a corner frequency well below the frequency band of interest. For ambient vibration

measurements, the magnitude of random time shifts depends on the energy ratio between coherent versus non-coherent wavefield components (analogue to the SNR). The influence of random time shifts can be reduced by using long analysis windows (25-50 times the center period) in a large number. Additionally, in case of curved wavefronts, predictable time delays will distort the slowness estimate (Almendros et al., 1999) which means that nearby sources must be avoided (d/r < 2.5; Jongmans et al., 2005).

Although wavefronts arriving at an array with aperture A from sources located at distances d >> A are nearly plane as compared to the more curved wavefronts from closer sources (the presence of plane wavefronts is a basic assumption for the f-k analysis), phase velocity curves derived from distant sources may show poor quality due to a lack of coherent energy attributed to the intrinsic attenuation properties of the medium (Jongmans et al., 2005). In addition, for strongly attenuating structures, higher mode energy contributions may dominate for certain frequency bands resulting in jumps of the estimated phase velocity between fundamental and higher mode branches, and intermediate phase velocities for comparable energy levels between different modes of propagation (for description and treatment of "apparent phase velocities", see Tokimatsu et al., 1992; Tokimatsu, 1997).

At sites having a sharp impedance contrast in the subsurface, spectral energy holes in the waveform spectra of the vertical component can be observed at least around the resonance frequency due to the filter characteristics of the subsurface hindering or impeding the determination of the dispersion curve in this frequency range (Scherbaum et al., 2003; Jongmans et al., 2005).

9.11 Array design for the purpose of maximizing the SNR gain

Signal detection at array stations is governed by the gain that can be achieved in the signal-to-noise ratio (SNR) through the process of beamforming. This subsection provides some guidance as to how an array can be designed to maximize this gain. Other aspects of array design (e.g., slowness resolution) have been dealt with elsewhere in this chapter.

9.11.1 The gain formula

The SNR gain *G* by beamforming achievable from seismic array data can be expressed by

$$G^2 = \frac{\sum_{ij} C_{ij}}{\sum_{ij} \rho_{ij}} \tag{9.27}$$

where C_{ij} is the signal cross-correlation between sensors *i* and *j* of an array and ρ_{ij} is the noise cross-correlation between sensors *i* and *j* (see also Section 9.4.5). For an array with M sensors, this formula collapses to the well-known relation $G^2 = M$ for perfectly correlating signals ($C_{ij} = 1$ for all *i* and *j*) and uncorrelated noise ($\rho_{ij} = 0$ for $i \neq j$ and $\rho_{ij} = 1$ for $i = j$).

For any array geometry it is thus possible to predict the array gain if the signal and noise cross-correlations are known for all pairs of sensors of the array layout. The remainder of this subsection describes how to design an array based on the availability of such correlation data.

9.11.2 Collection of correlation data during site surveys

Correlation data for use in the design phase should be collected in a carefully planned site survey. The sensor layout during the survey should be planned so as to represent as many intersensor distances as possible. The first layout for the experiments eventually leading to the deployment of the 25-element NORES array in Norway in 1984 utilized only 6 sensors, in a rather irregular geometry, as shown in Fig. 9.37.

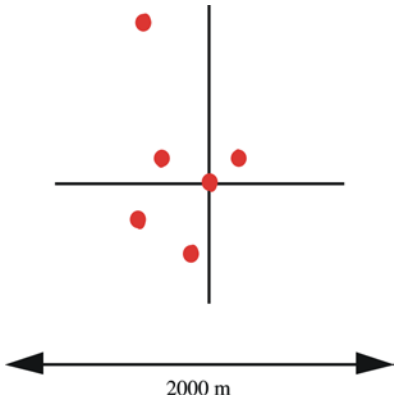

Fig. 9.37 The first array layout for the experiments leading to the design of the 25-element NORES array in Norway in 1984.

The deployment for the collection of correlation data should be done in a way as simple as possible and should take advantage of outcropping bedrock where possible. The layout should preferably comprise ten sensors or more. If, however, for example only six sensors are available for the site survey, one could start out with a configuration something like that in Fig. 9.37 and record data continuously for about one week. At the end of this one-week period, one could redeploy four of the sensors and record data for another week. Two of the sensors would then occupy the same locations for the entire two-week recording period and would provide evidence (or lack thereof) of consistency in the results between the two one-week periods. The largest intersensor separation represented in these data should be, if possible, of the order of 3 km.

The experience from the design of the NORES array showed that the signal and noise correlation curves obtained from the early experiments (with six, and later twelve sensors) possessed most of the characteristic features (Mykkeltveit, 1985) and thus qualitatively resembled the curves derived later on from configurations comprising many more sensors (up to 25).

9.11.3 Correlation curves derived from experimental data

In the processing of the data from the site survey, cross-correlation values must be computed for all combinations of sensor pairs of the experimental layout. Consider, for example, a geometry of six sensors. This geometry comprises 15 unique pairs of sensors. Consider also a short interval of say 30 seconds of noise data (make sure no signal is contained in this time window) and compute the cross-correlation values for each of the 15 unique pairs of sensors (no time shifts are to be introduced for this computation). The time series are first bandpass filtered so as to derive the correlation values of one particular frequency (or frequency band). The 15 correlation values are then plotted in an x-y diagram, where the x-axis represents the intersensor separation and the y-axis the correlation value (between -1.0 and +1.0), resulting in a plot as shown in Fig. 9.38.

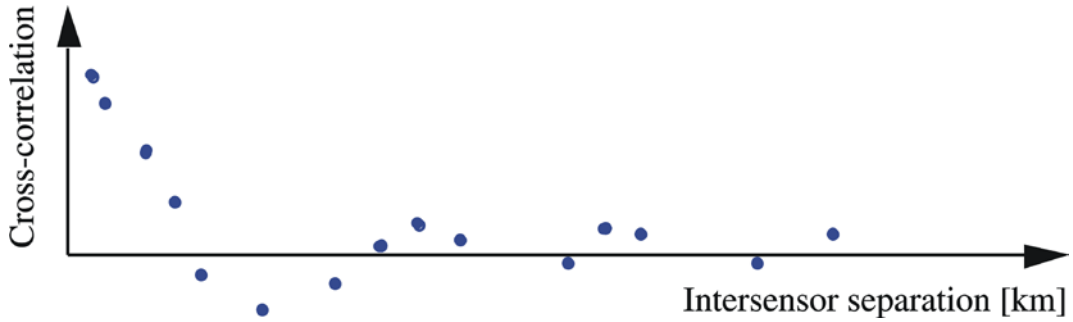

Fig. 9.38 Noise cross-correlation values for a test layout of 6 sensors.

When plotting the cross-correlation values as a function of sensor separation only and thus disregarding possible directional dependencies, an implicit assumption is made of azimuthal symmetry in wavenumber space, over a longer time interval. This assumption is justified by the NORES experience, which shows that only a relatively small scatter is exhibited in the correlation data.

Computations of the kind described above should also be done for signals, which for the purpose of this section will be assumed to be P waves (although design strategies for the detection of S-type phases will be similar to those described here). A recording period of about 14 days during the site survey hopefully should be sufficient to record a reasonable number of representative P-wave arrivals. The time windows for these computations should be relatively short (approximately 5 seconds) to capture the coherent part of the signal arrival. Signal time series must be aligned in accordance with the signal slowness (phase velocity and direction of approach) before the cross-correlation is computed. Again, the time series must be filtered in a relatively narrow band around the peak frequency of the signal being considered. A plot like the one shown in Fig. 9.39 results from this, again assuming a six-sensor layout with 15 unique combinations of sensor pairs.

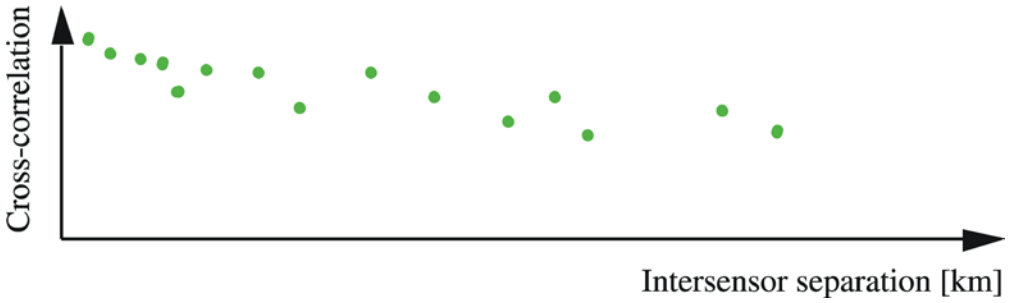

Fig. 9.39 Schematic plot of P-wave cross-correlation values for a test layout of 6 sensors.

Computations as described above should be repeated for various time intervals for the noise, and for various P arrivals recorded during the site survey. Then, for each frequency interval of interest, all data (both noise and signal correlation data) should be combined in one diagram for the purpose of deriving curves (based on interpolation) that are representative of that frequency interval, and that provides correlation values for all intersensor separations. Such diagrams might then appear as shown in Fig. 9.40, in which the upper curve represents the signal correlation and the lower curve the noise correlation.

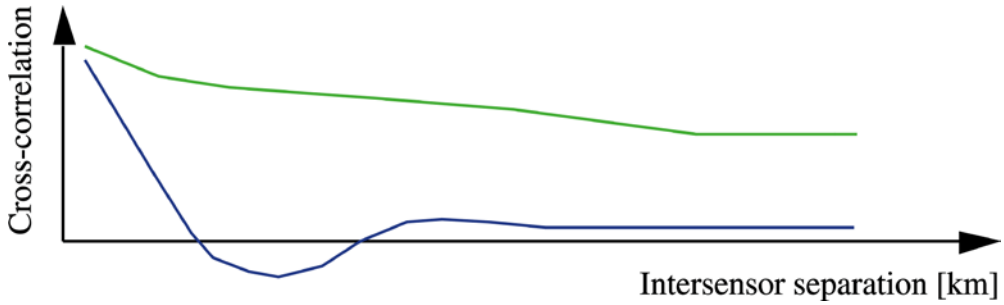

Fig. 9.40 Schematic plot of signal (upper, green) and noise (lower, blue) correlation curves representing experimental data collected for a test array.

For the noise correlation curve in Fig. 9.40 to be representative for 2 Hz, e.g., the noise data should be filtered in a band where 2 Hz is close to the lower limit of the passband, due to the spectral fall-off of the noise. A passband of 1.8 – 2.8 Hz might be appropriate for the noise, but actual noise spectra for the site in question should be computed and studied before this passband is decided on. To generate a signal correlation curve representative for 2 Hz, signals should be used that have their spectral peaks close to this frequency, and some narrow filter passbands centered on 2 Hz should be applied to the data. These curves would then be used to predict gains for various array designs as detailed below.

It should be noted that the rather pronounced negative minima for the noise correlation curves (as schematically represented in Fig. 9.40) are consistently observed for the NORES array. It is the exploitation of this feature that provides for gains in excess of $\sqrt{M}$ (see Section 9.4.5 and Eq. 9.7), commonly observed at the NORES array (or sub-geometries thereof). It should also be noted that this feature of negative noise correlation values is not a universal one; e.g., Harjes (1990) did not find consistently such pronounced negative minima for the GERES test array in Germany.

Braun and Schweitzer (2008) investigated the noise correlation behavior for a test-array installation of three-component sensors in Italy and similar intersensor-noise correlations were found for the rotated horizontal components as for the vertical sensors. The noise-correlation lengths (200 m for signals in the 2 – 4 Hz frequency passband) were about half as long as those observed for NORES. In addition, they also found specific BAZ directions with coherent noise with apparent velocities of Rg-type waves, which may be reducible by special array design.

9.12 Considerations when planning a new seismic array

9.12.1 Basics

Earlier in this chapter we described some older but still operational large seismic arrays. Today, with numerous digital seismic stations and the CTBTO monitoring arrays around the world, there is much less need for new arrays focusing on teleseismic monitoring. However, this is not true for small aperture arrays focusing on seismic sources at local and regional distances.

Based on very positive experiences during the last years with NORES-type, small aperture arrays, a recommended approach would be to use such an array geometry when planning a new array. However, it became also clear that an array does not necessarily need to consist of as many sites as NORES with its 25 sites. Quite good slowness (i.e., apparent velocity and backazimuth) estimates can already be achieved with SPITS-type arrays consisting of nine sites (corresponding to the A and B rings of NORES, see Fig. 9.41). The aperture of such a nine-element array should be between 750 and 1500 m depending on the local noise conditions (see Section 9.12.2). Then, even the identification and rough classification of teleseismic onsets is still possible.

With respect to instrumentation, it is no problem to keep the single sensors as broadband as possible. In particular when monitoring stronger events at local or regional distances the recording of higher frequencies in parallel with seismic low frequency energy can be of high importance, e.g., the new SPITS array is equipped with nine broadband, acceleration-proportional sensors, with a flat response between 100 s and 35 Hz.

A general problem of existing arrays is that they all record seismic waves predominantly with the use of vertical sensors only. Thereby, S-phase observation is much more difficult and limited to S phases with strong SV particle movements. This problem, discussed since some time, was partly solved for NORES-type arrays by installing three-component sensors at several sites (e.g., Schweitzer, 1994; Schweitzer and Kværna, 2002; Braun et al., 2004; Gibbons et al., 2011). Today, we can recommend equipping as many array sites as possible with three-component sensors as e.g., is the case for the refurbished Gräfenberg array, which has now three-component sensors at all 13 sites, and SPITS, which is equipped at six of nine sites with three-component sensors (Gibbons et al., 2011).

Finally, we would still like to recommend a central timing system for any array. During the last decades many cases were observed of malfunctioning single clocks at individual array sites, which produced unexpected (and sometimes undetected) wrong slowness results due to small time shifts. If the central clock of an array is showing a wrong time, the absolute onset times of seismic phases may be influenced, but the array itself is still functional.

9.12.2 Example: A possible design strategy for a 9-element array

As an example of application of the design ideas outlined above, let us consider practical aspects of the design of a 9-element array. Several new arrays that have been built by the CTBTO for the International Monitoring System (IMS) for CTBT monitoring comprise 9 elements. A useful design for a new 9-element array would be one for which there are 3 and 5 elements equidistantly placed on each of two concentric rings, respectively, plus one element at the center of the geometry, as shown in Fig. 9.41.

The elements on the two rings should be placed so as to avoid radial alignment, which would produce stronger side lobes in the array transfer function as any regular pattern of the array geometry. If the five elements of the outer ring are placed at 0, 72, 144, 216 and 288 degrees from due North, the elements of the inner ring might be placed at 36, 156 and 276 degrees, as shown in Fig. 9.41. Within this class of design, the problem at hand is thus to find the radii of the two rings that for a given site would provide the best overall array gain. To constrain the design options even further, one might consider adopting the NORES design idea, limited to these two rings. The radii of the four NORES rings are given by the formula:

$$R = R_{\min} \cdot 2.15^{n}, (n = 0,1,2,3) \tag{9.28}$$

For NORES, R_{min} = 150 m. For the design problem at hand, only R_{min}, the radius of the inner ring, remains to be determined from the correlation data, whereas the radius of the outer ring would then be 2.15 times the radius of the inner ring.

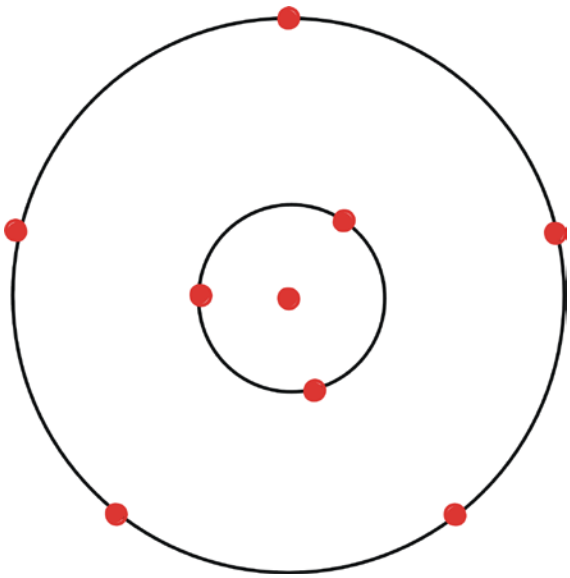

Fig. 9.41 The figure shows a possible design for a 9-element array.

The final step in the procedure outlined here is to compute expected gains for various array designs within this class of geometries. To this end, one must determine which signal frequencies are of the largest importance with regard to the detection capability of the array at the site under study. Assuming that three dominating P-wave signal frequencies, f_1, f_2 and f_3, (e.g., 1.8, 2.5 and 3.5 Hz) have been identified in the preparatory survey, these should be taken into account in the computations to derive the optimum array geometry. We would then

have available from the site survey empirically-based correlation curves in analytical or tabular form that would provide correlation values for **all** intersensor separations of interest. The gains as a function of frequency for various values of the parameter R_{min} could then be computed using the formula for the array gain and the correlation values derived from the correlation curves, for the relevant intersensor separations. The results of these computations could be tabulated as indicated in the (here artificial) Tab. 9.1. For more details and application of these analysis steps see Mykkeltveit (1985).

Note that for the lowest frequency considered (f_1), it might pay in terms of array gain to exclude the elements of the inner ring from the gain computations, since noise correlation values for low frequencies may be high for many sensor pairs involving sensors of relative short intersensor distances (e.g., the innermost sensor rings).

Tab. 9.1 Example for a table providing gains achievable by beamforming when applying different values of the parameter R_{min}.

R_{min} [m]	Gain (f_1) [dB]	Gain (f_2) [dB]	Gain (f_3) [dB]
200	3	6	8
300	4	8	9
400	5	9	7
...	...	...	...
1000	9	7	4
...	...	...	...

The optimum geometry would correspond to the value of R_{min} that gives the best overall gain in Tab. 9.1. This judgment would be based on some appropriate weighting scheme for the frequencies considered.

The procedure outlined here could be generalized to a class of designs for which the radii of the two rings are varied independently. Gain values would then be tabulated as shown in Tab. 9.1, but there would now be a sequence of tables (each table would represent a fixed radius of one of the two rings). The search for the optimum geometry would then be performed across all these tables.

9.13 Routine processing of array data at NORSAR

9.13.1 Introduction

Now, we will explain the main features of the automatic routine processing of data recorded by regional arrays at NORSAR (Fyen 1989; 2001a and b).

As aforementioned in Section 9.2, the array data processing can be divided into three steps:

- Detection Processing (DP), i.e., performing STA/LTA triggering on a number of predefined beams;

- Signal Attribute Processing (SAP), i.e., performing signal feature extraction of detected signals, such as onset times, amplitudes, and frequencies/periods of identified phases; and
- Event Processing (EP), i.e., performing phase association, location processing and event plotting.

In Mykkeltveit et al. (1988) and in Kværna (1989), it is shown that different combinations of sensors, for example, within the NORES array, give different noise reduction for various frequency bands. The lesson is that it is not always optimal to use all seismometers of the array to form a beam; rather one should in general use different sub-configurations, tailored to the signal frequencies.

Fig. 9.16 showed different beams for the same P-wave signal. It is obvious from this figure that we need beams for various slowness vectors to detect the signal.

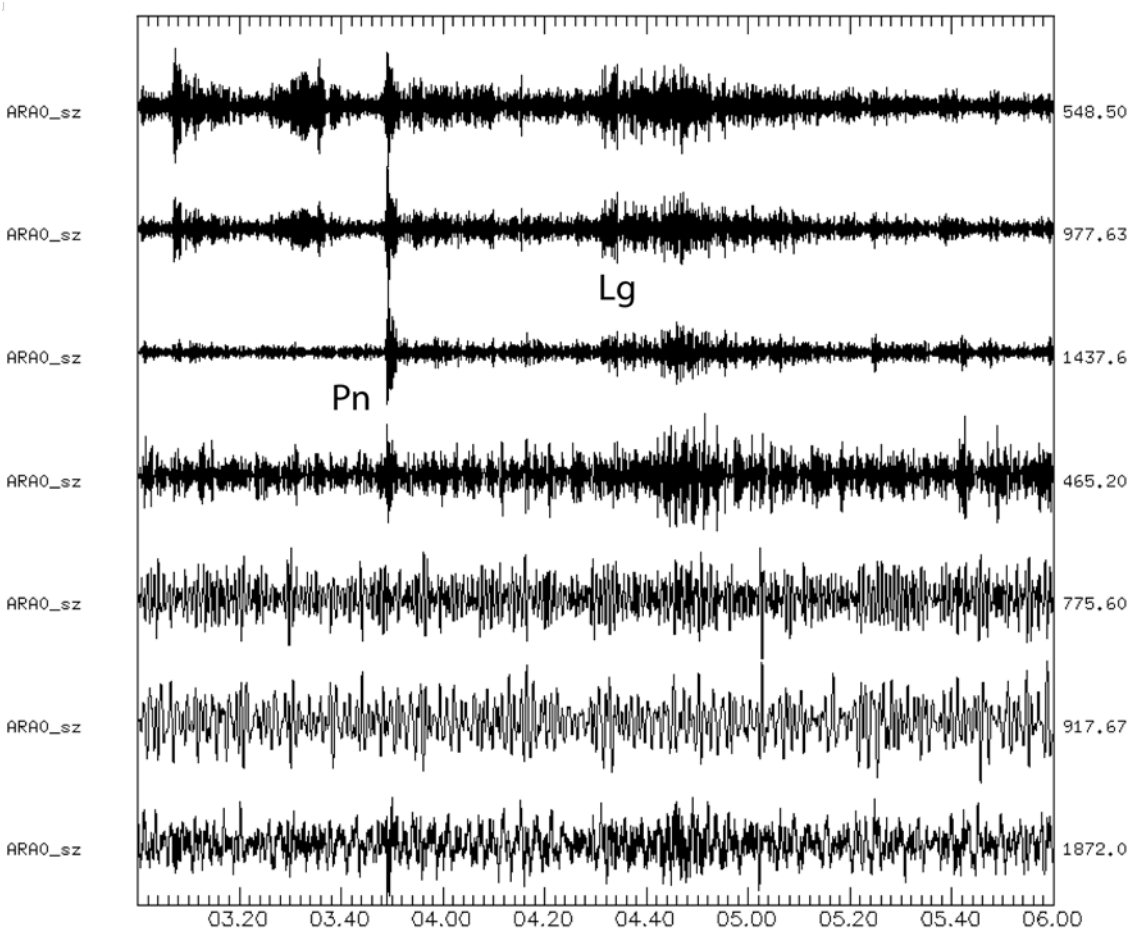

Fig. 9.42 The bottom trace shows raw data from instrument A0 at the center of the ARCES array. The next traces from bottom to top are data from the same instrument filtered with 3rd order Butterworth bandpass filters using frequency bands 0.5 – 1.5, 1 – 3, 2 – 4, 4 – 8, 6 – 12, and 8 – 16 Hz, respectively.

We have earlier pointed out the importance of beamforming and filtering for signal enhancement. In the array detection process, several beams are formed, and several different filters are used (see Tab. 9.2). An STA/LTA detector is used on each beam, and as seen from

Fig. 9.17, we may get a trigger on several beams. The detector will compare the maximum STA/LTA (SNR) for every beam within a (narrow) time window. The influence of different filters on the detectability of seismic signals is demonstrated in Fig. 9.42. It shows ARCES data with one of the seismometer outputs filtered in different filter bands. An important point made in this figure is that the regional seismic phases Pn and Lg have their best SNR in different frequency bands. So to be sure to detect both phases, we should use several filter bands in the detector recipe.

Tab. 9.2 An example for a detection beamset as it was in use at NORSAR for many years for the SPITS array. THR is the SNR threshold used to define a state of detection and "all" means that the whole SPITS array (SPA0, SPA1, SPA2, SPB1, SPB2, SPB3, SPB4, and SPB5) is used to form this beam (from Schweitzer, 1998).

BEAM NAMES	VELOCITY [km/s]	BACKAZIMUTH [deg]	FILTER		THR	SITES (verticals only)
			bandpass [Hz]	order		
S001	99999.9	0.0	0.8 – 2.0	4	4.5	SPA0 SPB1 SPB2 SPB3 SPB4 SPB5
S002	99999.9	0.0	0.8 – 2.0	4	4.5	all
S003	99999.9	0.0	1.0 – 3.0	3	4.5	SPA0 SPB1 SPB2 SPB3 SPB4 SPB5
S004	99999.9	0.0	1.0 – 3.0	3	4.5	all
S005	99999.9	0.0	2.0 – 4.0	3	4.0	SPA0 SPB1 SPB2 SPB3 SPB4 SPB5
S006	99999.9	0.0	2.0 – 4.0	3	4.0	all
S007	99999.9	0.0	3.0 – 5.0	3	4.0	SPA0 SPB1 SPB2 SPB3 SPB4 SPB5
S008	99999.9	0.0	3.0 – 5.0	3	4.0	all
S009	99999.9	0.0	0.9 – 3.5	4	4.5	SPA0 SPB1 SPB2 SPB3 SPB4 SPB5
S010	99999.9	0.0	0.9 – 3.5	4	4.5	all
S011	99999.9	0.0	1.0 – 4.0	3	4.5	SPA0 SPB1 SPB2 SPB3 SPB4 SPB5
S012	99999.9	0.0	1.0 – 4.0	3	4.5	all
SA01 – SA04	10.0	0 90 180 270	1.0 – 3.0	3	4.5	SPA0 SPB1 SPB2 SPB3 SPB4 SPB5
SA05 – SA08	10.0	45 135 225 315	1.0 – 3.0	3	4.5	all
SA09 – SA12	10.0	0 90 180 270	2.5 – 4.5	3	4.0	SPA0 SPB1 SPB2 SPB3 SPB4 SPB5
SA13 – SA16	10.0	45 135 225 315	2.5 – 4.5	3	4.0	all
SA17 – SA20	10.0	0 90 180 270	4.0 – 8.0	3	4.0	SPA0 SPB1 SPB2 SPB3 SPB4 SPB5
SA21 – SA24	10.0	45 135 225 315	4.0 – 8.0	3	4.0	all
SA25 – SA28	10.0	0 90 180 270	3.0 – 6.0	3	4.0	SPA0 SPB1 SPB2 SPB3 SPB4 SPB5
SA29 – SA32	10.0	45 135 225 315	3.0 – 6.0	3	4.0	all
SB01 – SB04	7.0	0 90 180 270	1.0 – 4.0	3	4.5	SPA0 SPB1 SPB2 SPB3 SPB4 SPB5
SB05 – SB08	7.0	45 135 225 315	1.0 – 4.0	3	4.5	all
SB09 – SB12	7.0	0 90 180 270	3.0 – 6.0	3	4.0	SPA0 SPB1 SPB2 SPB3 SPB4 SPB5
SB13 – SB16	7.0	45 135 225 315	3.0 – 6.0	3	4.0	all
SB17 – SB20	7.0	0 90 180 270	5.0 – 10.0	3	4.0	SPA0 SPB1 SPB2 SPB3 SPB4 SPB5
SB21 – SB24	7.0	45 135 225 315	5.0 – 10.0	3	4.0	all
SC01 – SC04	5.0	0 90 180 270	1.0 – 4.0	3	4.5	SPA0 SPB1 SPB2 SPB3 SPB4 SPB5
SC05 – SC08	5.0	45 135 225 315	1.0 – 4.0	3	4.5	all
SC09 – SC12	5.0	0 90 180 270	3.5 – 5.5	3	4.0	SPA0 SPB1 SPB2 SPB3 SPB4 SPB5
SC13 – SC16	5.0	45 135 225 315	3.5 – 5.5	3	4.0	all
SC17 – SC20	5.0	0 90 180 270	5.0 – 10.0	3	4.0	SPA0 SPB1 SPB2 SPB3 SPB4 SPB5
SC21 – SC24	5.0	45 135 225 315	5.0 – 10.0	3	4.0	all
SC25 – SC28	5.0	0 90 180 270	8.0 – 16.0	3	4.0	SPA0 SPB1 SPB2 SPB3 SPB4 SPB5
SC29 – SC32	5.0	45 135 225 315	8.0 – 16.0	3	4.0	all
SD01 – SD08	4.0	0 45 90 135 180 225 270 315	0.9 – 3.5	4	4.5	all
SD09 – SD16	4.0	0 45 90 135 180 225 270 315	3.0 – 6.0	3	4.0	all
SD17 – SD24	4.0	0 45 90 135 180 225 270 315	4.0 – 8.0	3	4.0	all
SE01 – SE08	3.3	0 45 90 135 180 225 270 315	1.5 – 3.5	3	4.5	all
SE09 – SE16	3.3	0 45 90 135 180 225 270 315	3.0 – 6.0	3	4.0	all
SE17 – SE24	3.3	0 45 90 135 180 225 270 315	5.0 – 10.0	3	4.0	all
SF01 – SF08	2.5	0 45 90 135 180 225 270 315	1.0 – 4.0	3	4.5	all
SF09 – SF16	2.5	0 45 90 135 180 225 270 315	2.0 – 4.0	3	4.0	all
SF17 – SF24	2.5	0 45 90 135 180 225 270 315	3.0 – 5.0	3	4.0	all
SN01	8.4	97.6	2.0 – 4.0	3	3.7	all
SN02	8.4	97.6	3.0 – 5.0	3	3.7	all
SN03	8.4	97.6	4.0 – 8.0	3	3.7	all
SN04	8.4	97.6	6.0 – 12.0	3	3.7	all
SN05	8.4	97.6	8.0 – 16.0	3	3.7	all
SN06	4.7	97.6	2.0 – 4.0	3	3.7	all
SN07	4.7	97.6	3.0 – 5.0	3	3.7	all
SN08	4.7	97.6	4.0 – 8.0	3	3.7	all
SN09	4.7	97.6	6.0 – 12.0	3	3.7	all
SN10	4.7	97.6	8.0 – 16.0	3	3.7	all
SG01 – SG12	2.0	0 30 60 90 120 150 180 210 240 270 300 330	1.5 – 3.5	3	4.5	all
SG13 – SG24	2.0	0 30 60 90 120 150 180 210 240 270 300 330	2.5 – 4.5	3	4.0	all
SG25 – SG36	2.0	0 30 60 90 120 150 180 210 240 270 300 330	3.5 – 5.5	3	4.0	all
SM01 – SM12	1.7	0 30 60 90 120 150 180 210 240 270 300 330	1.0 –3.0	3	4.5	all
SM13 – SM24	1.7	0 30 60 90 120 150 180 210 240 270 300 330	2.0 – 4.0	3	4.0	all
SM25 – SM36	1.7	0 30 60 90 120 150 180 210 240 270 300 330	3.0 – 6.0	3	4.0	all

Thus we have three parameter sets that make up the input for the STA/LTA detector: the specific array configuration, the slowness vector, and the filter band to use for this beam. Note that one could also use just a single seismometer instead of a beam. Based on experiments, a list of these parameters has been compiled at NORSAR that constitutes a "detector recipe" with, e.g., numerous beams using different slownesses, different configurations, and different filter bands. For a large signal, the detector program will trigger on many beams, and the program will use a detection reduction process to report only one detection for each signal.

As an example, a detector recipe listing the entire beam set composed of 254 beams for the online processing of data from the SPITS array, as it was in use at NORSAR for many years, is included in Tab. 9.2. The complete process is illustrated in the following Sections 9.13.2 – 9.13.4 by using a data example from the ARCES array.

9.13.2 Detection Processing – DP

The DP process continuously reads data off a disk loop or any other continuous database and uses beamforming, filtering, and the STA/LTA detector to obtain detections (triggers). Thus the DP program produces, e.g., a single file for each array and each day of the year (DOY).

The following list gives some example lines from such a file for DOY 199 in 1996 for the ARCES (ARC) array. The file contains the name of the detecting beam (e.g., F074), the time of detection (199:16.03.49.3), the end of the detection state (199:16.03.53.1), the maximum STA (242.4), the LTA at the time of detection (10.27), the SNR (STA/LTA = SNR = 23.601), and the number of beams detecting (37). The detecting beam reported (here F074) is the one beam, normally out of many, that detected this signal with the highest SNR. The key parameters reported are the beam code, the trigger time, and the SNR = STA/LTA. The beam code (leftmost column in the list below) points to a file (see Fig. 9.43) containing information on beam configuration, slowness and filter used. The format of a detection output is not important. Important is to create a list of detections that can be used for further analysis.

BEAM	DETECTION TIME	STA	LTA	SNR	# of BEAMS
FH04	199:16.02.18.6 - 02.19.9	106.52	32.15	3.313	1
FH04	199:16.02.39.1 - 02.39.6	116.09	43.91	2.644	1
FH04	199:16.02.44.4 - 02.48.6	296.52	56.63	5.236	5
Fl01	199:16.02.55.5 - 02.56.3	175.40	33.59	5. 221	3
F074	199:16.03.49.3 - 03.53.1	242.40	10.27	23.601	37
FH03	199:16.04.32.9 - 04.50.9	291. 46	73.01	3.992	5
FH02	199:16.04.46.4 - 04.35.9	297.87	75.23	3.960	24
FH04	199:16.09.57.6 - 09.58.9	80.86	24.07	3.359	2

```
THR  =    4.000
BF1  =    3.500
BF2  =    5.500
BMVEL =   11.100
BMAZI =  150.000
REFLAT =   69.535
REFLON =   25.506
REFELE =  403.000
REFSIT = ARA0_sz
SELECTED CHANNELS : ARA0_sz ARB1_sz ARB2_sz ARB3_sz ARB4_sz ARB5_sz
ARC1_sz ARC2_sz ARC3_sz ARC4_sz ARC5_sz ARC6_sz ARC7_sz
```

Fig. 9.43 Example of the contents of a file with the parameters that characterize beam F074. THR is the SNR detection threshold, BF1 and BF2 are the lower and the upper limits of the bandpass filter applied, BMVEL and BMAZI are the apparent velocity and the backazimuth for this beam, REFLAT, REFLON, REFELE, and REFSIT define the reference site of the beam, and SELECTED CHANNELS lists the site configuration.

9.13.3 Signal Attribute Processing – SAP

This process sequentially reads detections from the detection file and performs an f-k analysis for each detection to estimate apparent velocity and backazimuth. The estimated velocity and backazimuth is referred to as "observed slowness". Waveform segments for the analysis are again read from a disk loop or any other database.

A special version of NORSAR's EP program is used and produces a new file for the ARCES array on day-of-the-year (DOY) (here 199 in 1996). The key parameters reported in the EP-result files are the signal onset time, the beam code, the SNR, the estimated slowness, the signal amplitude and frequency, and the phase identification based on the slowness estimate.

#	ONSET TIME	DT	BEAM	SNR	VEL	PHASE	BAZ	POWER	Q	FREQ	AMP	STA	IP	IS	REC	H/V	INC 1	INC 3
5	199:16.02.18.314	0.29	FH04	3.3	2.4	nois	256.5	0.30	4	9.22	343.4	106.5	1	-3	0.63	0.86	19.32	81.70
10	199:16.02.36.964	2.14	FH04	2.6	2.4	nois	246.6	0.37	3	9.79	466.6	116.1	1	-3	0.75	0.29	6.02	88.69
15	199:16.02.43.014	1.39	FH04	5.2	2.4	nois	243.4	0.56	3	9.79	906.9	296.5	1	-3	0.56	0.69	10.38	80.87
20	199:16.02.54.915	0.58	F101	5.2	2.4	nois	236.7	0.59	3	9.84	1021.5	175.4	1	-3	0.63	0.42	10.56	86.32
25	199:16.03.48.409	0.89	F074	23.6	7.5	Pgn	122.7	0.71	2	4.85	518.5	242.4	0	-3	0.72	0.61	48.76	68.81
30	199:16.04.32.160	0.74	FH03	4.0	5.4	SN	117.4	0.29	3	6.30	581.6	291.5	D4_sz		0.37	1.78	10.97	12.82
35	199:16.04.45.785	0.62	FH02	4.0	4.1	LG	127.2	0.28	3	4.88	552.1	297.9	D4_sz		0.44	1.10	78.22	72.30
40	199:16.09.55.770	1.83	FH04	3.4	2.4	nois	197.7	0.37	4	9.48	228.7	80.9	-1	-2	0.63	1.24	87.74	68.06
45	199:16.10.39.171	1.33	F106	4.8	2.5	nois	221.7	0.44	3	8.38	226.2	59.7	1	-3	0.74	0.40	18.91	76.60

Fig. 9.44 Example of the contents of a file with the Signal Attribute Processing results for the detections listed in Fig. 9.43.

A few lines from such a file are listed above (Fig. 9.44). The entries are the arrival id number (e.g., 25), the estimated onset time (199:16.03.48.409), the difference time (DT) between trigger and onset time (0.89 s), the beam name (F074), the SNR (23.6), the apparent velocity (VEL in km/s) from f-k analysis (7.4), the preliminary phase name by automatically considering apparent velocity and three-component polarization analysis (Pgn, which is used

here as a code for ‘either Pg or Pn’), the estimated backazimuth (BAZ) from f-k analysis (122.5°), the relative power from f-k analysis (0.72, a number between 0.0 (no signal coherency) and 1.0 (perfect signal coherency)), the f-k analysis quality indicator (Q) (2, 1=best, 4=poor), the estimated dominant frequency (FREQ) in Hz (4.85), the maximum amplitude (AMP) in counts (476.9), the maximum STA of the detection (242.4), the polarization analysis classifications IP, IS (0 and –3, respectively), the polarization analysis rectilinearity (REC) (0.69), the horizontal/vertical ratio (H/V) (0.49), the inclination angle (INC) (41.26°), and the polarization angle (POL) (73.94°).

Fig. 9.45 shows raw data for the detection reported at time 199:16.03.49.3 (see the detection result listing). The signal attribute process will use this detection time to measure a first onset time of the signal and then to select a 3 second wide time window starting 0.5 second before the preliminary onset time (here 199:16.03.48.4, see also the time window indicated by vertical lines). The data from all vertical seismometers within this time window will then be used for f-k analysis to obtain the true apparent velocity of the signal.

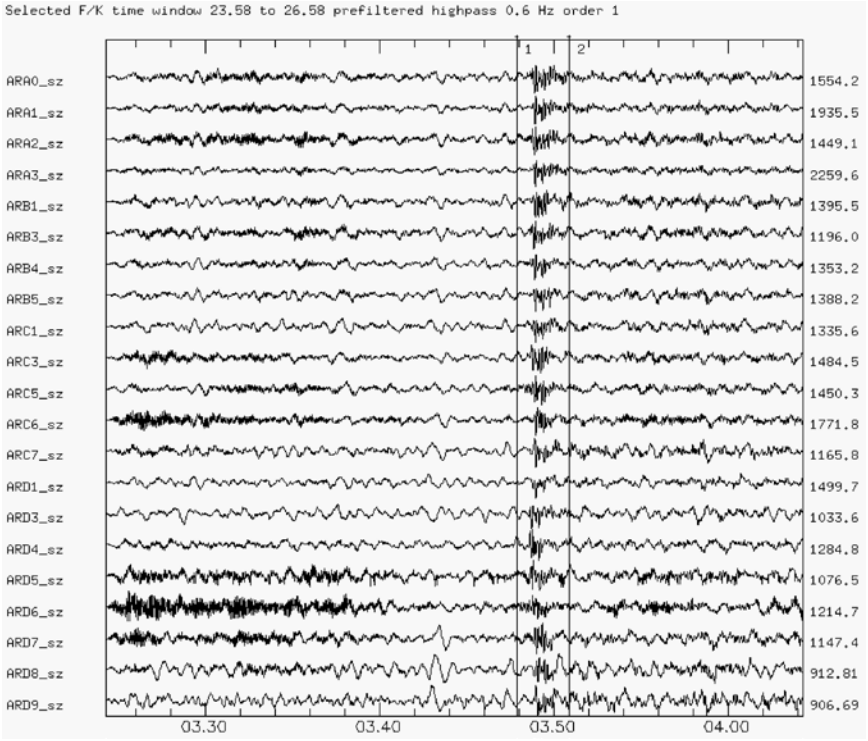

Fig. 9.45 Raw data from all the vertical seismometers of the ARCES array. The time interval contains the Pn phase of a regional event. The vertical bars define a 3 second time window that is used for the f-k analysis.

The result for the f-k analysis is shown in Fig. 9.46. This process is repeated for all detections and Fig. 9.47 shows the data interval selected for the Lg detection. The corresponding f-k analysis results are shown in Fig. 9.48. In automatic mode, of course, the EP program will not display any graphics. The figures are only produced for illustration purposes. However, the capability of displaying results graphically at any step of a process is essential to be able to develop optimum recipes and parameters. The EP program may output results into flat files or a database.

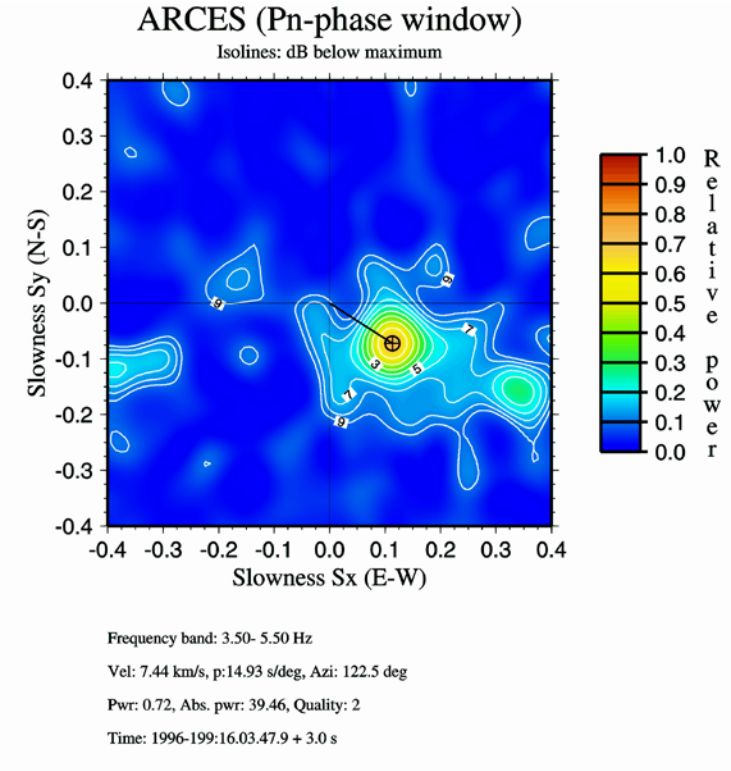

Fig. 9.46 Result of the wide-band f-k analysis for the data in Fig. 9.45, pertaining to the Pn-phase interval.

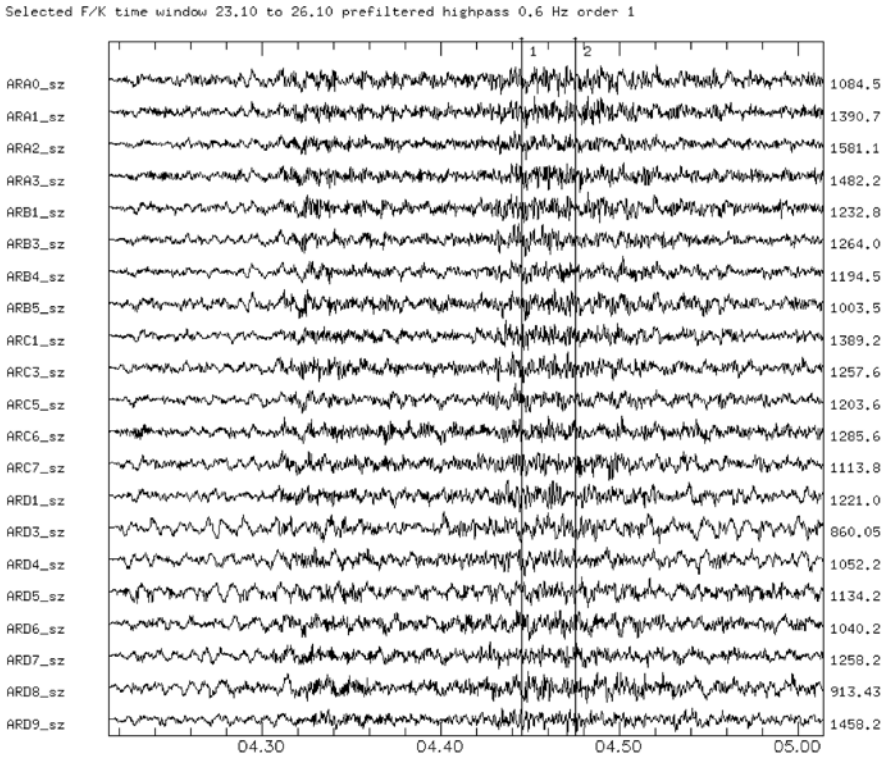

Fig. 9.47 Raw data from all the vertical seismometers of the ARCES array. The time interval contains the Lg phase of a regional event. The vertical bars define a 3 second time window that is used for the f-k analysis.

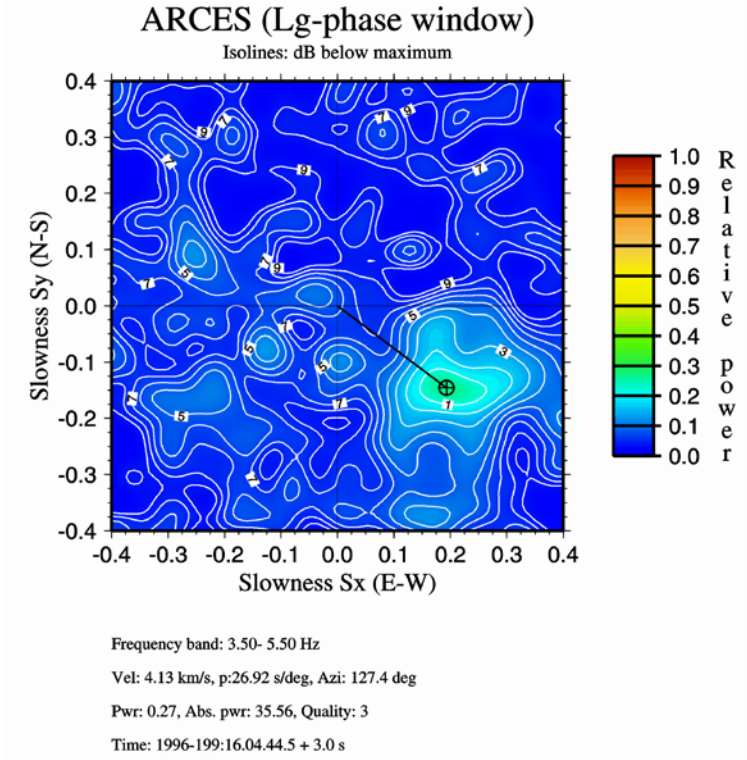

Fig. 9.48 Result of the wide-band f-k analysis for the data in Fig. 9.47, pertaining to the Lg-phase interval.

9.13.4 Event Processing – EP

This process sequentially reads all detections from the parameter extraction processing file. Whenever a detection with an apparent velocity greater than, e.g., 6.0 km/s is found, it is treated as P. Additional detections are searched for, and if additional detections are found with backazimuth estimates not more than, e.g., the predefined azimuth range of 30° from the first detection and a detection time not more than 4 minutes from the first detection, they are used as associated detections. If detections with an apparent velocity less than 6.0 km/s are found, then they are treated as S (Sn, Lg). If phases within 4 minutes and backazimuth deviation of less than 30° with a first P and an S later are found, then they are treated as observations from a regional event. A location routine, which uses the backazimuth information, is used to locate the regional event. More details on these topics are given in Mykkeltveit and Bungum (1984). The results are again written in a separate file for each DOY (here 199 in 1996). A few lines from such files are exemplarily listed below:

5	199:16.02.18.3	FRS	nois	0.148	9.2	3.3	FH04	2.4	256.5	Noplot3ci
10	199:16.02.37.0	FRS	nois	0.205	9.8	2.6	FH04	2.4	246.6	Noplot3ci
15	199:16.02.43.0	FRS	nois	0.398	9.8	5.2	FH04	2.4	243.4	Noplot3ci
20	199:16.02.54.9	FRS	nois	0.449	9.8	5.2	F101	2.4	236.7	Noplot3ci
10		HYP	724	BALTIC STATES-BELARUS-NW RUSSIA						
10	199:16.02.51.2	EPX		67.382	33.506	1.03		404.3	122.5	0F
25	199:16.03.48.4	FRS	PN	0.291	4.8	23.6	F074	7.5	122.7	LOCATE
30	199:16.04.32.2	FRS	SN	0.273	6.3	4.0	FH03	5.4	117.4	LOCATE
10	199:16.04.44.6	MAG	ML	0.337	4.9	602.8	aVG	3.6	122.5	LOCATE
35	199:16.04.45.8	FRS	LG	0.309	4.9	4.0	FH02	4.1	127.2	LOCATE
40	199:16.09.55.8	FRS	nois	0.099	9.5	3.4	FH04	2.4	197.7	Noplot3ci
45	199:16.10.39.2	FRS	nois	0.097	8.4	4.8	F106	2.5	221.7	Noplot3ci

Whenever an event is declared, a location is performed and reported with two lines (**HYP** and **EPX**) that contain event number (10), origin time (199:16.02.51.2), latitude (67.369°), longitude (33.479°), ML (1.01), distance in [km] (404.3), backazimuth (122.7°), fixed depth at 0 km (0F). The associated phases are listed thereafter, and for the Pn phase we have the id number (25), the arrival time (199:16.03.48.4), the station name (FRS, the old, NORSAR-internal code for ARCES), the phase name (PN), the maximum amplitude in [nm] (0.268), the corresponding dominant frequency in [Hz] (4.8), the SNR (23.6), the beam name (F074), the apparent velocity (7.4), the backazimuth (122.5°), and an explanatory code from the location process. **LOCATE** means that this phase was used for locating the event and **ASSOC** means that this onset was associated but not used for the location processing. **Tele** means that this phase is interpreted as a teleseismic onset and **Noplot3ci** means that this phase was not used for any event definition. Such onsets are then also often declared as **nois** (i.e., noise) observations. The "beam-name" **aVG** in a **MAG** line means that the corresponding arrival time is used for measuring the amplitude for **ML** as average amplitude of all traces, and the apparent velocity is the group velocity in that case. The key parameters reported are the origin time, the hypocenter, and the magnitude for each located event, and onset time, amplitude and frequency, SNR, beam code, and apparent velocity for all associated detections.

The example above identifies one group of phases with backazimuth around 123° that are arriving within 4 minutes. The first phase within the group has a regional P-wave apparent velocity, and it is followed by a phase with a regional S apparent velocity. Those are the predefined criteria for defining an event. For each declared event, an event plot may be created (see Fig. 9.49). Results of the automated regional array processing at NORSAR can be found at http://www.norsardata.no/NDC/bulletins/dpep.

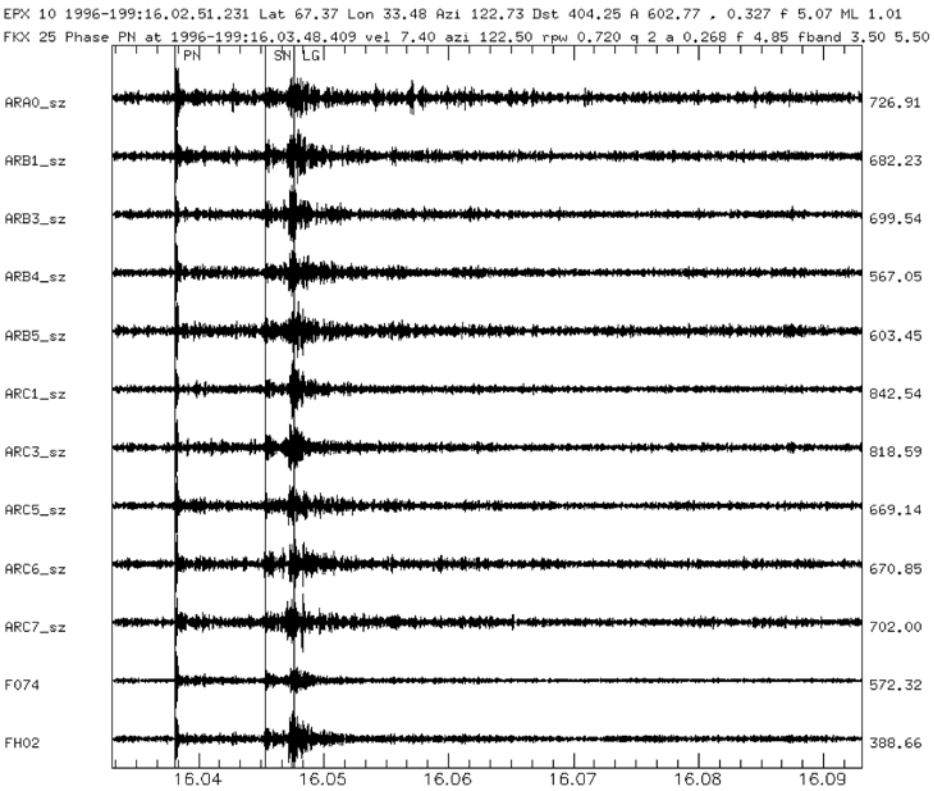

Fig. 9.49 Summarizing plot for the above discussed regional event.

9.13.5 Event location with a network of arrays

It became very soon obvious that the location precision of single small aperture arrays is quite limited mostly due to scatter in the backazimuth estimates and uncertainties in automatically measuring the travel-time differences between P- and S-type onsets. After building up a network of small aperture arrays in Northern and Central Europe during the late 1980s and early 1990s, a joint interpretation of observations from several small aperture arrays could be tested. One successful approach became the Generalized Beam Forming (GBF) location algorithm. This algorithm, developed at NORSAR, can automatically utilize the results of several seismic arrays in a common bulletin (Ringdal and Kværna, 1989; Kværna et al., 1999). Today, data from the highly sensitive regional arrays ARCES, FINES, HFS, SPITS, and NORES, and the teleseismic NORSAR array (NOA) are automatically processed in on-line mode applying this regional and local event-location process (http://www.norsardata.no/NDC/bulletins/gbf). For events observed at several arrays (i.e., events with local magnitudes above 2) these fully automatically achieved GBF locations are usually within a distance of 10 to 50 km from the analyst reviewed event locations (http://www.norsardata.no/NDC/bulletin/regional/). However, the location capabilities are very much depending on the relative location of the events to the geometry of the array network and the number of observed phases.

9.13.6 Teleseismic event location

Benndorf (1906; 1907) published that in the case of a spherically symmetric Earth model apparent velocities (or the seismic ray parameters) are constant along their whole ray path through the Earth (Benndorf's Law). If the velocities inside the Earth are known, it can easily be shown that the ray parameter of seismic onsets changes with the epicentral distance and that an observed ray parameter (or apparent velocity) can directly be inverted for the epicentral distance.

For modern spherically symmetric Earth models and seismic arrays of at least 10 km aperture, this principle works fine for first arriving P-type onsets from seismic events at teleseismic distances (*i.e.*, from about 25° to about 100° epicentral distance). Events at shorter distances are hard to locate because the derivative of the apparent velocity with respect to distance is very small and triplications of the travel-time curve do not allow for a unique correspondence between apparent velocity and distance. At distances beyond ~90° these derivatives become for P waves again very small and in the Earth's shadow zone for P (D >100°) the interpretation of the different core-phase onsets is also quite difficult and limits the location capabilities of a seismic array. Knowing the epicentral distance, the observed BAZ can then be used to define the epicentral coordinates.

The described event location technique has been in use at least since the 1960s and a quick look in the bulletins of the International Seismological Centre shows the huge amount of reported teleseismic event locations made with, e.g., the Large Aperture Seismic Array (LASA) in Montana, USA, the Yellowknife Array (YKA) in Northern Canada, the Gräfenberg Array (GRF) in Bavaria, Germany, or the large Norwegian Seismic Array (NOA) in southern Norway.

For the large NORSAR array (NOA), we may choose between frequency-domain f-k analysis or the beampacking process. The benefit of using beampacking rather than frequency domain f-k analysis is that for every point in slowness space, we can use time delay corrections (see Section 9.5.4) and obtain a calibrated slowness. On the basis of phase identification and measured slowness, we then get an epicentral distance by screening a slowness table and thereby a location using distance and backazimuth. So, for each detection a corresponding location is provided by NORSAR's near real-time array data processing. All results of the automatic array processing of the NOA array can be found at http://www.norsardata.no/NDC/bulletins/dpep.

9.14 Seismic arrays in Earthquake Early Warning Systems (EEWS)

9.14.1 Introduction

The advantage of applying seismic array techniques in EEWS is connected with the capability of an array not only to observe a seismic signal but also to measure its propagation direction and apparent velocity. However, the capability of an array to measure the backazimuth (BAZ) and apparent velocity with sufficient accuracy and to suppress other than the target signals is very much depending on the array geometry and the number of its sensors. Therefore, not each array is equally suitable for an Earthquake Early Warning System (EEWS). Here, we will focus on the usage of seismic arrays as EEWSs in general and in particular on real-time algorithms and discuss the advantages and disadvantages of applying array-analysis techniques as input for any EEWS.

9.14.2 Examples for array contributions to fast event locations

9.14.2.1 Single array results

As mentioned earlier, it is possible to locate seismic events with data observed by one or more seismic arrays. However, in the case of any fast event location algorithm array analysis can only contribute if the whole data processing is automated. On the other hand, the recorded data volume of seismic arrays is very large, thus also requiring automated data processing techniques. Therefore, array data processing algorithms were as much as possible automated since the 1960s. For example, NORSAR's program package DP/EP as described in Section 9.13 was mostly developed in the 1970s – 1990s and later adapted to many other array installations (Fyen, 1989; 2001a and b).

After international exchange of emails was becoming more reliable and common in the early 1990s, it became possible to report event locations or strong P-phase observations based on fully automatic data processing algorithms. Thereby, results from the NORSAR, YKA, or the GERES array were automatically sent to, e.g., the USGS for its Quick Epicenter Determinations (QEDs), the European-Mediterranean Seismological Center (EMSC), the Swiss Seismological Service (SED), and the wider interested seismological community.

9.14.2.2 The Fast Earthquake Information Service (FEIS) algorithm

At the University of Bochum a special alert system was developed in the mid 1990s, which combined the mentioned single array observations with recordings of the newly at that time installed German Regional Seismological Network (GRSN). The so-called Fast Earthquake Information Service (FEIS) algorithm (Schulte-Theis et al., 1995; Harjes et al., 1996) was triggered by strong local or regional events observed by the GERES array. For this, the data of the regional GERES array were automatically analyzed in real time by applying the DP/EP array software developed at NORSAR (Fyen, 1989; 2001a and b, see also Section 9.13). After each automatic GERES location with a local magnitude above 3, the FEIS algorithm was triggered, consisting of the following steps:

- recalculation of an initial location from the GERES data alone;
- calculation of theoretical onset times for regional phases (Pn, Pg, Sn, Sg) at all GRSN stations;
- polling of all automatic GRSN-detection lists via telecommunication lines for a larger time interval around the assumed arrival times;
- searching a small time interval around the theoretical onset times for Pg or Pn detections, depending on the epicentral distance;
- in the case that a P-type phase could be associated, the detection lists were searched for possible S-type detections in a distance-depending predefined time window;
- relocation of the event with the GERES-observation parameters (phase names, onset times, BAZs) and the applicable GRSN detections;
- in the case of a stable location result, the determined location was distributed automatically to interested addresses in Europe.

A comparison with PDE (USGS) locations indicated that the automatic FEIS-relocation procedure significantly improved the original automatically achieved GERESS location accuracy, in particular for events, which occurred within the GRSN.

9.14.2.3 NORSAR's Event Warning System (NEWS)

Since 2000, a new quick event-location system was developed at NORSAR to provide fast and reliable solutions in the case of strong events: NORSAR's Event Warning System (NEWS) (Schweitzer, 2003). The whole NEWS algorithm is based on high Signal-to-Noise Ratio (SNR) detections; whenever one of the contributing arrays observes a P-type onset with an SNR larger than a predefined threshold, the NEWS process is initialized.

Once triggered, the NEWS process searches the automatic result lists of all other available arrays for corresponding onsets. Corresponding in this context means that the other onsets have to come from a backazimuth, and with an apparent velocity, which is consistent with the triggering onset. Formulating robust rules for which onsets can eventually be associated with the same event, was a quite cumbersome procedure. However, as implemented today, these rules are built on travel-time differences between the onset times at the different stations, measured backazimuth and apparent velocity of the signals, and SNR of the onsets. In the case of a presumably local or regional event, NEWS also searches for S-type onsets in the onset lists of the arrays.

After all available lists are searched the NEWS process locates the seismic event. To make this automatic event location as robust as possible, onset times and apparent velocity values are only used from first P and S arrivals. However, to use as much as possible information from the seismic arrays, all onsets in compliance with the selection rules and the measured backazimuth values are used to locate the event. Depending on the mean apparent velocity of all detected P onsets, the program defines the event as probably regional, or as near, far or very far teleseismic. Then, together with the mean backazimuth estimation, an initial source region is chosen. Depending on this initial solution, either a regional or a global velocity model is used to locate the event. The observed P amplitudes can be used to calculate a preliminary event magnitude.

For the determination of the source parameters NORSAR's location program HYPOSAT (see PD.11.1) is used. With the limited amount of data available for locating the event, the event's depth cannot be resolved and has therefore to be fixed to a predefined value. However, until now, such preliminary locations have been sufficient for preliminary information to the public in the case of local or regional events. Although the used network of seismic arrays has an aperture of about 18 degrees in the north-south direction, teleseismic events are usually observed over only a very small azimuth range. Therefore, the small number of available observations produces solutions with limited accuracy and large error bars, and some events are even not locatable. This is in particular true for events in the South Pacific, for which only PKP-type onsets can be observed.

On average, NEWS solutions are available between a few and up to about 10 minutes after the first P onsets have been recorded at one of the seismic arrays. A listing of the most recent NEWS solutions is available on the web (http://www.norsardata.no/NDC/ael/eventmap.html) and NEWS solutions are disseminated to international data centers, which also work on quick epicenter determinations. The delay of several minutes between the source time and the dissemination of source parameters of regional events by today's NEWS implementation is due to several factors:

- usually, the distance between a seismic event and the closest array recording it is in the order of several hundreds of kilometers;
- it takes several additional minutes until other arrays of the sparse network of arrays in Northern Europe can record the event;
- to achieve a more stable solution for the event location the NEWS algorithm is implemented in such a way that it also waits for possible S-type onsets;
- the location algorithm HYPOSAT (see PD 11.1) used for locating the event may be better optimized for shorter computation time.

9.14.3 Usage of seismic arrays to monitor an EEWS relevant site

With its unique capability to measure not only onset times and amplitudes, but also BAZs and apparent velocities of seismic onsets, an array gives us several possibilities to locate an event. The only question is, which algorithm and data processing scheme should be used to provide quick locations for an EEWS. Working with the above mentioned methods and software packages, one can conclude that with today's computer capacities the most critical parameter for using seismic arrays in an EEWS is the epicentral distance to the array installation(s). All discussed algorithms are on today's computers so fast that the actual calculation times for the different algorithms do not really contribute to EEWS delays. More important are the actual

transmission times of seismic signals since all data connection algorithms work with data frames containing a specific amount of data. The delay time between the actual recording of a signal and its arrival at a data center can vary between seconds and minutes and has to be added to the EEWS times achievable by the discussed location algorithms.

9.14.3.1 The single array case

In the case of single array locations at local or near regional distances, the travel-time difference between source and arrival time of the first P phase is in the order of tens of seconds for local or near regional events. Additional tens of seconds will be needed to record the first S onset, necessary for calculating the epicentral distance. Therefore, such an array used as an EEWS tool will most likely need more time to locate the event than a traditional seismic network installed in the area of interest. The situation changes in many cases where several seismic active areas or a longer tectonic fault contribute to seismic hazard. Dense, local networks cannot be installed at all places and in particular if more remote or off-shore located zones contribute to a hazard scenario, single array installations can contribute, within a few minutes, with quite reliable event locations for all events within some hundred kilometers epicentral distance. Moreover, as shown by Gibbons et al. (2005), a single array can be tuned for a specific target area and the resulting location precision can become as high as that of a local network, assuming that sufficient calibration information is available. This is of particular interest in case of monitoring the aftershock sequence of a very large earthquake.

In the case of source regions with a higher risk to generate tsunamis, it is of large interest to know quickly not only the hypocenter of the earthquake but also at least a rough estimate of the magnitude and details of the rupture lengths. In such cases, algorithms as proposed and tested by Roessler et al. (2010) could be implemented (see also Section 9.8.6) in a tsunami warning system.

9.14.3.2 A single array and a sparse regional network

In the case that data from an array and additionally a regional or local network are available, a FEIS-type algorithm can be used. Knowing the BAZ and apparent velocity of the first P-type onset directly gives information about the direction in which the event occurred and if it was at a local or a regional distance. For regional events, the first P onset should have an apparent velocity typical for Pn phases and for local events typical for Pg onsets, respectively. With this information, the array result for the first P onset directly indicates, which single station records should be added to achieve a fast and more reliable event location.

An EEWS based on a single array and a sparse network can provide a first, quick and reasonably good event location at local or near regional distance ($D < 400$ km) within the first minutes after the event origin time (OT) as long as one of the network stations is located as close as the array or closer to the event.

9.14.3.3 Multiple array configuration

In the case of observations from two or more arrays, a GBF- (see Section 9.13.5) or NEWS-type algorithm can be implemented. Recording one onset from each array with a BAZ

estimate is already sufficient to locate the source area. If the target fault zone is located between two arrays, which have a distance of about 200 km from each other, such an installation is sufficient to locate the main shock and the whole aftershock sequence on the fault zone within about 30 seconds after OT. Events, which are not located between the two arrays, will be located within 20 s plus the absolute travel time of the first P onset to one of the arrays.

This scenario of course assumes that the data of the two arrays are available in real time for fully automated array processing software. The location capabilities and precision will in general increase with a larger number of arrays. In such cases, different arrays may be also combined to monitor simultaneously different target areas.

Acknowledgments

The authors thank John B. Young (Blacknest) for reprints of publications from the old days of array seismology in Great Britain, and Peter Bormann, Brian Kennett, Frank Scherbaum, and Lyla Taylor for critical reviews of the manuscript of this chapter in the first NMSOP edition of 2002. We thank Hanneke Paulssen, John Coyne and Peter Bormann for critically reviewing the new 2011 version of this chapter and for many helpful comments on how to improve it. Main parts of Section 9.14 were compiled during NORSAR's participation in the SAFER project, funded under the Sixth Framework Programme of the European Commission (Project Number 036935).

References

Abrahamson, N. A., Bolt, B. A., Darragh, R. B., Penzien J., and Tsai Y. B. (1987). The SMART 1 accelerograph array (1980-1987): a review. *Earthquake Spectra*, **3**, 263-287.

Abt, A. (1907). *Vergleichung seismischer Registrierungen von Göttingen und Essen (Ruhr)*. Inaugural-Dissertation (Ph.D. thesis), Philosophische Fakultät, Georg-August-Universität zu Göttingen, Göttingen 1907, 26 pp. + curriculum vitae.

Aki, K. (1957). Space and time spectra of stationary stochastic waves with special reference to microtremors. *Bull. Earthqu. Res. Inst.*, **35**, 415-456.

Aki, K., and Richards, P. G. (1980). *Quantitative seismology – theory and methods*, Volume II, Freeman and Company, ISBN 0-7167-1059-5(v. 2), 609-625.

Aki, K., Christoffersson, A., and Husebye, E. S. (1977). Determination of the three dimensional seismic structure of the lithosphere. *J. Geophys. Res.*, **82**, 277-296.

Almendros, J., Ibáñez, J. M., Alguacil, G., and Del Pezzo, E. (1999). Array analysis using circular-wave-front geometry: an application to locate the nearby seismo-volcanic source. *Geophys. J. Int.*, **136**, 159-170.

Almendros, J., Ibàñez, J. M., Alguacil, G., Del Pezzo, E., and Ortiz, R. (1997). Array tracking of the volcanic tremor source at Deception Island, Antarctica. *Geophys. Res. Let.*, **24**, 3069-3072.

Arai, H., and K. Tokimatsu (2004). S-wave velocity profiling by inversion of microtremor H/V spectrum. *Bull. Seism. Soc. Am.*, **94**, 53-63.

Asten, M. W., and Henstridge, J. D. (1984). Array estimators and the use of microseisms for reconnaissance of sedimentary basins. *Geophys.*, **49**, (11), 1828-1837.

Barber, N. S. (1958). Optimum arrays for direction finding. *New Zealand. J. of Sci.*, **1**, 35-51.

Barber, N. S. (1959). Design of 'optimum' arrays for direction finding. *Electronic and Radio Engineer*, **36**, 333-232.

Bard, P.-Y. (1999). Microtremor measurements: a tool for site effect estimation? In: Kudo, K., Okada H., and Sasatani T. (eds.). Proc. of the 2nd Int. Symp. on Effects of Surface Geology on Seismic Motion, Yokohama, Japan, *Balkema*, **3**, 1251-1279.

Beauchamp, K. G. (ed.) (1975). *Exploitation of seismograph networks*, NATO Advanced Study Institutes Series E 111, Nordhoff Leiden, XII + 647 pp.

Benndorf, H. (1905). Über die Art der Fortpflanzung der Erdbebenwellen im Erdinneren. 1. Mitteilung. *Sitzungsberichte der Kaiserlichen Akademie in Wien. Mathematisch-Naturwissenschaftliche Klasse*, **114**, *Mitteilungen der Erdbebenkommission*, **Neue Folge 29**, 1-42.

Benndorf, H. (1906). Über die Art der Fortpflanzung der Erdbebenwellen im Erdinneren. 2. Mitteilung. *Sitzungsberichte der Kaiserlichen Akademie in Wien. Mathematisch-Naturwissenschaftliche Klasse*, **115**, *Mitteilungen der Erdbebenkommission*, **Neue Folge 31**, 1-24.

Benz, H. M., Vidale, J. E., and Mori, J. (1994). Using regional seismic networks to study the Earth's deep interior. *EOS Trans. Am. Geophys. Soc.*, **75**, 225, 229.

Berteussen, K. A. (1974). NORSAR location calibrations and time delay corrections. *NORSAR Sci. Rep.*, **2-73/74**, 41 pp.

Berteussen, K. A. (1976). The origin of slowness and azimuth anomalies at large arrays. *Bull. Seism. Soc., Am.*, **66**, 719-741.

Bettig, B., Bard, P.-Y., Scherbaum, F., Riepl, J., and Cotton, F. (2001). Analysis of dense array noise measurements using the modified spatial autocorrelation method (SPAC). Application to the Grenoble area. *Boll. Geof. Teor. Appl.*, **42**, (3/4), 281-304.

Birtill, J. W., and Whiteway, F. E. (1965). The application of phased arrays to the analysis of seismic body waves. *Phil. Trans. Royal Soc. of London, Math. and Phys. Sciences*, **A-258**, (1091), 421-493.

Bondár, I., North R. G., and Beall, G. (1999). Teleseismic slowness-azimuth station corrections for the International Monitoring System seismic network. *Bull. Seism. Soc. Am.*, **89**, 989-1003.

Bonnefoy-Claudet, S., Cornou, C., Bard, P.-Y., and Cotton, F. (2004). Nature of noise wavefield. *SESAME Deliverable D13.08*, available at http://sesame-fp5.obs.ujf-grenoble.fr/Delivrables/D13.08_finalreport_new.pdf.

Bonnefoy-Claudet, S., Cornou, C., Di Giuglio, G., Guillier, B., Jongmans, D., Köhler, A., Ohrnberger, M., Savvaidis, A., Roten, D., Scherbaum, F., Schissele, E., Vollmer D., and Wathelet, M. (2005). Report on the FK/SPAC capabilities and limitations. *SESAME Deliverable D19.06*, available at http://sesame-fp5.obs.ujf-grenoble.fr/Delivrables/Del-D19-Wp06.pdf.

Braun, T., and Schweitzer, J. (2008). Spatial noise-field characteristics of a three-component small aperture test array in Central Italy. *Bull. Seism. Soc. Amer.*, **98**, 1876-1886, doi: 10.1785/0120070077.

Braun, T., Schweitzer, J., Azzara, R. M., Piccinini, D., Cocco, M., and Boschi E. (2004). Results from the temporary installation of a small aperture seismic array in the Central Apennines and its merits for the local event detection and location capabilities. *Annals of Geophysics* (*Annali di Geofisica*), **47**, 1557-1568.

Bullen, K. E., and Bolt, B. A. (1985). *An introduction to the theory of seismology*. Cambridge University Press, 4th revised ed., xvii+499 pp., ISBN: 0-521-28389-2, 451-454.

Bulletin of the Seismological Society of America (1990). Special Issue: "Regional seismic arrays and nuclear test ban verification". *Bull. Seism. Soc. Am.*, **80**, (6B), 1775-2281.

Bungum, H., Husebye, E. S., and Ringdal F. (1971). The NORSAR array and preliminary results of data analysis. *Geophys. J. R. astr. Soc.*, **25**, 115-126.

Bungum, H., Olesen, O., Pascal, C., Gibbons, S., Lindholm, C., and Vestøl, O. (2010). To what extent is the present seismicity of Norway driven by postglacial rebound? *J. Geolog. Soc. London*, **167**, 373-384, doi: 10.1144/0016-76492009-009.

Burg, J. P. (1964). Three-dimensional filtering with an array of seismometers. *Geophysics*, **29**, 693-713.

Burg, J. P. (1967). Maximum entropy spectral analysis. *37th Ann. Int. SEG Meeting, Soc. Explor. Geophys.*, Oklahoma City, Oklahoma, Oct. 31, 1967.

Buttkus, B. (2000). *Spectral analysis and filter theory in applied geophysics.* Springer Verlag, xv+667 pp., ISBN 3-540-62674-3.

Buttkus, B. (ed.) (1986). Ten years of the Gräfenberg array: defining the frontiers of broadband seismology. *Geologisches Jahrbuch* E-35, Hannover, 135 pp.

Cansi, Y. (1995). An automatic seismic event processing for detection and location: P.M.C.C. method. *Geophys. Res. Lett.*, **22**, 1021-1024.

Cansi, Y., Plantet, J. L., and Massion, B. (1993). Earthquake location applied to a min-array: k-spectrum versus correlation method. *Geophys. Res. Lett.*, **20**, 1819-1822.

Capon, J. (1969a). High-resolution frequency-wavenumber spectrum analysis. *Proc. IEEE*, **57**, 1408-1418.

Capon, J. (1969b). Investigation of long-period noise at the large aperture seismic array. *J. Geophys. Res.*, **12**, 3182-3194.

Capon, J. (1973). Signal Processing and frequency-wavenumber spectrum analysis for a large aperture seismic array. In: Bolt, B. A. (ed.) *Methods in computational physics, **13** Geophysics*. Academic Press, xiii+473 pp., IBN 0-12-460813-2, 1-59.

Capon, J., Greenfield, R. J., and Kolker, K. J. (1967). Multidimensional maximum-likelihood processing of a Large Aperture Seismic Array. *Proc. IEEE*, **55**, 2, 192-211.

Cessaro, R. K (1994). Sources of primary and secondary microseisms. *Bull. Seism. Soc. Am.*, **84**, 142–148.

Chiu, H. C., Yeh, Y. T., Ni, S. D., Lee, L., Liu, W. S., Wen, C. F., and Liu, C. C. (1994). A new strong-motion array in Taiwan: Smart-2. *TAO*, **5**, 463-475.

Chouet, B. (1996). New methods and future trends in seismological volcano monitoring. In: Scarpa, R., and Tilling, R. (eds.). *Monitoring and mitigation of volcano hazards*, Berlin, Springer-Verlag, 1996, xx + 841 pp., ISBN 3-540-60713-7, 23-97.

Christoffersson, A., and Husebye, E. S. (2011). Seismic tomographic mapping of the Earth's interior – back to basics revisiting the ACH inversion. *Earth-Science Rev.*, **106**, 293-306, doi: 101.1016/j.earscirev.2011.02.007.

Cornou, C., Ohrnberger, M., Boore, D. M., Kudo, K., and Bard, P.-Y. (2006). Derivation of structural models from ambient vibration array recordings: results from an international blind test. *3rd Int. Symp. on the Effects of Surf. Geol. on Seismic Motion*, Grenoble, France, 30 August – 1 September 2006.

Dahlman, O., Mykkeltveit, S., and Haak, H. (2009). *Nuclear test ban – converting political visions to reality.* Springer Verlag, xviii+277 pp., ISBN 978-1-4020-6883-6, doi: 10.1007/978-1-4020-6885-0.

Davies, D., Kelly, E. J., and Filson, J. R. (1971). The VESPA process for the analysis of seismic signals. *Nature*, **232**, 8-13.

Del Pezzo, E., and Giudicepietro, F. (2002). Plane wave fitting method for a plane, small aperture, short period seismic array: a MATHCAD program. *Computers and Geosciences*, **28**, 59-64, doi: 10.1016/S0098-3004(01)00076-0.

Delgado, L., López, C. C., Giner, J., Estévez, A., Cuenca, A., and Mouna, S. (2000). Microtremors as geophysical exploration tool: applications and limitations. *Pure Appl. Geophys.*, **157**, 1445-1462.

Dietrich, K., Schweitzer, J., and Meier, T. (2001). S-velocities in the crust and uppermost mantle of northern Fennoscandia deduced from dispersion analysis of Rayleigh waves. *NORSAR Sci. Rep.*, **1–2001**, 71–76.

Doornbos, D. J., and Husebye, E. S. (1972). Array analysis of PKP phases and their precursors. *Phys. Earth Planet. Inter.*, **6**, 387-399.

Douglas, A. (2002). Seismometer arrays – their use in earthquake and test ban seismology. In: Lee, W. H. K., Kanamori, H., Jennings, P. C., and Kisslinger, C. (eds.) (2002): *Handbook of Earthquake and Engineering Seismology*. Academic Press.

Essen, H. H., Krüger, F., Dahm, T., and Grevemeyer, I. (2003). On the generation of secondary microseism observed in north and central Europe. *J. Geophys. Res.*, **108**, B10, ESE 15, 15 pp., doi: 10.1029/2002JB002318.

Fäh, D., Kind, F., and Giardini, D. (2003). Inversion of local S-wave velocity structures from average H/V ratios, and their use for the estimation of site effects. *J. Seism.*, **7**, 449-467.

Foti, S., Parolai, S., Albarello, D., and Picozzi, M. (2011). Application of surface–wave methods for seismic site characterization. *Surv. Geophys.*, doi: 10.1007/s10712-011-9134-2.

Frankel, A., Hough, S., Friberg, P., and Rusby, R. (1991). Observations of Loma Prieta aftershocks from a dense array in Sunnyvale, California. *Bull. Seism. Soc. Amer.*, **81**, 1900-1922.

Freiberger, W. F. (1963). An approximation method in signal detection. *Quart. J. App. Math.*, **20**, 373-378.

Friedrich, A., Krüger, F., and Klinge, K., (1998). Ocean generated microseismic noise located with the Gräfenberg array. *J. Seism.*, **2**, 47-64.

Frosch, R. A., and Green, P. E., Jr. (1966). The concept of a large aperture seismic array. *Proc. Royal Soc.*, **A-290**, 368-384.

Fujiwara, H. (1997). Windowed f-k spectra of a three-dimensional wavefield excited by a point source in a two-dimensional multilayered elastic medium. *Geophys. J. Int.*, **128**, 571-584.

Furumoto, M., Kunitomo, T., Inoue, H., Yamada, I., Yamaoka, K., Ikami, A., and Fukao, Y. (1990). Twin Sources of High-Frequency Volcanic Tremor of Izu-Oshima Volcano. Japan. *Geophys. Res. Lett.*, **17**, 25-27.

Fyen, J. (1989). Event processor program package. *NORSAR Sci. Rep.*, **2-88/89**, 117-123.

Fyen, J. (2001a). *NORSAR seismic data processing – user guide and command reference.* NORSAR (contribution 748), Kjeller, Norway.

Fyen, J. (2001b). *NORSAR seismic detection processing – user guide and command reference*. NORSAR (contribution 731), Kjeller, Norway.

Geller, R. J., and Mueller, C. S. (1980). Four similar earthquakes in central California. *Geophys. Res. Lett.*, **7**, 821-824.

Gibbons, S. J., and Ringdal, F. (2006). The detection of low magnitude seismic events using array-based waveform correlation. *Geophys. J. Int.*, **165**, 149-166.

Gibbons, S. J., Kværna, T., and Ringdal, F. (2005). Monitoring of seismic events from a specific source region using a single regional array: A case study. *J. Seism.* **9**, 277-294.

Gibbons, S. J., Kværna, T., and Ringdal, F. (2009). Considerations in phase estimation and event location using small-aperture regional seismic arrays. *Pure Appl. Geophys.*, doi: 10.1007/s00024-009-0024-1.

Gibbons, S. J., Schweitzer, J., Ringdal, F., Kværna, T., Mykkeltveit, S., and Paulsen, B. (2011). Improvemnets to seismic monitoring of the European Arctic using three-component array processing at SPITS. *Bull. Seism. Soc. Am.*, **101**, 2737-2754, doi: 10.1785/0120110109.

Goldstein, P., and Archuleta, R. J. (1991a). Deterministic frequency-wavenumber methods and direct measurements of rupture propagation during earthquakes using a dense array: theory and methods. *J. Geophys. Res.*, **96**, 6173-6185.

Goldstein, P., and Archuleta, R. J. (1991b). Deterministic frequency-wavenumber methods and direct measurements of rupture propagation during earthquakes using a dense array: data analysis. *J. Geophys. Res.*, **96**, 6187-6198.

Goldstein, P., and Chouet, B. (1994). Array measurements and modeling of sources of shallow volcanic tremor at Kilauea Volcano, Hawaii. *J. Geophys. Res.*, **99**, 2637-2652.

Halldorsson, B., Sigbjornsson, S., and Schweitzer, J. (2009). ICEARRAY: the first small-aperture, strong-motion array on Iceland. *J. Seism.*, **13**, 173-178, doi: 10.1007/s10950-008-9133-z.

Hao, C., and Zheng, Z. (2009). Slowness-azimuth corrections of teleseismic events for IMS primary arrays in China. *J. Seism.*, **13**, 437-448, doi: 10.1007/s10950-008-9137-8.

Harjes, H.-P. (1990). Design and siting of a new regional seismic array in Central Europe. *Bull. Seism. Soc. Am.*, **80**, 1801-1817.

Harjes, H.-P., and Henger, M. (1973). Array-Seismologie, *Zeitschrift für Geophysik*, **39**, 865-905.

Harjes, H.-P., and Seidl, D. (1978). Digital recording and analysis of broad-band seismic data at the Gräfenberg (GRF-) array. *J. Geophys.*, **44**, 511-523.

Harjes, H.-P., Schulte-Theis, H., Jost, M. L., and Schweitzer, J. (1996). Fast Earthquake Information Service (FEIS). *CSEM / EMSC, Newsletter*, **9**, 2-4, 1996.

Haubrich, R. A. (1968). Array design. *Bull. Seism. Soc. Am.*, **58**, 977-991.

Herrmann, R.-B. (1987). *Computer programs in seismology, Volume 4*, St Louis University.

Horike, M. (1985). Inversion of phase velocity of long-period microtremors to the S-wave velocity structure down to the basement in urbanized areas. *J. Phys. Earth*, **33**, 59-96.

Huang, B.-S. (2001). Evidence for azimuthal and temporal variation of the rupture propagation of the 1999 CH-Chi, Taiwan earthquake from dense seismic array observations. *Geophys. Res. Lett.*, **28**, 3377-3380.

IBM (1972). *Seismic array design handbook.* ARPA Order No. 800, USAF Electronic System Division Contract No. F19628-68-C-0400, Gaithersburg, Maryland, August 1972, xv + 483 pp.

Ibs von Seht, M., and Wohlenberger, R. (1999). Microtremor measurements used to map thickness of soft soil sediments. *Bull. Seism. Soc. Am.*, **89**, 250-259.

Ishii, M., Shearer, P., and Vidale, J. (2005a). Extent, duration and speed of the 2004 Sumatra-Andaman earthquake imaged by the Hi-Net array. *Nature*, **435**, 933-936, doi: 10.1038/nature03675.

Ishii, M., Shearer, P. M., Houston, H., and Vidale, J. E. (2005b). Teleseismic P wave imaging of the 26 December 2004 Sumatra-Andaman and 28 March 2005 Sumatra earthquake ruptures using the Hi-Net array. *J. Geophys. Res.*, **112**, B11307, doi: 10.1029/2006JB004700.

Iyer, H. M. (1968). Determination of frequency-wave-number spectra using seismic arrays. *Geophys. J. R. astr. Soc.*, **16**, 97-117.

J-Array Group (1993). The J-array program: system and present status. *J. Geomag. Geoelectr.*, **45**, 1265-1274.

Johnson, D. H., and Dudgeon, D. E. (1993, 2002). *Array signal processing: concepts and techniques*. Prentice Hall signal processing series, PTR Prentice Hall, XIII+533 pp., ISBN 0-13-048513-6.

Jongmans, D., Ohrnberger, M., and Wathelet, M. (2005). Recommendations for array measurements and processing. *Deliverable D24.13*, available at http://sesame-fp5.obs.ujf-grenoble.fr/Delivrables/Del-D24-Wp13.pdf.

Journal of Seismology (2011). Special Issue: "Array seismology in Europe: recent developments and applications", *J. Seism.*, **15**, (3), 429-556.

Kanasewich, E. R., Hemmings, C. D., and Alpaslan, T. (1973). N-th root stack nonlinear multichannel filter. *Geophysics*, **38**, 327-338.

Keen, C. G., Montgomery, J., Mowat, W. M. H., and Platt, D. C. (1965). British seismometer array recording systems. *The Radio and Electronic Engineer*, **30**, 297-306.

Kelly, E. J. Jr., and Levin, M. J. (1964). Signal parameter estimation for seismometer arrays. *M.I.T., Lincoln Laboratory Techn. Rep.*, **339**, Lexington, Massachusetts.

Kennett, B. L. N. (2000). Stacking three-component seismograms. *Geophys. J. Int.*, **141**, 263-269.

Kennett, B. L. N. (2002). *The seismic wavefield, Volume II: Interpretation of seismograms on regional and global scale.* Cambridge University Press, xii+534 pp., ISBN 0-521-00665-1, 163-170.

Kind, F. (2002). *Development of microzonation methods: application to Basle, Switzerland.* Dissertation ETH No. 14548, Swiss Federal Institute of Technology, Zürich, 110 p.

Krüger, F., and Ohrnberger, M. (2005a). Tracking the rupture of the $M_W = 9.3$ Sumatra earthquake over 1150 km at teleseismic distance. *Nature*, **435**, 937-939, doi: 10.1038/nature0369kao.

Krüger, F., and Ohrnberger, M. (2005b). Spatiuo-temporal source characteristics of the 26 December 2004 Sumatra earthquake as imaged by teleseismic broadband arrays. *Geophys. Res. Lett.*, **32**, L24312, doi: 10.1029/2005GL023939.

Krüger, F., and Weber, M. (1992). The effect of low velocity sediments on the mislocation vectors of the GRF array. *Geophys. J. Int.*, **105**, 387-393.

Krüger, F., Weber, M., Scherbaum, F., and Schlittenhardt, J. (1993). Double beam analysis of anomalies in the core-mantle boundary region. *Geophys. Res. Lett.*, **20**, 1475-1478.

Kuleli, S., Zor, E., Türkelli, N, Sandvol, E., Seber, D., and Barazangi, M. (2001). The IMS Belbaşi seismic array (BRAR) in Central Turkey. *Seism. Res. Lett.*, **72**, 60-69.

Kværna, T. (1989). On exploitation of small-aperture NORESS type arrays for enhanced P-wave detectability. *Bull. Seism. Soc. Am.*, **79**, 888-900.

Kværna, T., and Doornbos, D. J. (1986). An integrated approach to slowness analysis with arrays and three-component stations. *NORSAR Sci. Rep.*, **2-85/86**, 60-69.

Kværna, T., and Ringdal, F. (1986). Stability of various f-k estimation techniques. *NORSAR Sci. Rep.*, **1-86/87**, 29-40.

Kværna, T., Schweitzer, J., Taylor, L., and Ringdal, F. (1999). Monitoring of the European Arctic using regional generalized beamforming. *NORSAR Sci. Rep.*, **2–98/99**, 78–94.

Lacoss, R. T. (1965). Geometry and patterns of Large Aperture Seismic Arrays. *M.I.T., Lincoln Laboratory, Techn. Note*, **1965-64**, Lexington, Massachusetts.

Lacoss, R. T., Kelly, E. J., Toksöz, and M. N. (1969). Estimation of seismic noise structure using arrays. *Geophysics*, **34**, 21-38.

Levander, A., Humphreys, E. D., Ekstrom, G., Meltzer, A. S., and Shearer, P. M. (1999). Continental Assembly, Stability, and Instability: USArray: An Earth sciences tool for investigating North America. *EOS Trans. Am. Geophys. Un.*, **80**, 245-249.

Levin, M. J. (1964). Maximum-likelihood array processing. *Lincoln Laboratory Report*, **31**, December 1964.

Liaw, A. L., and McEvilly, T. V. (1979). Microseisms in geothermal exploration – studies in Grass Valley, Nevada. *Geophysics*, **44**, 1097-1115.

Linville, F. A., and Laster, S. J. (1966). Numerical experiments in the estimation of frequency-wavenumber spectra of seismic events using linear arrays. *Bull. Seism. Soc. Am.*, **56**, 1337-1355.

Malischewsky, P., and Scherbaum, F. (2004) Love's formula and H/V ratio (ellipticity) of Rayleigh waves. *Wave Motion*, **40**, (1), 57-67.

Manchee, E. B. and Weichert, D. H. (1968). Epicentral uncertainties and detection probabilities from the Yellowknife seismic array data. *Bull. Seism. Soc. Am.*, **58**, 1359-1377.

Muirhead, K. J. (1968). Eliminating false alarms when detecting seismic events automatically. *Nature*, **217**, 553-554.

Muirhead, K. J., and Ram Datt (1976). The N-th root process applied to seismic array data. *Geophys. J. R. Astr. Soc.*, **47**, 197-210.

Mykkeltveit, S. (1985). A new regional array in Norway: design work and results from analysis of data from a provisionally installation. In: A.U. Kerr (editor). *The VELA Program – A twenty-five year review of basic research.* Defence Advanced Research Project Agency, xviii + 964 pp., 1985, 546-553.

Mykkeltveit, S., and Bungum, H. (1984). Processing of regional seismic events using data from small-aperture arrays. *Bull. Seism. Soc. Am.*, **74**, 2313-2333.

Mykkeltveit, S., Åstebøl, K., Doornbos, D. J., and Husebye, E. S. (1983). Seismic array configuration optimization. *Bull. Seism. Soc. Am.*, **73**, 173-186.

Mykkeltveit, S., Fyen, J., Ringdal, F., and Kværna, T. (1988). Spatial characteristics of the NORESS noise field and implications for array detection processing. *Phys. Earth Planet. Inter.*, **63**, 277-283.

Nakamura, Y. (1989). A method for dynamic characteristics estimation of subsurface using microtremor on the ground surface. *Quat. Rep. RTRI*, **30**, 25-33.

Nogoshi, M., and Igarashi, T. (1971). On the amplitude characteristics of microtremor (part 2). *J. Seism. Soc. Japan*, **24**, 26-40 (Japanese with English abstract).

Ødegaard, E., Doornbos, D. J., and Kværna, T. (1990). Surface topographic effects at arrays and three-component stations. *Bull. Seism. Soc. Am.*, **80,** 2214-2226.

Ohori, M., Nobata, A., and Wakamatsu, K. (2002). A comparison of ESAC and FK methods of estimating phase velocity using arbitrarily shaped microtremor arrays. *Bull. Seism. Soc. Am.*, **92**, (6), 2323-2332.

Okada, H. (2003). The microseismic survey method. *Soc. Expl. Geophys. Japan, Geophys. Mon. Ser.*, **12** (translated by Koya Suto).

Parolai, S., Bormann, P., and Milkereit, C. (2001). Asssessment of the natural frequency of the sedimentary cover in the Cologne area (Germany) using noise measurements. *J. Earthq. Eng.*, **5**, 541-564.

Parolai, S., Bormann, P., and Milkereit, C. (2002). New relationship between Vs, thickness of the sediments, and resonance frequency calculated by the H/V ratio of seismic noise for the Cologne area (Germany). *Bull. Seism. Soc. Amer.*, **92**, 2521-2527.

Parolai, S., Picozzi, M., Richwalski, S. M., and Milkereit, C. (2005). Joint inversion of phase velocity dispersion and H/V ratio curves from seismic noise recordings using a genetic algorithm, considering higher modes. *Geophys. Res. Lett.*, **32**, doi: 10.1029/2004GL021115.

Picozzi, M., Parolai, S., and Richwalski, S. M. (2005). Joint inversion of H/V ratios and dispersion curves from seismic noise: Estimating the S-wave velocity of bedrock. *Geophys. Res. Lett.*, **32,** doi: 10.1029/2005GL022878.

Ringdal, F., and Kværna, T. (1989). A multi-channel processing approach to real time network detection, phase association, and threshold monitoring. *Bull. Seism. Soc. Am.*, **79**, 1927-1940.

Roessler, D., Krueger, F., Ohrnberger, M., and Ehlert, L. (2010). Rapid characteristics of large earthquakes by m,ultiple seismic broadband arrays. *Nat. Hazards Earth. Syst. Sci.*, **10**, 923-932, www.nat-hazards-earth-syst-sci.net/10/923/2010/.

Rost, S., and Thomas, C. (2002). Array Seismology: Methods and applications. *Rev. Geophys.*, **40**, (3), 1008, doi: 10.1029/2000RG000100.

Rost, S., and Thomas, C. (2009). Improving seismic resolution through seismic arrays. *Surv. Geophys.*, **30**, 271-299, doi: 10.1007/s10712-009-9070-6.

Sambridge, M. (1999a). Geophysical inversion with a neighbourhood algorithm – I. Searching a parameter space. *Geophys. J. Int.*, **138**, 479-494.

Sambridge, M. (1999b). Geophysical inversion with a neighbourhood algorithm – II. Appraising the ensemble. *Geophys. J. Int.*, **138**, 727-746.

Scherbaum, F. (2001). *Of Poles and Zeros: Fundamentals of Digital Seismology*. Kluwer Academic Publishers, 2nd edition, 265 pp. (including a CD-ROM by E. Schmidtke and F. Scherbaum, with examples written in Java).

Scherbaum, F., Hinzen, K. G., and Ohrnberger, M. (2003). Determination of shallow shear wave velocity profiles in the Cologne, Germany area using ambient vibrations. *Geophys. J. Int.*, **152**, 597-612.

Schimmel, M., and Paulssen, H. (1997). Noise reduction and detection of weak, coherent signals through phase-weighted stacks. *Geophys. J. Int.*, **130**, 497-505.

Schmidt, R. O. (1986). Multiple emitter location and signal parameter estimation. *IEEE Trans. Ant. Prop.*, **AP-34**, 276-280.

Schmidt, R. O., and Franks, E. R. (1986). Multiple source df signal processing: an experimental system. *IEEE Trans. Ant. Prop.*, **AP-34**, 281-290.

Schulte-Pelkum, V., Earle, P. S., and Vernon, F. L. (2003). Strong directivity of ocean-generated seismic noise. *Geochem. Geophys. Geosyst.*, **5**, Q03004, doi: 10.1029/2003GC000520.

Schulte-Theis, H., Jost, M. L., and Schweitzer, J. (1995). Fast earthquake information service (FEIS): optimized location of seismic events in Europe. In: *Advanced waveform research methods for GERESS recordings*. Scientific Report 4, 1 December 1994 – 30 June 1995, DARPA Grant MDA 972–93–1–0022, 17–28, 1995

Schweitzer, J. (1994). Some improvements of the detector / SigPro-system at NORSAR. *NORSAR Sci. Rep.*, **2–93/94**, 128–139.

Schweitzer, J. (1998). Tuning the automatic data processing for the Spitsbergen array (SPITS). *NORSAR Sci. Rep.*, **1-98/99**, 110-125.

Schweitzer, J. (2001). Slowness corrections – one way to improve IDC products. *Pure Appl. Geophys.*, **158**, 375-396.

Schweitzer, J. (2003). NORSAR's event warning system (NEWS). *NORSAR Sci. Rep.*, **1–2003**, 27-31.

Schweitzer, J., and Krüger, F. (2011). Foreword (special issue “Array seismology in Europe: recent developments and applications”). *J. Seismology*, **15**, (3), 429-430, doi: 10.1007/s10950-011-9241-z.

Schweitzer, J., and Kværna, T. (2002). Design study for the refurbishment of the SPITS array (AS72). *NORSAR Sci. Rep.*, **2–2002**, 65–77.

Semin, K. U., Ozel, N. M., and Necmioglu, O. (2011). Detection and identification of low-magnitude seismic events near Bala, Central Turkey, using array-based waveform correlation. *Seism. Res. Lett.*, **82**, (1), 97-103.

SESAME group (2004). Guidelines for the implementation of the H/V spectral ratio technique on ambient vibrations measurements, processing and interpretation. *SESAME Deliverable D23.12*, available at http://sesame-fp5.obs.ujf-grenoble.fr/Delivrables/Del-D23-HV-User-Guidelines.pdf.

Shen, X., and Ritter, J. R. R. (2010). Small-scale heterogeneities below the Lanzhou CTBTO seismic array, from seismic wave field fluctuations. *J. Seism.*, **14**, 481-493.

Somers, H., and Manchee, E. B. (1966). Selectivity of the Yellowknife seismic array. *Geophys. J. R. astr. Soc.*, 10, 401-412.

Spudich, P., and Bostwick, T. (1987). Studies of the seismic coda using an earthquake cluster as deeply buried seismograph array. *J. Geophys. Res.*, **92**, 10526-10546.

Spudich, P., and Cranswick, E. (1984). Direct observation of rupture propagation during the 1979 Iperial Valley earthquake using a short baseline accelerometer array. *Bull. Seism. Soc. Am.*, **74**, 2083-2114.

Tibuleac, I. M., and Stroujkova, A. (2009). Calibrating the Chiang Mai seismic array (CMAR) for improved event location. *Seism. Res. Lett.*, **80**, 579-590, doi: 10.1785/gssrl.80.4.579.

Tokimatsu, K. (1997). Geotechnical site characterization using surface waves. In: Ishihara, K. (ed.): Proc. IS-Tokyo '95, 1st Intl. conf. Earthquake Geotech. Eng., Tokyo, Japan, 14-16 November 1995, *Balkema*, **3**, 1333-1368.

Tokimatsu, K., Tamura, S., and Kojima, H. (1992). Effects of multiple modes on Rayleigh wave dispersion. *J. Geotech. Eng. ASCE*, **118**, (10), 1529-1543.

van der Kulk, W., Rosen, F., and Lorenz, S. (1965). Large aperture array signal processing study. *IBM Final Report*, ARPA Contract SD-296, Rockville.

Wang, J. (2002). A scheme for initial beam deployment for the International Monitoring System arrays. *Pure Appl. Geophys.*, **159**, 1005-1020.

Wathelet, M. (2008). An improved neighbourhood algorithm: parameter conditions and dynamic scaling. *Geophys. Res. Lett.*, **35**, L09301, doi: 10.1029/2008GL033256.

Wathelet, M., Jongmans, D., and Ohrnberger, M. (2004). Surface wave inversion using a direct search algorithm and its application to ambient vibration measurements. *Near Surf. Geophys.*, **2**, 211-221.

Weichert, D. H. (1975). The role of medium aperture arrays: the Yellowknife system. In: Beauchamp, K. G., (1975), 167-195.

Weichert, D. H., Manchee, E. B., and Whitham, K. (1967). Digital experiments at twice real-time speed on the capabilities of the Yellowknife seismic array. *Geophys. J. R. astr. Soc.*, **13**, 277-295.

Whiteway, F. E. (1965). The recording and analysis of seismic body waves using linear cross arrays. *The Radio and Electronic Engineer*, **29**, 33-46.

Whiteway, F. E. (1966). The use of arrays for earthquake seismology. *Proc. Royal Soc.*, **A-290**, 328-342.

Willmore, P. L. (1979). *Manual of seismological observatory practice*. World Data Center A, Report **SE-20**, 165 pp., reprinted 1982.